Universidad Autónoma de Madrid
Departamento de Física Teórica

The MareNostrum Universe: A numerical study of galaxy clusters

Memoria de Tesis Doctoral

Raúl Sevilla González

Dirigida por Gustavo Yepes Alonso

Madrid, Septiembre de 2010

To Gene Roddenberry,
the man whose dream
inspired many others
and triggered this work.

Resumen

Los cúmulos de galaxias ocupan una importante posición en la jerarquía de la estructura cosmológica por diferentes razones. Éstos, que son unos de los objetos más grandes del Universo, contienen cientos de galaxias y gas caliente que emite gran cantidad de rayos X, por lo que pueden ser detectados a grandes distancias.

Estos objetos nos permiten estudiar la estructura a gran escala del Universo y, a partir de sus propiedades físicas, extraer información cosmológica (ver Rosati et al. (2002)). En la última década se ha producido un considerable avance en las observaciones de todas las componentes de los cúmulos. Las nuevas observaciones de alta resolución en rayos X de CHANDRA y XMM-Newton han revolucionado nuestro conocimiento de las propiedades del gas caliente gracias a mapas de densidad del gas, temperatura y metalicidad (e.g. Vikhlinin et al. (2006), Mantz et al. (2009), Pratt et al. (2010)). En la actualidad, las incertidumbres estadísticas debidas a tener muestras pequeñas son las que predominan en los análisis, algo que sólo puede ser resuelto aumentando la muestra de objetos observados.

La próxima generación de observaciones debería cubrir un rango representativo de redshifts $z < 2$, al mismo tiempo que sondear un rango de masas más amplio. Esto permitiría estudiar las propiedades de los sistemas más pequeños a alto redshift según se van fusionando en objetos mayores. Sin embargo, cada vez queda más claro que cualquier estudio cosmológico preciso en las próximas décadas necesitará de una precisión en las estimaciones de masa de los cúmulos de $\sim 5 - 10\%$.

Es un hecho conocido que las masas de los cúmulos están fuertemente correlacionadas con las propiedades que presentan en rayos X (e.g. Fabian et al. (1994), Markevitch (1998), Voit (2005a)) son las llamadas relaciones de escala. Gracias a dichas relaciones es, en principio, posible convertir directamente una cantidad en otra. Teóricamente, las relaciones de escala son básicamente una consecuencia directa del teorema del virial (modelo auto-similar, (Kaiser

1986)), aunque las observaciones han sacado a la luz dos complicaciones. En primer lugar, las pendientes de las relaciones observadas en rayos X son más pronunciadas que las predichas, debido a un exceso de entropía en el núcleo de los cúmulos, como se muestra en Ponman et al. (1999). En segundo lugar, cada relación de escala presenta una dispersión intrínseca debida a la variedad de estados dinámicos de los cúmulos y el efecto del entorno en que se encuentran.

Gracias a los códigos numéricos cosmológicos se ha podido simular con precisión la dinámica de la materia oscura y las componentes bariónicas y poder comprender los procesos físicos involucrados en la formación de cúmulos. En los últimos $7-10$ años, la mayoría del los recursos computacionales se han empleado en modelizar procesos bariónicos radiativos adicionales para explicar el exceso de entropía.

En esta tesis seguimos un enfoque distinto. La computación numérica de la física radiativa requiere un consumo de $\sim 60\%$ del tiempo de ejecución a pesar de ser más importante sólo en la región más interna de los cúmulos. Al no tener en cuenta estos procesos bariónicos adicionales en el código, las simulaciones se pueden hacer sobre volúmenes mayores y con una mayor resolución. El único inconveniente es que los núcleos no están bien muestreados; en cambio se crean muestras mayores de cúmulos, incluso a redshifts altos, que están correctamente simulados hasta en sus zonas más externas.

Siguiendo este espíritu hemos realizado una serie de simulaciones adiabáticas de alta resolución utilizando uno de los mayores sistemas computacionales del mundo, el supercomputador MARENOSTRUM instalado en el Centro Nacional de Supercomputacin de Barcelona (BSC). Estos experimentos numéricos, que se incluyen dentro del MNCP(MARENOSTRUM Numerical Cosmology Project), consisten en cinco simulaciones que recrean la formación de estructura a gran escala en tres de los entornos cosmológicos más plausibles. La simulación MUC es la que presenta una interés especial ya que es la mayor simulación cosmológica hidrodinámica que se ha realizado hasta la fecha. En este trabajo presentamos el análisis y los resultados de los cúmulos de galaxias de dichas simulaciones a partir de las relaciones de escala y sus abundancias.

Primeramente, caracterizamos las relaciones a $z = 0$ en los distintos entornos cosmológicos centrándonos en la dispersión intrínseca. Actualmente hay varias formas de estimar la masa de los cúmulos (Vikhlinin et al. 2009), para elegir el más preciso es necesario determinar las incertidumbres debidas a la dispersión intrínseca. Además, prestamos especial atención al papel de la resolución numérica como fuente de dispersión en las simulaciones para comparar con los resultados de trabajos de otros autores con menor resolución.

En segundo lugar, la densidad de cúmulos de galaxias en el universo es muy sensible a los parámetros cosmológicos que continuamente se actualizan gracias a observaciones del CMB(Spergel et al. (2003), Spergel et al. (2007), Dunkley et al. (2009)). Nosotros calculamos la función de temperatura en rayos X (XTF) en nuestras simulaciones para comprobar si los modelos cosmológicos considerados en esta tesis son capaces de reproducir el número de cúmulos de galaxias observados en la actualidad. Al mismo tiempo, calibramos la normalización de las relaciones $M_{\rm tot} - T_{\rm X}$ necesarias para reconciliar simulaciones y observaciones.

Finalmente, utilizamos el catalogo de cúmulos de galaxias obtenido en la simulación MUC para estudiar la evolución de las relaciones de escala en rayos X en el rango de redshifts $z = 0 - 1$. Dada la gran resolución de esta simulación, pretendemos establecer las bases a partir de la cual posteriores resultados numéricos puedan determinar el efecto neto que tienen los diversos procesos radiativos del gas a distintos redshifts.

Abstract

Galaxy clusters are an important position within the hierarchy of cosmological structures for several reasons. They are the largest objects in the Universe, formed by hundred of galaxies embedded in hot gas that emits a large amount of X-rays, making possible their detection at large distances.

They allow us to study the large-scale structure of the Universe and, through out their physical properties, we can also obtain cosmological information (see Rosati et al. (2002)). Over the past decade, dramatic progress has been made in observations of all the main components of clusters. New high-resolution X-ray observations by CHANDRA and XMM-Newton have revolutionized our knowledge about properties of the hot gas by reliably mapping gas density, temperature and metallicity, e.g. Vikhlinin et al. (2006), Mantz et al. (2009), Pratt et al. (2010). Nowadays, statistical uncertainties arising from small sample sizes remain the dominant uncertainty in current studies, which could be solved by increasing the sample with further observations.

The next generation of observations should cover a representative range of redshifts $z < 2$, probing also a wide range of masses. This would allow to study the properties of smaller systems at high-z as they merge and are incorporated into larger ones. However, it is increasingly clear that any precision cosmological study in the next decades will need cluster mass estimates with a systematic accuracy of $\sim 5 - 10\%$.

Cluster masses are known to be tightly correlated with X-ray observables, (e.g. Fabian et al. (1994), Markevitch (1998), Voit (2005a)), through the so-called scaling relations. Thanks to these relations it is, in principle, straightforward to convert between two quantities. Theoretically, the scaling relations are essentially a direct consequence of the virial theorem (self-similar model, Kaiser (1986)), but observations revealed two complications. Firstly, the slopes of the X-ray observed relations were steeper than the predicted due to an excess of entropy in the core of the clusters, as shown in Ponman et al. (1999). Secondly, each scaling relation presents an intrinsic scatter due to the

different formation histories of clusters of the same mass.

Modern cosmological numerical codes has been developed to accurately follow the dynamics of dark matter and gaseous baryonic components to eventually understand the physical processes involved in cluster formation. During the last $7-10$ years, most of the computational effort have focused on including additional baryonic processes that can account for the entropy excess seen in observations.

In this thesis we follow a different approach. The numerical computation of radiative physics takes $\sim 60\%$ of the computing time although they are most important in the inner region of clusters. By disabling the computation of additional baryonic processes from the code, simulations of larger volumes can be performed at higher resolution. The only drawback is that inner cores are poorly modeled; in exchange a larger sample of clusters, even at high redshift, which are accurately resolved up to very large radii are produced.

In this spirit we have performed a series of adiabatic high resolution simulations using one of the largest computational facilities in the world, the MARENOSTRUM supercomputer at the Barcelona Supercomputing Center (BSC). This numerical experiments, which are part of the MNCP (MARENOSTRUM Numerical Cosmology Project), consist in five simulations that follow the formation of large-scale structure in the three most flavoured cosmological frameworks. Of particular interest is the MUC simulation which is the largest cosmological SPH simulation ever performed. In this work we present the analysis and results of the galaxy clusters in these simulations by means of the scaling relations and their abundances.

Firstly, we characterise the relations at $z = 0$ in the different cosmological environments focusing in the intrinsic scatter. Several ways to estimate cluster masses are currently available (Vikhlinin et al. 2009), choosing the most accurate one is eventually determined by the uncertainty due to the intrinsic scatter. Furthermore, we pay special attention to the role of numerical resolution in the amount of scatter present in simulations for a comparison with other authors' studies that have lower resolution.

Secondly, the density of galaxy clusters in the Universe is very sensitive to the cosmological parameters which are continuously being updated by more accurate observations of the CMB (Spergel et al. (2003), Spergel et al. (2007), Dunkley et al. (2009)). We compute the X-ray Temperature Function (XTF) in our simulations to test whether the observed number of galaxy clusters at the present time can be obtained with in the cosmological models considered in this thesis. At the same time, we derive the normalization in the $M_{\rm tot} - T_{\rm X}$

relations necessary to reconcile simulations and observations.

Finally, we use the catalogue of galaxy clusters identified in MUC simulation to study the evolution of X-ray scaling relations in the redshift range $z = 0-1$. Given its very high resolution, this establishes a foundation from where further numerical results can determine the net effect of radiative gas processes at different redshift.

Agradecimientos

Al finalizar un trabado tan ardúo y tan duro, a la par que enriquecedor, como la realización de una tesis doctoral es inevitable recordar a todas las personas que de una u otra manera han tenido relevancia en mi vida en los últimos años. Espero que se presenten muchos más y que pueda seguir aprendiendo en mayor o menor medida de todo lo que llegue a partir de ahora gracias a ellos. Aprovechar este espacio para expresarles mis agradecimientos.

Es justo empezar con mi director Gustavo Yepes al que le debo de agradecer de una manera muy especial el haberme iniciado y guiado en mis primeros pasos en la investigación. Su apoyo, paciencia e increíble capacidad para resolver todos los problemas que han surgido hacen que que este trabajo sea posible en una gran medida gracias a él. En este sentido no puedo olvidarme de sus colaboradores, destacando a S. Gottlöber y V. Müller, por su disponibilidad y paciencia y en especial, por acogerme en el Instituto de Astrofísica de Potsdam al que considero mi segunda casa.

Tambié es de obligado cumplimiento agradecer a mi familia. Mis padres, David y Rana que son los que siempre han estado aportando cariño y siempre me han apoyado a pesar de la distancia.

Muchas gracias a aquellos que me conocen desde tiempos inmemoriales. Juanjo al que he tenido que decepcionar por no elegir uno de esos buenos temas que sugirió para la tesis, como “Contar el número de planetas del sistema solar” o “Encontrar la cara simpática de la Luna”. Jorge por mostrarme como un carnet de conducir puede ser tan complicado como una tesis. Jaime, por descubrir a la *Garra Garrática*. Rodolfo, que con algodones es capaz de arreglar cualquier ordenador. Bueno, claro, y Dan Wilmort que no puede faltar con ese espíritu navideño que le caracteriza.

También a los amigos super-piratas que son los que más han sufrido todo el proceso. Rubén, empezamos juntos y hemos acabado cada uno en una punta del mundo. Abi, siempre optimista para todo y todos. Jaime, a pesar de

dejarme sólo al frente del *equipo*. Conchi, por mucho que te empeñes no eres lo peor.

Gracias a mis compañeros astromonos de los pasillos de la UAM. Cómo esta familia es muy extensa voy a empezar por mis hermanos científicos mayores que estuvieron desde un principio y de los que más he aprendido. Yago, Enrique y Alcione (tenías razón, las palmeras de chocolate son imprescindibles para escribir), compañeros de nocturnidades en el observatorio. Marta, quien siempre me dice lo que necesito oir cuando más falta me hace. Que Dios te lo pague con más ... Jesús, por esos innumerables cafés que nos hemos tomado. Luis, atravesamos juntos el desierto, literalmente. Mariluz, que durante un tiempo fue el ángel del observatorio. Y a muchos otros que han pasado por aquí: Jose, Federico, Néstor, Jairo, Marcelo, Álex, Guille y Moni, Manuel, Carlos Hoyos, Héctor, Latifa, y Judit.

A todos voleistas revoltosos y amixtosos sueltos por la pista de la universidad, Suances, Sotillo, etc: Sory, Alberto, J4v1, la señora Schettini, Luis, Elena, Kengo, Cris, Cova, Rosa, Bego, César, Sofi, Jose el macarrón, Vane, Jorge, Víctor, Mario, los Rubenes, Gorka, Isa, Carla, Mery. Ufff, empiezo a contar y no acabo, daos por saludados los demás. Y por extensión al personal del pabellón. Y para acabar... Dani... tontorrón, que de tí no me podía olvidar.

Por supuesto que tengo que nombrar a ese equipazo de la UAM, que son muy grandes. Mertxante, Miguel, Kefrén, Jorge, César, Dani, Mauro, Nacho, Deme, Adrián, Hugo y Álex. Por cierto... ¡Búfalo!

También hay un huequecillo para los del EMVA. Todos no cabeis así que sólo nombro una representación. Belén, Bombero, Susanne, Ana Cris, Óscar, Álex, los de 30-casi40ytantos, Jorge, Bonilla, Merche, Papi, la árbitra guapa, Perico, Bea y por extensión al resto.

He dejado para el final a aquellos que merecen una atención por lo mucho que me han aportado: Juan Campos, el hombre que nunca descansa. Y Lola, que lleva aún más tiempo que yo por los pasillos de la UAM.

Contents

Nomenclature

BAO	Baryon Acoustic Oscillations
CIE	Collisional Ionization Equilibrium
CMB	Cosmic Microwave Background
FOF	Friends-of-friends halo identification algorithm
GADGET-2	Second version of GADGET numerical code (Springel 2005)
ICM	Intracluster Medium
LTE	Local Thermodynamic Equilibrium
MEKAL	Mewe-Kaastra-Liedahl plasma code (Mewe et al. 1985, Liedahl et al. 1995)
MGS	Millennium Gas Simulations
MNCP	MARENOSTRUM Cosmology Project
MU2W	MARENOSTRUM Universe, different realization. WMAP3 model
MUC	MARENOSTRUM Universe. WMAP1 cosmology. Higher resolution
MUCL	MARENOSTRUM Universe. WMAP1 cosmology
MUW	MARENOSTRUM Universe. WMAP3 cosmology
MUWHS	MARENOSTRUM Universe. WMAP3 cosmology at $\sigma_8 = 0.8$
MST	Minimum Spanning Tree
SPH	Smoothed Particle Hydrodynamics (Monaghan 1992)
SZ	Sunyaev-Zel'dovich effect (Sunyaev & Zel'dovich 1972)
WHIM	Warm-Hot Intergalactic Medium

WMAP1	1-year WMAP data release
WMAP3	3-year WMAP data release
WMAP5	5-year WMAP data release
XTF	X-ray Temperature Function

List of Figures

List of Tables

Chapter 1

Introduction

> In the beginning God created the heaven and the earth.
> And the earth was without form and void;
> and darkness was upon the face of the deep.
> And the Spirit of God moved upon the face of the waters.
> And God said, let there be light and there was light.
> And God saw the light, that it was good...
>
> *In the beginning*, Mike Oldfield

For centuries, mankind has been wondering what is our place in the vast world surrounding us. Tied in with this was the fundamental question of how the world came into being. After centuries of mixture of myth and religion by various civilizations, it was with the ancient Greeks when astronomy and cosmology entered the level of scientific inquiry. While the common Greek citizens still shared the mythical view of the world, Plato and Aristotle academies led to a world view based on mathematics and geometrical models.

It was not until the Scientific Revolution of the 16th and 17th centuries that these theories were revisited and a truly scientific model came into being. Nicolai Copernicus, in 1543, is the first to establish that Earth does not occupy a special spatial or temporal position in space-time. Later on, Kepler, Galilei and Newton managed to frame the laws of gravity and mechanics, founding the classical physics.

The last steps were given in the beginning of the 20th century. Albert Einstein's General Theory of Relativity turned space-time into a dynamic medium

in which gravity is a manifestation of the curvature. Soon it was realized that this implies that the Universe could not be static and should be expanding or contracting. Friedmann and Lemaître were the first who worked out the expanding solutions for a homogeneous and isotropic Universe. Their ideas were soon confirmed in 1929 by Edwin Hubble. He measured that distant galaxies are receding with velocities proportional to their distance, which is still a pillar for present day cosmology.

The Hubble Law imply that the Universe would have been smaller, denser and much hotter than the present Universe. This gives rise to the *Big Bang Theory*, where the Universe would have started in a finite point in the past. Nowadays we believe that the Universe formed 13.6 billion years ago from an almost homogeneous mixture of matter and radiation, and it was so hot that even the fundamental interactions where merged. The Big Bag was confirmed in 1965 when Penzias and Wilson detected the cosmic background radiation (CMB) by chance. This is the relic radiation from the epoch when matter and photons decoupled. Since CMB still preserves the properties of such times, we have been able to derive the value of the fundamental cosmological parameters with amazing accuracy. Hence, CMB is one of the most important probe to precision cosmology.

Despite the tremendous impact of standard Big Bang Theories, there are some unresolved issues. Some of them are the near flatness of the Universe, the almost perfect isotropy and the origin of structures. All these issues are solved simultaneously if the Universe suffered and exponential expansion phase. During this cosmic inflation the Universe grew up by a factor of 10^{60}.

However, there are still some unknown pieces of the puzzle. 30% of the total energy of the Universe is due to matter, but only 4% is present in the form of baryonic matter and radiation. Structure would have never been formed without the dominant gravitational influence of a mysterious *dark matter* component. Only sensitive to the gravitational force, it is the insensitivity to the electromagnetic force what makes it unable to emit photons and, though, it is invisible to us. The presence of dark matter was detected indirectly by their gravitational effects, but we have not yet been able to pinpoint its identity.

Also intriguing is the presence of *dark energy*. Discovered ten years ago, it has transformed our view of the Universe. It represents 70% of the total Universe energy budget and is responsible for the accelerated expansion of the Universe. Its identity is a complete mystery for astronomers, though its influence may provide the key towards unraveling the dichotomy between quantum physics and general relativity at high energies. However, the most probable

situation is that of the presence of a cosmological constant. The pressure of this dark energy would be negative, translating into a repulsive gravitational impact. While we have recognized its dominant influence on large scales, its impact on smaller scales remains to be seen.

1.1 Friedman-Robertson-Walker Universes

In the General Theory of Relativity, the *Cosmological Principle* plays a crucial role in constraining the geometry of the Universe. In essence it states that we do not occupy any privileged position in the Universe. In fact, everywhere on the visible Universe should have the same physical conditions such as temperature and density. In other words, the Universe is homogeneous and isotropic on sufficient large-scales.

Formally, the *Cosmological Principle* constraints the shape of the metric $g_{\mu\nu}$. The metric solutions for homogeneous and isotropic spaces take the name of *Robertson-Walker* metric in honor to the mathematicians who proved it, and has the form

$$ds^2 = c^2dt^2 - a^2(t)\left(\frac{dr^2}{1-kr^2} + r^2d\theta + r^2\sin^2\theta\, d\phi^2\right) \tag{1.1}$$

where t is the cosmic time and r, θ and ϕ are the spherical co-moving coordinates. The curvature of space is characterized by the curvature index $k = 0, \pm 1$, and the speed of light in vacuum is $c \equiv 299792.458\, km/s$. The expansion of the Universe is encapsulated in $a(t)$, namely the dimensionless *scale factor*. By convention, at the present time t_0, $a(t_0) = 1$.

Under the assumption that the Universe behaves as a perfect fluid with a metric given in a *Robertson-Walker* form, the *Einstein's field equations* of general relativity leads to the *Friedmann-Lemaître* equations

$$\frac{\ddot{a}}{a} = -\frac{4\pi G}{3}\left(\rho + \frac{3p}{c^2}\right) + \frac{\Lambda}{3} \tag{1.2}$$

$$\left(\frac{\dot{a}}{a}\right)^2 = \frac{8\pi G\rho}{3} - \frac{kc^2}{a^2} + \frac{\Lambda}{3} \tag{1.3}$$

being G is the Newton's gravitational universal constant, p is the pressure, ρ is

the mass density and Λ is the cosmological constant or vacuum energy. These set of two equations describe the expansion and evolution of the Universe. Those models governed by equations 1.2 and 1.3 are known as *Friedmann-Robertson-Walker* Universes.

To solve the density evolution from the Friedmann equations, an equation of state $p = w\rho c^2$ is needed to form a set of three non-linear equations. The major components are matter content (baryonic and dark matter), radiation and dark energy, having $w = 0$, $w = 1/3$ and $w < -1/3$ respectively. In conclusion, each component behaves independently as

$$\begin{aligned} \rho_m &\propto a^{-3} \\ \rho_r &\propto a^{-4} \\ \rho_{DE} &\propto a^{-3(1+w)} \end{aligned}$$

and defines how the total density evolves in ages when only one of them is not negligible. The case of dark energy is a generalization to account for its unknown nature. Particularly interesting is $w = -1$ when Λ is the only source of dark energy, implying a constant energy density $\rho_\Lambda = a^0$ which is related to the vacuum energy.

Dark energy, in the form of cosmological constant, has several strong effects on the evolution of the Universe. A positive cosmological constant will resist the attraction of matter due to its negative pressure. In most universes, it will eventually dominate over the gravitational attraction of matter and will drive the universe to expand exponentially. For a limited rage of values, Λ will never dominate over matter, and therefore, the Universe will re-collapse after some finite time. In the extreme case of a very large cosmological constant, the Universe may not even experience a Big Bang.

Recently, observations began to confirm the existence of a cosmological constant. The most compelling evidences are summarized in fig. 1.1. It shows the combined constraints on $\Omega_{\rm m}$ and Ω_Λ from different and independent methods. In blue, Knop et al. (2003) reports the constraints resulting from the observations of distant supernovae type Ia. This kind of SN allows the determination of its luminosity from the shape of the light curve. Orange color is devoted to the number count of galaxy clusters (Allen et al. 2002), which are a direct probe of cosmology. We will discuss this issue in depth on section 1.4.3. Finally the observations from the CMB the oldest light in the Universe, gives information about the physical conditions when the Universe

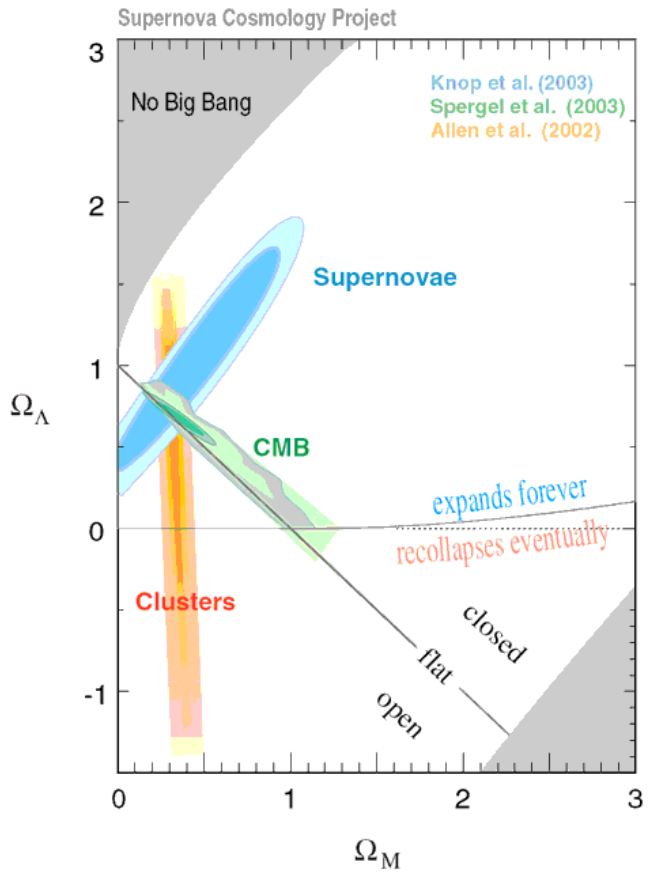

Figure 1.1: Combined confidence regions for Ω_m and Ω_Λ with results from distant supernovae (Knop et al. 2003), WMAP3 (Spergel et al. 2003) and abundance of galaxy cluster (Allen et al. 2002). Credit: Supernova Cosmology Project.

was much younger. As an illustration, Spergel et al. (2003) constraints, which are plotted in green in fig. 1.1, has determined the age and geometry of the Universe among other important parameters.

Since all distances are stretched by the expansion of the Universe, the wavelength of photons traveling through space for a significant period of time must also be affected. This leads to a cosmological redshift z and the consequent loss of energy as light propagates. So, a photon emitted at time t with rest-frame wavelength λ_{em} is observed at the present time with a wavelength λ_{obs} redshifted by

$$1 + z \equiv \frac{\lambda_{obs}}{\lambda_{emission}} = \frac{1}{a(t)} \tag{1.4}$$

the redshift z is of key importance in cosmology because it is a directly observable proxy of distance and time[1].

Edwin Hubble (Hubble 1929) confirmed the expansion on the Universe by means of galaxies receding from us. The proportionality constant between galaxies velocities and distance ($v = Hr$) happen to be the Hubble function, which is simply the ratio of the expansion velocity and the scale factor

$$H_z = \frac{\dot{a}}{a}. \tag{1.5}$$

Its present value H_0 is usually parametrized as a dimensionless constant $h = H_0/(100\, km\, s^{-1}\, Mpc^{-1})$.

To assess the fate of the Universe, it is useful to express energies in terms of the critical density,

$$\rho_{\mathrm{crit,z}} = \frac{3H_z^2}{8\pi G}. \tag{1.6}$$

By definition, the critical density is the density required for the Universe to asymptotically stop expansion at an infinite time. The value it takes at the current epoch is $2.775 \times 10^{11}\, h^2 M_\odot Mpc^{-3}$.

Additionally, we can define other useful cosmological parameters:

$$\Omega_{\mathrm{m,z}} = \frac{\rho_{\mathrm{m,z}}}{\rho_{\mathrm{crit,z}}}; \quad \Omega_{\mathrm{rad,z}} = \frac{\rho_{\mathrm{rad,z}}}{\rho_{\mathrm{crit,z}}}; \quad \Omega_{\Lambda,\mathrm{z}} = \frac{\Lambda}{3H_z^2}; \quad \Omega_{\mathrm{k,z}} = -\frac{kc^2}{a^2 H_z^2} \tag{1.7}$$

that refer to energies in the form of matter, radiation, vacuum and curvature. Hence, the second Friedmann equation (eq. 1.3) can be rewritten into the following closure relation:

$$\Omega_{\mathrm{m,z}} + \Omega_{\mathrm{rad,z}} + \Omega_{\Lambda,\mathrm{z}} + \Omega_{\mathrm{k,z}} = 1. \tag{1.8}$$

When combining equations 1.2, 1.5 and 1.7, the general expansion history is obtained in the form of the *normalized Hubble function.*

[1]For the sake of simplification, it is common to notate the temporal dependence as subscript z, and 0 or none for the present time. Hereafter, this formalism will be applied.

$$H_z^2 = H_0^2 \left(\Omega_{\rm m}\, a^{-3} + \Omega_{\rm rad}\, a^{-4} + \Omega_\Lambda + \Omega_{\rm k}\, a^{-2} \right). \tag{1.9}$$

Notwithstanding, radiation density is only important in the first stages of Universe expansion, when photons and matter are coupled. After the Universe becomes transparent the net contribution of $\Omega_{\rm rad}$ can be neglected. Hence, the normalized Hubble function takes the usual expression

$$E_z = \frac{H_z}{H_0} = \sqrt{\Omega_{\rm m}\,(1+z)^3 + \Omega_\Lambda + \Omega_{\rm k}\,(1+z)^2} \tag{1.10}$$

1.2 Growth of structure

The Universe is far from being homogeneous. In fact, there is an enormous richness of structures depending on the spatial scale we look at, ranging from dwarf galaxies to superclusters of galaxies. The number of abundance of such objects is eventually determined by primordial fluctuations and the overall evolution of the cosmos. In the following sections we review the mathematical methods to describe them.

1.2.1 Power spectrum

In the current view of structure formation we assume that after the first seconds the Universe was not absolutely homogeneous. Indeed, small quantum fluctuations were present in the density field. As the Universe evolved, these small ripples grew up to the present structures. It is very convenient to describe the density field according to the background mean density,

$$\delta(x) = \frac{\rho(x) - \rho_{bg}}{\rho_{bg}}, \tag{1.11}$$

where ρ_{bg} is the background density. This view implies that overdense fluctuations turned out into the collapsed objects, such as galaxies and galaxy clusters. Conversely, the matter was swept away from the underdense fluctuations creating areas of virtual emptiness, the so-called voids. The only prediction about the origin of these ripples comes from inflation, implying that primordial fluctuations behave as a gaussian random field.

A gaussian density field is fully characterized by its power spectrum $P(k)$, which specifies the amplitude of the fluctuations as a functions of their spatial scale. In general, it is assumed that the initial power spectrum is a power-law,

$$P(k) \propto k^n. \tag{1.12}$$

The spectral index n determines the balance between small and large scales power. There is a special case, when $n = 1$, in which the density contrast has the same amplitude when the perturbations enter the horizon. This case is often referred to as the *Harrison-Zel'dovich* (Harrison (1970)) and it is a natural prediction of the inflationary theories.

The primordial power spectrum is believed to change during the evolution Universe. In the early Universe, the fluctuation field is small and the equations of motion can be linearized. During this period, the overall effect on $P(k)$ can be encapsulated in the transfer function, $T(k)$, which gives the ratio of the later-time amplitude mode to its initial value,

$$P(k, z) \propto T^2(k)\, P(k, 0) \tag{1.13}$$

Calculations of the transfer function are a challenge due to the mixture of matter and relativistic particles. For Cold Dark Matter spectrum, Eisenstein & Hu (1999) obtained a fitting formula for a wide variety of cosmologies.

To completely specify the power spectrum, we need to fix the overall amplitude. For $P(k)$ of a given shape, the normalization is fixed as long as we know the value of $P(k)$ at any k. The prescription to normalize a power spectrum involves the variance of the galaxy distribution when sampled with randomly placed spheres of radius R:

$$\sigma^2(R) = \frac{1}{2\pi} \int_0^\infty k^3 P(k) W^2(k, R) \frac{dk}{k}, \tag{1.14}$$

where $W(k, R)$ is the Fourier representation from the distribution of a real space top-hat filter enclosing a mass M at the mean density of the Universe. Historically, the derived value from the distributions of galaxies in spheres of $8\, h^{-1} Mpc$ is taken to determine this normalization, a cosmological parameter known as σ_8.

1.2.2 Evolution in the non-linear regime

Once density fluctuations approach unity, linear theory is no longer valid. The full non-linear solutions are too complex to solve analytically and the power spectrum evolution cannot be describe by an analytical function. In this case, one must rely on numerical simulations to solve the full non-linear solutions. The epoch of highly non-linear evolution depends on the scale of the structure because each object forms at different times scales, as outlined in Peebles (1993). For instance, a simulation of galaxy formation can begin at $z \sim 300$ while the evolution of galaxy cluster must be started no later than $z \sim 50$.

Simulations allow to track the evolution of hydrodynamical gas together with the formation of massive objects. As such, they represent ideal probes for understanding the complex formation history of objects in the Universe. They are often limited by the detailed implementation of physical processes and the computational resources available. Consequently, there are two main approaches to deal with the problem of simulating a given patch of Universe.

The former, and the most common, is to apply all numerical power into solving as much physics as possible for a small number of objects in a relatively small volume. Then, clusters are highly resolved, but the low number of simulated objects give no information about their statistical properties or overall evolution. Without forgetting the fact that some physical processes cannot be accurately simulated yet.

The latter simulations spend the computation resources in increasing the numerical resolution and the size of the box in order to have a large statistical sample of well resolved objects. However, only the most relevant physics are involved instead of "all of it". In this category we may include N-body and non-radiative gasdynamical *adiabatic* simulations. In N-body codes, the total gravitational potential is computed with high accuracy but we get no information from the collisional baryonic content. On the other hand, in *adiabatic* simulations, the equations of motion and the hydrodynamics are solved within the code at the same time. In this sense, the term *adiabatic* does not refer to the usual thermodynamical meaning where no entropy is generated. Instead, it means that non-radiative processes are not considered although entropy is generated by shock waves. The range of validity for its results is indeed limited to the regions where adiabatic contraction/expansion and shock wave heating is the dominant process, i. e. very high density regions such as cluster cores and small-scale collapsed halos, such as galaxies or low mass galaxy groups.

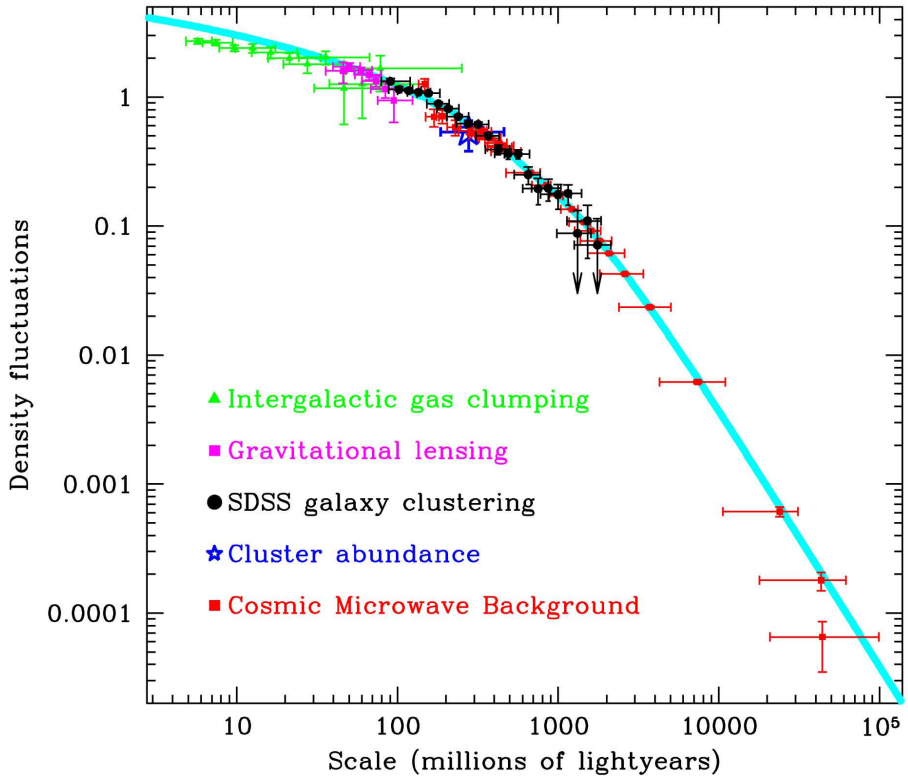

Figure 1.2: Power spectrum derived from observables at different scales. Blue line represents the theoretical expectation of a $\Omega_{\rm m} = 0.3$ and $\Omega_\Lambda = 0.7$ model. Credit: *www.sdss.org*

1.3 Current cosmological parameters

In summary, it is now clear how a set of 6 basic cosmological parameters (Ω_Λ, $\Omega_{\rm m}$, $\Omega_{\rm bar}$, h, n_s, σ_8) completely determines the evolution of a Friedman-Robertson-Walker Universe. In the last years, a great effort has been done to determine the most probable values of the cosmological parameters from several approaches. Such as probing the power spectrum at different scales by means of studying CMB, baryon acoustic oscillations (BAO) galaxy clusters distribution, measuring the geometry at high distances by means of supernovae or even constraining the total mass of clusters by weak lensing. Figure 1.2 shows different measurements of the power spectrum along with a representative theoretical model that reproduce the observational results.

In theory the results from each one should be compatible with the others, however each technique is more sensitive to some of the parameters. For in-

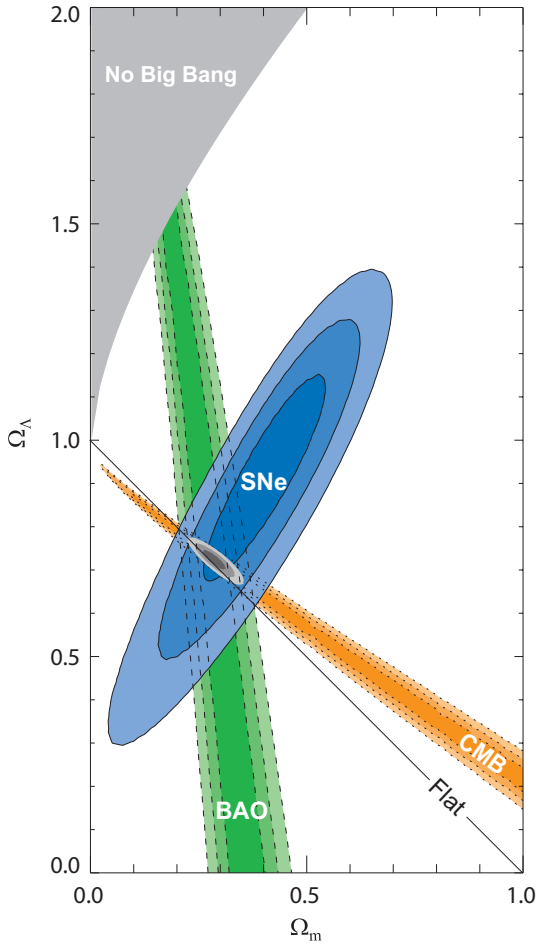

Figure 1.3: Constraints on Ω_Λ and Ω_m from SNe (Kowalski et al. 2008), BAO (Eisenstein et al. 2005) and WMAP5 Hinshaw et al. (2009).

stance, σ_8 has a more important impact on clusters abundance than in CMB due to the fact that large-scales remain almost unperturbed during the Universe's evolution. Yet, their results converge to a joint cosmological model named *concordance model*, which is considered as the starting point for the 21st century's precision cosmology. For instance, we show in figure 1.3 the independent constraints in the $\Omega_m - \Omega_\Lambda$ plane from supernovae, BAO and CMB. According to this model, the Universe is flat and composed of $\sim 74\%$ of dark energy, $\sim 22\%$ non-relativistic dark matter and $\sim 4\%$ ordinary matter. It assumes a Harrison-Zel'dovich initial power spectrum and gaussian primordial perturbations driven from inflation, and a Hubble constant $h \sim 0.70$. In the rest of this section we will review the current status of cosmological models from supernovae, BAO and CMB.

As mentioned above, the geometry of space can be used to constrain the Friedman-Robertson-Walker models. However, discriminating between different values of Ω_k requires very accurate measurements of high distant objects. To this end, the Hubble Space Telescope's key project is devoted to the observation of distant stars, in particular supernovae. In particular the Supernovae type Ia have the rare characteristic of having the same light curve, suggesting that this luminous events can be used as standard candles for cosmological measurements. As a result, the distances are obtained from the dimming of their bright allowing to measure the Hubble constant at low redshifts and the deceleration parameter at high-z. These are the foundations of the so-called `Supernova Cosmology Project`, which was started in 1998 and stated that the cosmological constant has a positive value. A compilation of the latest results can be found in Kowalski et al. (2008).

On the other hand, all the cosmological information and evolution is embedded in the features of the power spectrum. At scales of $\sim 100h^{-1}Mpc$, acoustic oscillations leave their imprint. They arise from the competition between gravitational attraction and gas pressure in the primordial plasma. These oscillations leave their imprint on structures at every epoch of the evolution of the Universe, providing a robust standard ruler from which the expansion history of the Universe can be inferred. BAO were recently discovered by the SDSS, a spectacular confirmation of the current model of cosmology. This poses a tremendous challenge to observations, as surveys must cover large volumes of the Universe. The very large scale of baryon oscillations also confers certain advantages. Structure formation on these scales is rather well understood, and galaxy formation details do not hinder the extraction of accurate results.

The features on the power spectrum at large-scales are imprinted shortly after the Big Bang. In 2001, the *Wilkinson Microwave Anisotropy Probe* (hereafter WMAP) was launched to improve the previous temperature measures and trace the anisotropies printed on the CMB. Then, the anisotropies are used to measure the Universe's geometry, content and evolution to test cosmological models and the inflation theory. WMAP has being obtaining lots of data, providing unprecedent accurate measurements of many cosmological parameters. The results have been published in four data releases collecting the data after the first year of operations (WMAP1), the third year (WMAP3), the fifth year (WMAP5) and the final release so far (WMAP7), being the two latests results very similar. What makes the WMAP releases unique is the fact that not only CMB data are used to determine the best-fit cosmological model. In addition to WMAP data, the final analysis also includes results from other CMB ex-

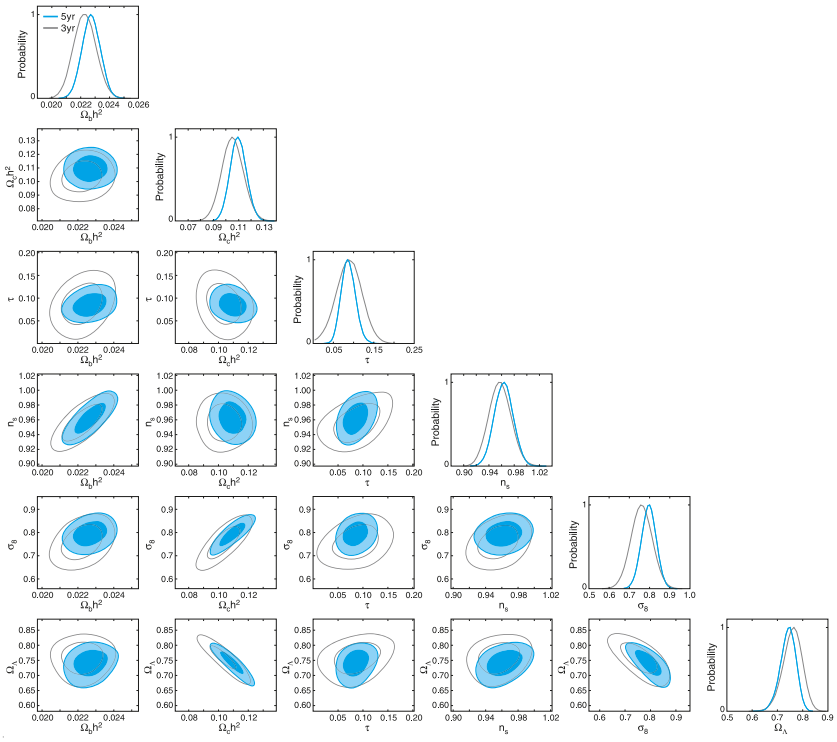

Figure 1.4: Constraints on cosmological parameters from WMAP3 (grey) and WMAP5 (blue). Fig. 7 from Dunkley et al. (2009).

periments, measurements of the power spectrum from galaxy cluster surveys, measurements of the *Ly* α power spectrum, Type Ia supernovae and BAO.

In the first release of WMAP data (February 2003), only the temperature data and analyses from the first year of operations were provided. Much more information and data were provided in the WMAP3 (March 2006), including polarization analysis and maps, temperature maps and an improved error analysis. Finally, WMAP5 (February 2008) is characterized by the improvement in calibration, data and error analysis. In general the basic cosmological parameters are consistent in all the releases and the estimates of these parameters space is better constrained in WMAP5; see fig. 1.4 for a comparison between WMAP3 and WMAP5 results from (Dunkley et al. 2009). Given that the abundance of clusters is very sensitive to $\Omega_{\rm m}$ and σ_8, it may be possible that even the small shifts found between WMAP3 and WMAP5-7 could lead to large discrepancies in the large-scale structure. We will deal this issue in depth on section 1.4.3 and chapter 5.

1.4 Galaxy clusters

Clusters of galaxies are the highest peaks in a cosmic terrain driven by gravitational clustering and represent the largest scale of virialized structures in the Universe. Thus they offer an unique insight into the formation of structures and into the parameters governing their evolution. The internal mix of components within clusters, as well as the space density and temperature distribution function of the most distant and massive clusters, can be used to determine fundamental cosmological parameters. Besides, its evolution and their baryon content are other important measurements for cosmological studies.

Galaxy clusters are believed to form under the gravitational wells created by dark matter in the largest primordial perturbations described in section 1.2.1. They are the largest gravitational-bound structures in the Universe, and so, they probe the large scale end of the power spectrum. As a result they are an excellent tool to constrain cosmological parameters.

When observed visually, clusters of galaxies appear to be a collections of 50 to 10000 galaxies held together by their mutual gravitational attraction. They have velocity dispersions in the order of $\sim 800 - 1000 km/s$, too large to remain gravitationally bound; implying that there must be an additional invisible mass component. The current picture of galaxy clusters and groups is composed by three distinct components:

- A dark matter halo formed by the collapse of the initial perturbations which contains roughly 90% of the total mass in the gravity well. It is, presumably, formed by non-relativistic particles (whatever their nature is) that only interact gravitationally. Due to its nature it is not directly observable and can only be detected through its effect in the dynamics of baryons.

- The Intracluster Medium (hereafter ICM) is a hot diffuse reservoir of gas, $\sim 80\%$ from the total baryon mass, trapped in the gravity created mainly by the dark matter. Typically, the gas number density ranges around $n \sim 10^{-3} - 10^{-1}\, cm^{-3}$ and temperatures are $T = 10^7 - 10^8 K$. It is the most massive visible component of galaxy clusters due to its emission in X-rays; typically $10^{44}\, erg/s$.

- The galaxy population, accessible through optical and infrared observations, was the first component to be discovered in the 18th century (p.e. Herschel (1785)). A cluster usually contains 100-1000 galaxies in a high density region and formed roughly in the same conditions of age and

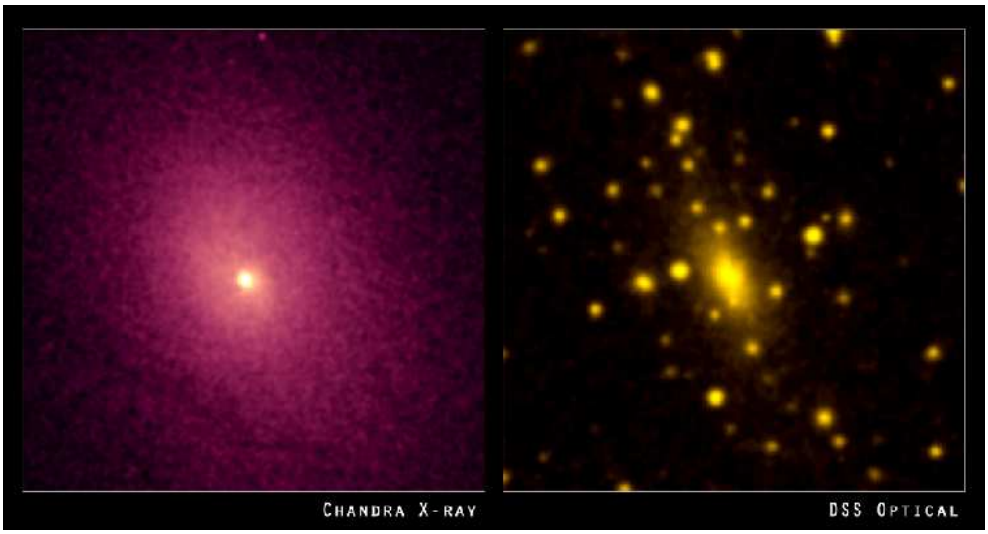

Figure 1.5: The ICM and galaxy population of Abell 2029 core. *Left*: X-ray emission coming from hot gas in the ICM. *Right*: optical emission showing the hundreds of galaxies embedded in the ICM cloud.

metal abundance. As a result, clusters play an important role for galaxy evolution Furthermore, there are a unique kind of galaxy that are formed only in clusters such as *cD* galaxies that can only be found in the center of rich clusters

Only the ICM and the galaxies can be measured directly, from satellite imaging in X-rays or optical respectively. In fig. 1.5 we show an example for this two components in the core of Abell 2029 galaxy cluster. However dark matter, the main contributor to the gravitational potential can only be studied through indirect detection. The best procedure to measure cluster mass is to quantify the distortion by gravitational lensing. When the light from a background source travels through a massive potential its path is diverted, and the apparent image of the background source is magnified and distorted. In summary, the light arc and distorted galaxies detected in optical imaging of galaxy clusters (fig. 1.6) traces the cluster gravitational potential shape and depth.

1.4.1 The Intracluster Medium

The overall formation and evolution determines the main properties of galaxy clusters, and their appearance in X-rays is well understood. During

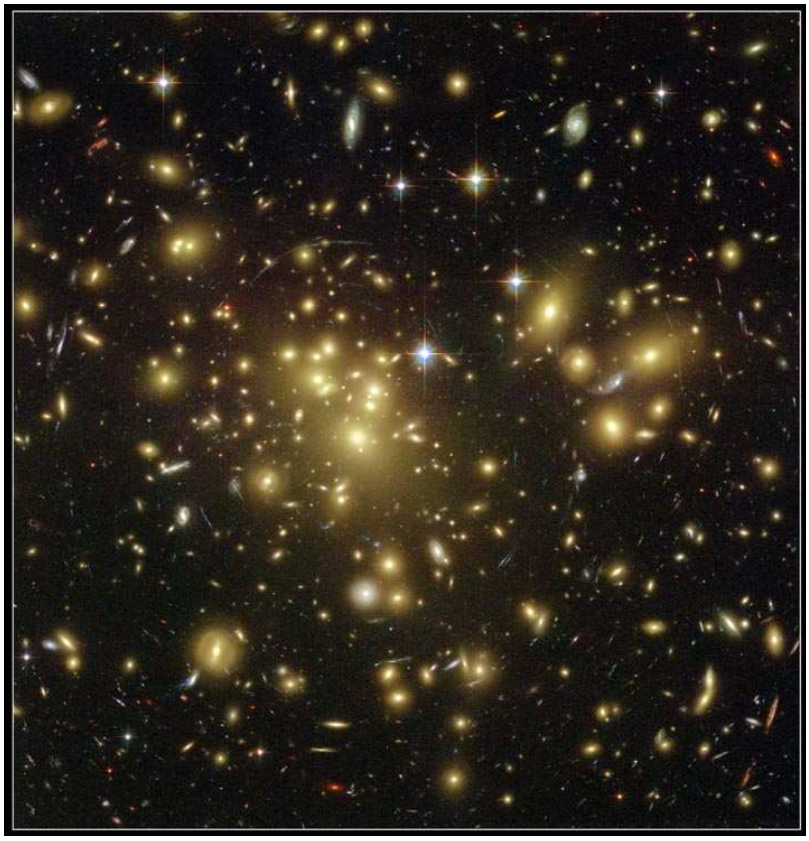

Figure 1.6: Gravitational lensing produced by the cluster potential of Abell 1689 (Benitez et al. 2002).

their formation, gas is dragged from the field along deep potential wells, forming the ICM, and it has heated up through shocks and adiabatic compression produced during the halo contraction.

The ICM is nearly fully-ionized due to the high temperatures created by the dark matter gravitational potential. For instance, Hydrogen and helium are fully stripped of their electrons and heavier elements can retain only a few of them. Besides, the intracluster medium is sufficiently dilute that the effect of any radiation field is negligible and even most of the photons created there can escape without interacting with the plasma. This means that photo-ionization and photo-excitation processes are far less frequent than collisional ionization and excitation. This particular state is commonly known as Collisional Ionization Equilibrium (CIE) and is present in a wide variety of astrophysical sources.

It is important to mention that plasmas close to CIE have level population far different from the Boltzmann predictions for local thermodynamic equilibrium (LTE). Hence, the rate coefficients for all relevant recombination and ionization processes are needed to determine the ionization balance for those plasmas. Once the ionization balance is determined, the spectrum can be calculated considering the various radiation processes.

In the ICM spectrum we may distinguish two components, continuum and lines, which are produced by different photon production mechanisms. The most important processes are *thermal bremsstrahlung* for the continuum emission and the K and L shell[2] transitions for the line emission.

The primary contribution to continuum emission is thermal bremsstrahlung, the emission by a charge when its accelerated in the electrostatic field created by another charge. It is often referred as a free-free emission in the sense that the transitions occur between unbound energy levels, and so, the energy of the emitted photon is not fixed to a given wavelength. The total power produced by pure bremsstrahlung emission in $erg\,cm^3\,s^{-1}$ is

$$\epsilon_{bol} = 1.4 \times 10^{-27}\, n_e\, n_i\, Z^2\, \bar{g}_B\, T^{1/2} \tag{1.15}$$

where n_e and n_i are the electron and ion densities, Z is the metal abundance, $\bar{g}_B$ is the frequency average gaunt factor which is ~ 1 and T is the plasma temperature. However, this naïve approximation is far from realistic in diffuse plasmas at $T \lesssim 10^7 K$. Nevertheless, for colder regimes the continuum emission is produced not only by bremsstrahlung, also recombination (free-bound emission) and two photon decay of metastable levels determine the final shape of the continuum.

Unlike continuum, line emission comes from a number of atomic processes. They are mainly formed by collisional excitation, radiative and dielectronic recombination, inner shell collisional ionization, and radiative cascades. Though they are heavily dependent from metal abundance and are particularly suited for determining elemental abundances, ionization state and temperature. In spite of the large number of atomic reactions necessary for an accurate evaluation of ionization balance, roughly only 8 elements are responsible for the strongest transitions. Some of this elements are iron (Fe XXVI, Fe XXV, Fe XXIV, ...), sulfur (S XXVI and S XXV), silicon, magnesium and neon. A detailed discussion can be found in Brickhouse et al. (1995) or Kaastra et al. (2008).

[2]In atomic notation it refers to states with principal quantum number $n = 1, 2$

1.4.2 Self-similar model

Since gravity does not have any preferred scale and we can assume hydrostatic equilibrium between gas pressure and gravitation, all clusters and groups are scaled versions of the same object. Under these hypothesis, cluster properties are related to each other following equations 1.4.2. The derivation of the self-similar scaling relations for a spherical top-hat collapse can be found in appendix A[3].

$$\begin{aligned} E_z\, M_{\rm tot} &\propto T_{\rm X}^{3/2} \\ E_z\, M_{\rm tot} &\propto (E_z\, Y_{\rm X})^{3/5} \\ E_z^{-1} L_{\rm X} &\propto T_{\rm X}^{2} \\ f_{\rm gas} &\propto T_{\rm X}^{0} \\ f_{\rm gas} &\propto M_{\rm tot}^{0} \end{aligned} \tag{1.16}$$

X-ray observations confirmed the existence of the scaling relations (e.g. Edge & Stewart (1991), Fabian et al. (1994)), however observed properties do not follow the prescription described by the self-similar model. One of the best examples comes from the $L_{\rm X} - T_{\rm X}$ relation which not only has a significant steeper slope for observed clusters, mainly due to an excess of entropy in theoretical predictions (Voit 2005b), but presents a bimodal behavior when galaxy groups are also taken into account (see fig. 1.7).

Our understanding of the similarity breaking remains incomplete because including galaxy formation in cosmological models of cluster formation is a formidable computational challenge. Sophisticated hydrodynamical techniques are now able to model the formation of the first stars but are far from been able to track in detail the formation of an entire galaxy.

Traditionally, radiative cooling and feedback are considered the responsible for such differences. For instance, those processes are radiative cooling or energy feedback from AGNs, supernovae, etc. However other facts must also be taken into consideration. Firstly, not all the phenomenological assumptions are accomplished on real clusters. As an example, Ascasibar et al. (2003) points out that clusters are not isothermal even when preheating or thermal cooling are not enabled. Secondly, there is an intrinsic scatter in the scaling relations due to the different formation histories of elements of the same mass.

[3]A more extensive discussion can be found in Voit (2005a) and Ettori et al. (2004a) for instance.

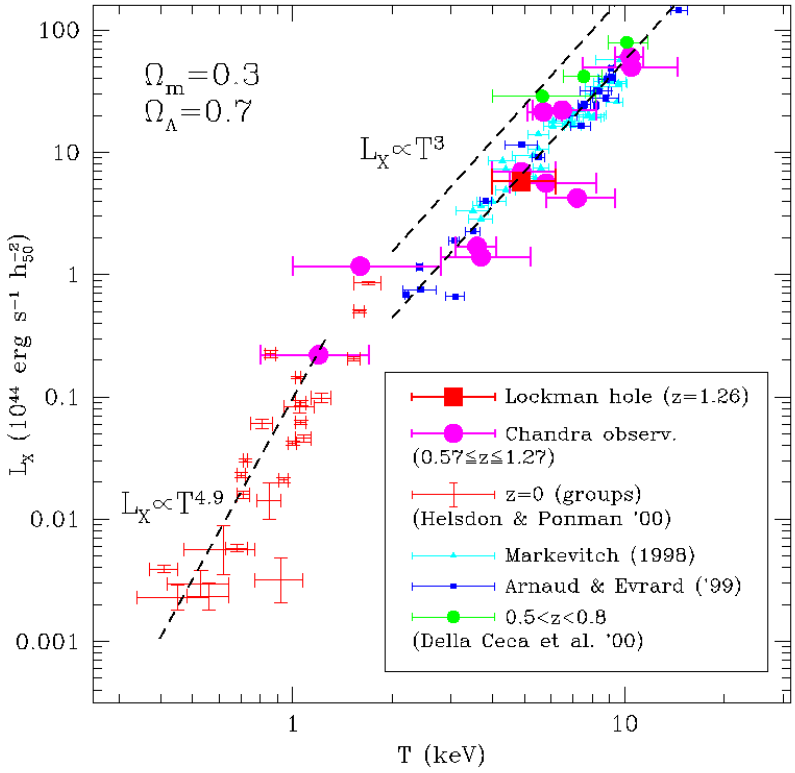

Figure 1.7: $L_X - T_X$ relation for clusters and groups at $z < 1$. Taken from Rosati et al. (2002).

Measurements of how scaling relations evolve with redshift allow to test entropy-generating models and further constraint cosmological parameters. Besides, the number of observed high-redshift clusters have soared during the recent years.

1.4.3 Cosmological dependence for clusters

In the hierarchical collapse scenario for structure formation, the number density of collapsed objects as a function of mass and time is a sensitive probe of cosmology. Galaxy clusters provide a powerful tool to estimate the cosmological parameters. In particular, the sensitivity of cluster abundance to the distribution of energy matter in the universe (Ω_m and Ω_Λ) is moderate and to the normalization of the power spectrum σ_8 is very strong. Whereas, for Ω_{bar}, h and n it is weak or non-existent. The growth rate of clusters depends primarily

on $\Omega_{\rm m}$, although at $z \approx 1$ matter ceases to dominate and dark energy takes over. Thus, the Universe is not decelerating because of the matter density and eventually its expansion accelerates due to the gravitational repulsion.

Applied to clusters of galaxies, dark energy prevents halos to accrete matter at low redshifts. Hence, halos show infall or outflow profiles in the outskirts depending on their masses, i.e. Prada et al. (2006) and Ascasibar & Gottlöber (2008). However, the net effect of Ω_Λ in clusters of galaxies is minor compared to the matter density and the normalization of the power spectrum. Araya-Melo (2008) outlines the importance of $\Omega_{\rm m}$ in the mass accretion history of clusters. In low $\Omega_{\rm m}$ cosmologies most evolution takes place by accretion at early times, followed by massive mergers at high redshifts. Whereas at high $\Omega_{\rm m}$ such mergers are more frequent at recent epochs.

There has been much effort to exploit the strong dependence of cluster abundance to σ_8. In the past, the local population of galaxy clusters has been used to constrain these parameters. However, there is a degeneracy between $\Omega_{\rm m}$ and σ_8 (Reiprich & Böhringer (2002), Allen et al. (2003), Rozo et al. (2010)). The main obstacles to accurately measure σ_8 are the systematic uncertainties in the estimates of clusters' mass. Perhaps the largest uncertainty comes from the relation between the observed cluster mass and a more easily observable proxy, the temperature. Henry (2004a) outlines that much of the scatter among reported cluster σ_8 measurements is derived to the observed mass-temperature relation normalization.

However, at this time, the $M_{\rm tot} - T_{\rm X}$ relation is becoming more reliable for two main reasons. First, clusters masses estimates have been improved. There are three main ways to obtain the cluster masses: weak lensing observations, X-ray observations assuming virial equilibrium and numerical simulations. Weak lensing determines mass and temperatures independently. X-ray estimates require a careful selection of clusters, excluding non-relaxed and cool cores. Simulated masses need no correction since they are known from the summing of cluster particles. Historically these three methods have not always agreed, but recent techniques suggest convergence to the true solution, as mentioned in Henry et al. (2009). Besides, the trouble to model X-ray spectra of clusters with a single-temperature model has to be taken into account. Observed temperatures of clusters had historically differed significantly from the simulated ones, no matter the temperature definition used: volume-averaged, mass-weighted, etc; as we explain in chapter 3. Although a cluster spectrum is a composition of plasmas at different temperatures and metallicities, the ICM temperature is usually measured by fitting an observed spectrum without taking into account the energy dependence on the effective telescope

area. Recently, Vikhlinin (2006) provided a fitting formula to accurately reproduce a multi-plasma spectrum with a single spectroscopic temperature for the most commonly used detectors. This algorithm makes it possible to consistently compare numerical clusters with observations and can also be applied to deprojection analysis of objects with temperature gradients.

1.4.4 Future projects

Since any model of structure formation must explain both the tiny ripples in the CMB temperature across the sky and the large-scale structures we see in the Universe today, the combination of these two probes is especially powerful. Together, we are able to probe the power spectrum of fluctuations at small and large scales; the former by photons coming from an epoch when the Universe became transparent (CMB), and the latter providing information about the evolution of those ripples. To this end we need information from surveys of galaxy clusters at high redshifts for two main reasons. First, the larger the clusters observed the less random noise we may have on the power spectrum at large-scales. Besides, pushing observations to higher redshift probes the evolution of cluster abundances and breaks the degeneracy between $\Omega_{\rm m}$ and σ_8 (seen on section 1.4.3).

Until recently, most astronomical researches have focused on small samples of cosmic sources. Over the last two decades, advances in technology have made possible to undertake large-scale sky surveys. Motivated by this scientific progress, a number of even more advanced projects will be launched in the near future. The most important are:

- BOSS will map the spatial distribution of luminous galaxies and quasars to detect the characteristic scale imprinted on the BAO in the early universe.

- KAOS is a multi-object spectrograph designed for the 8-meter Gemini telescopes. It is conceived to study galaxy evolution and to measure the physical length scale of the BAO between $z = 1$ and $z = 3$.

- LSST is a wide-field telescope designed to obtain multi-band images. One of its main objectives is to probe dark matter and energy by observing weak lensing of galaxies as a function of redshift, and to obtain light curves of supernovae in several photometric band.

- DES, which will begin at the fall of 2010, is designed to probe the origin of the accelerating universe. It is intended to make measurements of dark energy by means of optical imaging survey using four independent techniques: counting galaxy clusters, weak lensing, supernovae redshifts and BAO.

- JPAS is a deep large-area survey that will improve the current BAO results. It is a narrow-band photometric survey to determine the galaxy distances on the basis of photometric-redshift technique.

However, the most promising prospect to detect clusters at high redshift lies on the SZ effect. High energy photons from the CMB suffer from inverse Compton scattering on their way through a cluster, which increases their energy to distinct frequencies in radiowaves. Therefore, galaxy clusters appear as hotspots in SZ mappings. Since SZ is a scattering effect its signal is almost independent of redshift, being a very robust method to detect high redshift clusters. At present, some groups have already begin to survey the sky of clusters using SZ. Some of the most relevant projects in the future have already seen their first light:

- South Pole Telescope: a 10-meter diameter telescope operating at the NSF South Pole. The telescope is designed for conducting large-area millimeter and sub-millimeter wave surveys of faint, low contrast emission, as required to map primary and secondary anisotropies in the cosmic microwave background.

- Atacama Cosmology Telescope (ATC): a 6-meter telescope in the Atacama Desert, the driest place in the world, in the north of Chile. It is designed to make high-resolution, microwave-wavelength surveys of the sky. At ATC resolutions the SZ effect should be prominent, and it is expected to detect on the order of 1000 such clusters.

- PLANCK: is a space observatory placed in the Lagrangian point L2, at 1.5 million Km from Earth. Apart from its primary objective, to observe the anisotropy in the CMB with high sensitivity and angular resolution, it is a unique tool fro observing galaxy clusters by their SZ-signature. It is going to increase the budget of high-redshift galaxy clusters with an all-sky coverage.

Together with follow-up measurements in visible and X-ray light, SZ would provide a picture of the evolution of structure in the universe. Among other

things, this would improve our understanding of the evolution of galaxy clusters which seems to be a dominant component of the universe.

1.5 Motivation of this thesis

In the last 10 years, the picture we had from galaxy clusters has undergo a terrible change. Clusters are the biggest virialized objects in the Universe, and hence are the best proxy for the large-scale end of the power spectrum. The advent of XMM-Newton and CHANDRA satellites has shed light on their physical properties at low and intermediate redshift, although the number of objects observed is too small for statistical studies. In the following years, several grand challenge instruments are projected (see section 1.4.4) to survey the sky in search of high redshift clusters by X-ray and SZ emission. With this work we intend to establish the first stone in the future interpretation of these projects that will eventually constrain the cosmological parameters even more.

The aim of this thesis is to achieve a deep insight in the properties of such clusters, by means of a detailed analysis of simulations in different cosmological scenarios. In particular we will focus on the intrinsic scatter and the evolution of their adiabatic scaling relations. In addition, we revisit the theoretical expectations for abundance of clusters in different cosmologies, compared to the observational measurements.

The study of intrinsic scatter in their scaling relations is still an almost unstudied issue because of the large statistical sample required. To this end, we have performed a series of high resolution adiabatic simulations which trace the evolution of dark matter and gas from primordial fluctuations until the present time. Each simulation mimics the formation of the Universe in different ΛCDM models. For the sake of comparison, the initial seeds are the same avoiding large variations due to cosmic variance. The number of resolved clusters varies depending on the cosmology, but in all cases it is larger than similar studies on the subject (Stanek et al. (2006), Ettori et al. (2004a), Ikebe et al. (2002)).

The MARENOSTRUM Numerical Cosmology Project

The cosmological simulations of big patches of the Universe is one of the greatest challenges for computational astrophysics. The amount of resources, both human and technological, to accomplish this task often require the cooperation of several international institutions. The MARENOSTRUM Cosmology

Project (hereafter, MNCP)[4] started as a collaboration between the *Universidad Autónoma de Madrid* and the *Astrophysikalisches Institut Potsdam* to perform a series of high-quality simulations of the Universe. Later, other institutions joined the collaboration. These are *New Mexico State University*, *University of Chicago*, *Jacobs University of Bremen* and *The Hebrew University of Jerusalem*.

The MNCP makes use of the exceptional capabilities of the MARENOSTRUM supercomputer, beginning during the testing period of the system. Hosted by the *Barcelona Supercomputing Center*, this facility was the largest in Europe and the 5th largest in the world when it was officially inaugurated in 2004. At the present time, the MARENOSTRUM supercomputer is a 10,240-processor IBM machine with 20 Tb of main memory and 260 Tb of storage, and is able to perform more than 94 trillion operations per second.

Together with MARENOSTRUM, other supercomputers are used in the MNCP to store and analyze the simulation's data. These are the *Jüelich Multi-Processor* (JUMP), a 1312-processor machine with 5.2 Tb of main memory, and the HLBR2, with 4096-processor and 17.5 Tb of main memory. What both computers have in common is a suitable shared-memory architecture which allows the execution of parallel programs in OpenMP and MPI, greatly simplifying the analysis of large amount of data.

The primary objective of MNCP is to study the properties of several kinds of objects which form the large-scale structure of the Universe. To this end, two different simulations are performed focusing at different scales within the cosmic web using the cosmological code GADGET-2. These are:

- The MARENOSTRUM *Universe*: the first simulation performed under this project, run on 2004 during the MARENOSTRUM testing period. It is a 2-billion particle adiabatic cosmological SPH simulation of a patch of the Universe of $500\,h^{-1}Mpc$ on a side, in a WMAP1 cosmological model. This simulation took ~ 500 hours to finish on 512 processors, consuming more than 29 years of computation. The result is the largest SPH simulation performed so far. It has an unprecedented large number of clusters of galaxies and voids, and makes of it an ideal simulation to study large-scale structure in both high and low density environments. A snapshot of the gas density distribution at $z = 0$ is shown on figure 1.8.

- The MARENOSTRUM *Galaxy Formation Simulation*: This simulation focuses on the formation of galaxies at high redshifts. To this end, the

[4] MNCP webpage: http://astro.ft.uam.es/MareNostrum

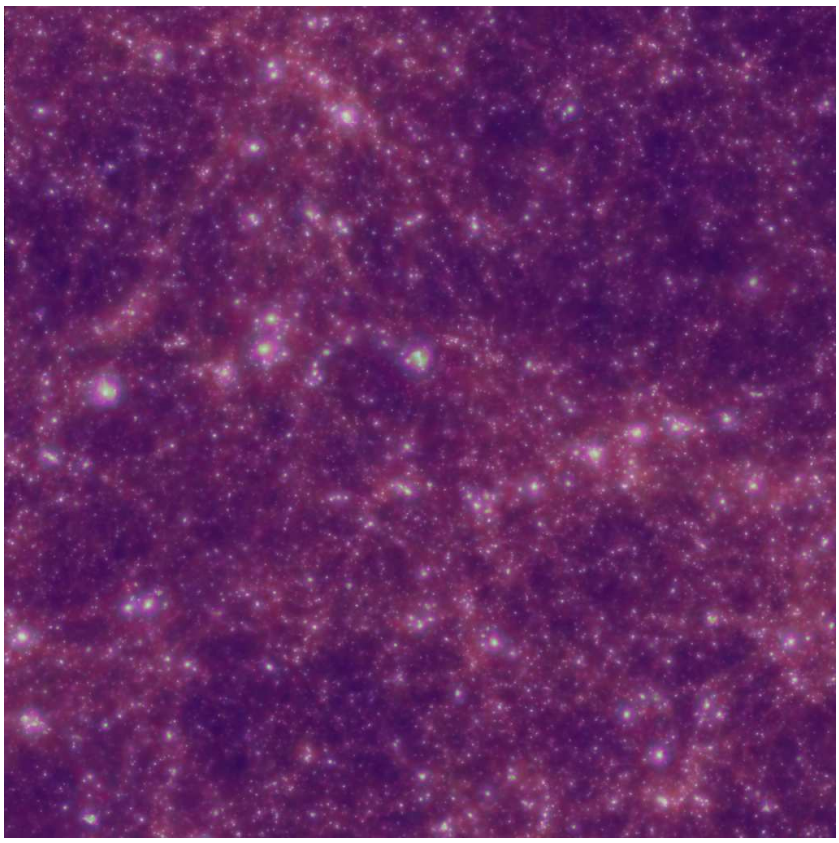

Figure 1.8: Color map of gas density in MUC at $z = 0$. Bright areas correspond to denser gas, while dark ones are low-density environments.

volume is reduced to a box of $50\,h^{-1}Mpc$ on a side which is filled with 2 billion particles equally divided among dark matter and gas. Radiative cooling, star formatting, feedback and metallicity evolution have been included, given the critical role that these processes play on galaxy formation. Simulating a vast number of galaxies with a high resolution and full physics until the present time requires a computation time much larger than any reasonable availability usage on any supercomputer. For this reason the simulation was not run until $z = 0$ but to a earlier epoch consistent with the predictions of detections in the future years, in particular from $z = 60$ to $z = 0$.

As a side effect, the same simulation was performed by the *HORIZON project*[5] using an alternate software, the grid-based code named RAMSES, leading to the chance of comparing the convergence of results.

[5]HORIZON webpage: http://www.projet-horizon.fr/article325.html

1.6 Thesis outline

In this thesis we present the results of high resolution numerical simulation of galaxy cluster formation. We have done five SPH cosmological simulations using the numerical code GADGET2 (Springel 2005), which employs an explicit entropy-conserving formulation (Springel & Hernquist 2002). In this simulations, radiative physical processes have been disable in order to use all computational power to increase the resolution and simulated volume. We will get volume-complete datasets with a large number of high-resolution clusters. The main advantage is that clusters will have with different formation histories, with the only drawback is that our model will not describe accurately their inner cores.

In this work we will present systematical analysis of the X-ray scaling relation in WMAP-based cosmologies. The first part of this thesis is devoted to an overview of the current cosmological and numerical status. Chapters 1 offers an overview of the basic physical concepts necessary to describe galaxy clusters and their properties. A thorough discussion of the numerical experiments performed and the cluster samples used is given in chapter 2. Chapter 3 is devoted to the computation of X-ray properties. First, we describe how X-rays properties are computed in SPH simulations. Then, we assess the numerical uncertainties of the scaling relation with different resolution.

The second part of this work present the analysis of the scaling relations and cluster datasets obtained. Chapter 4 contains the results of the intrinsic scatter of scaling relations for different cosmological models. We also determine both the overall intrinsic and the marginal scatter for each scaling relation. In chapter 5, we prove that cluster abundance of WMAP3 is hardly compatible with observations which is partially solved by increased the normalization of the initial power spectrum. In chapter 6 we investigate the evolution of the scaling relation for the MARENOSTRUM Universe, our simulation with higher resolution.

Chapter 7 contains a summary of conclusions and future prospects.

Chapter 2

Description of simulations

Computer, compute to the last digit the value of pi.

TOS: Wolf in the Fold, Mr. Spock

In this chapter, we will describe the numerical code and cosmological parameters to set up the simulations that we will use throughout simulation.

2.1 The code

The simulations used in this work were performed by the GADGET-2 numerical code[1] developed by Springel (2005). In this code, both collisionless dark matter and the gaseous fluid are represented as particles, allowing self-gravity of both components to be computed with gravitational N-body methods. GADGET-2 solves the Poisson equation for gravitational forces by using a hybrid method called TREEPM algorithm. The potential is splitted into a long-range part and a short-range one and solved independently. The former can be efficient and accurately solved with a Particle-Mesh while the latter is computed by a TREE algorithm which divide the space into smaller computational cells.

The hydrodynamics are solved by using an entropy conserving scheme of the smoothed particle hydrodynamics method (SPH). As for dark matter particles, gas kinematics are defined with coordinates $\overrightarrow{r_i}$, velocities $\overrightarrow{v_i}$ and masses

[1]Publicly available from http://www.mpa-garching.mpg.de/gadget/

m_i. The thermodynamics state of each fluid element is defined in terms of its entropy per unit mass s_i which ensures the conservation of entropy in all situations, as found at Frenk et al. (1999). SPH uses a kernel interpolation technique (Monaghan 1992) to define the continuous quantities from the discrete distribution of gas particles. Consequently, the value of a fluid quantity in any point of space can be computed from the particle distribution. For instance, the density can be expressed as

$$\rho_i = \sum_{j=1}^{N} m_j \, W(|\overrightarrow{r_{ij}}|; h_i), \tag{2.1}$$

where $\overrightarrow{r_{ij}} \equiv \overrightarrow{r_i} - \overrightarrow{r_j}$ and $W(r; h)$ is the smoothing kernel. Values for density, internal energy and smoothing length are computed by GADGET for all particles.

The most important feature of the GADGET code is the highly efficient work-load balanced on different tasks, which makes of it a massively parallel code. The approach is to treat different scalar CPUs as independent computers, each of them having their own physical memory, and each of them running a separate instance of the application. Such parallel programs have the potential to be scalable up to very large number of processors although, in practice, it is only possible when all processors have similar work-load and the communication between them is minimized. The key resides on dividing the full simulation into parts that are suitable for distribution among individual processors. A commonly taken approach is to decompose the computational volume into a set of domains, each one assigned to one processor. GADGET-2 uses a space-filling fractal to map 3-D space on to a 1-D function, the so-called Peano-Hilbert curve. An important property of the Peano-Hilbert curve is that points close along the curve are, in general, close in 3-D space. As a consequence, efficient domains can be set by chopping off the curve into pieces.

The result is a highly scalable and customizable parallel algorithm, allowing to perform simulations with a very large number of particles and volumes using many processors. Besides, it is fully adaptive both in force computation and in time stepping (i.e. each particle can have its own mass and time step).

Name	$\Omega_{\rm m}$	$\Omega_{\rm bar}$	Ω_Λ	h	σ_8	n
MUC	0.3	0.045	0.7	0.7	0.9	1
MUCL	0.3	0.045	0.7	0.7	0.9	1
MUW	0.24	0.0418	0.76	0.73	0.75	0.95
MU2W	0.24	0.0418	0.76	0.73	0.75	0.95
MUWHS	0.24	0.0418	0.76	0.73	0.8	0.95

Table 2.1: Cosmological parameters for all simulations performed.

2.2 Numerical experiments

In order to study the large-scale structure in different cosmologies, we have performed adiabatic simulations for each cosmological backgrounds. In essence, all the work reported in this thesis is based on the analysis of a set of simulations performed in different cosmological frameworks. Undoubtedly, the most probable model is roughly constrained to a flat Universe with $\sim 30\%$ matter content, however large discrepancies are still present. In particular, σ_8 represent a key parameter as it is the main responsible for setting the cluster abundance so that it may have a significant effect on galaxy clusters in different cosmologies. The cosmological dependence of these simulations, as well as notation throughout the rest of this thesis, is summarized in table 2.1. In all cases we keep track of the non-linear evolution of structures in gas and dark matter within a co-moving box of 500 $h^{-1}Mpc$ since $z = 40$.

The foundation for all simulations is MARENOSTRUM *Universe* (MUC), the largest SPH simulation done so far. Firstly, we had performed two simulations (MUC and MUCL) soon after the WMAP1 data release. After the update on cosmological parameters by WMAP3 two more numerical experiments were done, MUW and MU2W, to state for the cluster properties in the new cosmological scenario. At this point, several authors reported inconsistencies between the reported value of $\sigma_8 = 0.75$ in WMAP3 and other independent measurements. To mention some, the derived σ_8 only from weak lensing in Pedersen & Dahle (2007) and Lesgourgues et al. (2007) is $\sigma_8 \sim 0.88$; at the same time that Rozo et al. (2007) estimates $\sigma_8 = 0.92$ from the SDSS. However the most recent measurements independently states that a slightly bigger normalization, i.e. $\sigma_8 \sim 0.8$ from Evrard et al. (2008) and Rozo et al. (2010), would suffice to agree WMAP3 and cluster properties.

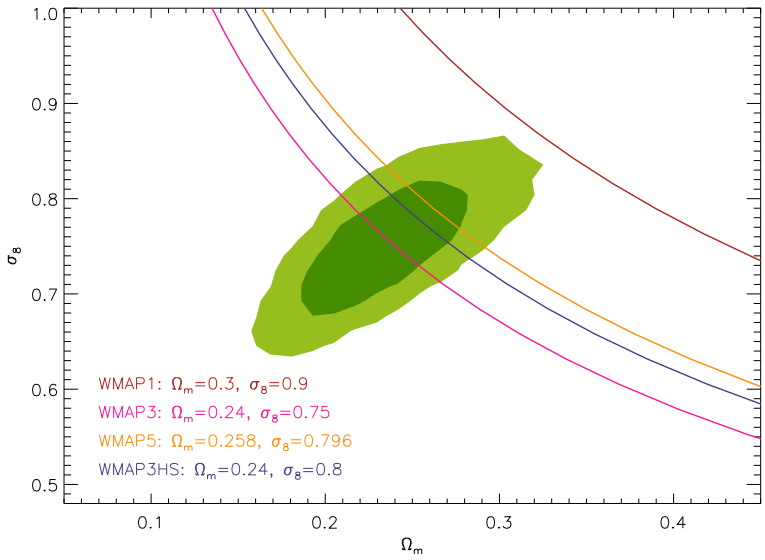

Figure 2.1: Constraints for σ_8 and $\Omega_{\rm m}$. Contours represent 1σ and 2σ confidence levels for WMAP3. Degeneracy $\sigma_8\Omega_{\rm m}^{-0.5}$ is overplotted for the cosmological models used in the MNCP and WMAP5.

Finally, we decided to perform a final simulation with a higher normalization but still compatible with WMAP3. As a result, MUWHS is a repeated realization of MUC in a WMAP3 cosmology, but with a more higher initial power spectrum ($\sigma_8 = 0.8$) (Yepes et al. 2007). The main purpose of MUWHS is to map the $\Omega_{\rm m} - \sigma_8$ region between WMAP1 and WMAP3 with a feasible cosmological scenario. It also alleviates the tension between observations of clusters abundance and WMAP3 as we reported in Yepes et al. (2007).

Very recently, new data from the fifth and seven-year WMAP has been reported by Dunkley et al. (2009) and Hinshaw et al. (2009), respectively. As we mentioned in chapter 1.3, all cosmological parameters are consistent with WMAP3 results. However, the variations in σ_8 have a dramatic effect on the cluster abundance. In figure 2.1 we plot the contours at 1σ and 2σ confidence levels taken from the Markov chains of WMAP3, kindly provided by Licia Verde. We have overplotted the models of equal number counts of clusters for all cosmologies considered in this thesis. MUWHS is very close to the estimates from WMAP5. Besides, WMAP1 and WMAP3 establish reasonable upper and lower limits in σ_8 values.

Name	# Particles	m_{gas}	m_{dm}	ϵ	$z_{initial}$
MUC	2×1024^3	0.145	0.824	15	40
MUCL	2×512^3	1.16	6.59	50	40
MUW	2×512^3	1.08	5.12	50	40
MU2W	2×512^3	1.08	5.12	50	40
MUWHS	2×512^3	1.08	5.12	50	40

Table 2.2: Parameters of MARENOSTRUM simulations including: total number of particles, m_{gas} and m_{dm} are masses of gas and dark matter, in units $10^{10}h^{-1}M_{\odot}$; ϵ is the Gravitational Plummer equivalent smoothing scale in kpc, in co-moving values (see text) in units of $h = 1$ and initial redshift.

2.2.1 Initial conditions

Table 2.2 summarizes the numerical parameters adopted. The spatial force resolution in MUC was set to an equivalent Plummer gravitational softening of comoving $15\,h^{-1}kpc$, while for MUCL, MUW, MU2W and MUWHS it was set to $50\,h^{-1}kpc$. The SPH smoothing length is determined by the distance of the 40th nearest neighbour of each gas particle. In all simulations, we have adopted the largest between gravitational and SPH softening.

The initial conditions were chosen to minimize the cosmic variance among simulations. The first simulation performed, MUC, has been taken as a model to make the others. It is a random realization of the formation of large-scale structure in a cubic box of $500\,h^{-1}Mpc$ on a side in a WMAP1 cosmology.

MUC has 1024^3 dark matter particles of equal mass $m_{dm} = 8.24 \times 10^9\,h^{-1}M_{\odot}$ and 1024^3 gas particles of $m_{gas} = 1.45 \times 10^9\,h^{-1}M_{\odot}$. The original initial conditions for MUC has 2048^3 independent harmonics, allowing to simulate up to 2048^3 particles. In fact, the running of the whole simulation at full resolution required too many resources. For this reason, it was downgraded to a single mass simulation with 1024^3 Fourier modes. However, we still have the chance of re-simulating individual objects.

To account for any resolution effect we decided to make simulation MUCL by downgraded once more the original conditions. Which leads to the same unconstrained realization than MUC but keeping half the particles: 2×512^3 (Gottlöber & Yepes 2007).

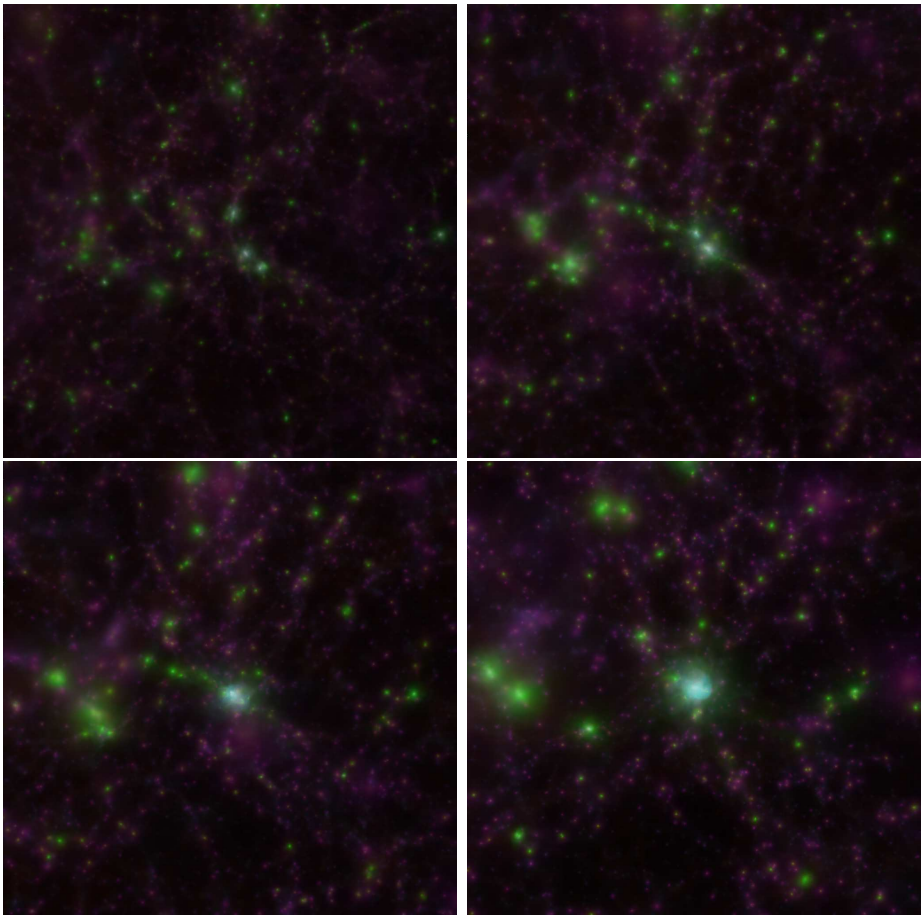

Figure 2.2: Gas density maps around the biggest cluster on MUC. Redshifts are $z = 1.5, 0.75, 0.5, 0$ from top to bottom and left to right.

In order to test whether the clusters on MUC are resolved or not, we re-simulated eight selected objects from the simulation at the highest resolution. The procedure, described at Klypin et al. (2001), sets a layer of multi-mass particles around the cluster. The object lays in the area of most refinement but the space around it is probed by more massive particles, so that the cluster is formed as if the box were effectively mapped by 2048^3 light particles. We only take them into account for a resolution comparison in section 3.4.1.

Given that WMAP3 has the lowest σ_8 value that we take into account, we have performed two simulations to increase the statistical of clusters. Simulations MUW and MU2W has the same resolution with MUCL (2×512^3) but in the precise WMAP3 cosmology. In MUW, the initial conditions are generated to have the same random phases as MUC, so that it can be considered as a

WMAP3 version of MUCL. MU2W was created with a random initial seed to result in a different patch of the Universe. Together we are also allowed to study the effects of cosmic variance as well as we have a better estimate for scatter. The latter will be crucial in chapter 4 where we analyze scatter in scaling relations.

Last but not least, we decided to simulate an intermediate cosmological model with a σ_8 parameter in better concordance with abundances estimates (i.e. Li et al. (2006), Rozo et al. (2007), McCarthy et al. (2007), Evrard et al. (2008)). Therefore, MUWHS has the same resolution and random phases of MUCL and a set of cosmological parameters still consistent with WMAP3, within 1σ, although using a higher σ_8.

2.3 Halo finder

Even though the collapsed structures can be seen in almost any snapshot of a simulation, locating those structures from a three-dimensional particle distribution is a challenging task. Currently, there are several methods to accomplish this task, each one having its own merits and drawbacks. However, none of them were designed to treat a large number of particle in a reasonable time, as it had been the MARENOSTRUM simulations. Consequently, we must have developed our own technique to gather all the particle information around every cluster, basing on previous well-known halo finders. As a side effect, each cluster data is stored in a compact and portable format allowing to further analysis without needing large computational resources. The halo finding for MARENOSTRUM clusters is divided into two steps.

Firstly, we have created a parallel version of a hierarchical friends-of-friends (FOF) as described on Klypin et al. (1999). On a first step we build the minimum spanning tree (MST) for the distribution of gas and dark matter particles. The MST of a point in an euclidean distribution of particles is the graph that connects all particles. An important characteristic is that the total length that connects the particles is minimized, and unique. Then, a topological sorting algorithm transforms the tree into a linear sequence of particles which is the representation of a halo. Finally, FOF halos are extracted by simply chopping off the list at the desired linking length.

For the MARENOSTRUM simulations, we have drawn up the FOF catalogs of dark matter at four different linking length. The starting one is the largest with a linking length of 0.17 times the mean interparticle separation which roughly

correspond to objects with virial overdensity at $z = 0$ (Gottlöber & Yepes 2007). Note that this linking length is obtained when the conventional value 0.2 is scaled by $(\Delta_c/\Omega_{\rm m})^{-1/3}$. The others catalogs divide the linking length by a factor 2, 4 and 8 to sample more compact objects with overdensities 8 times larger each one. With this multiples catalogs at different lengths we locate all halos and their substructure.

Some structural properties of this halos are reported in Gottlöber & Yepes (2007) for MUC. In summary, they show that gas tends to be much more spherically distributed. More massive objects are less spherical in both gas and dark matter. At $z = 0$, the spin of the gas component is larger than the dark matter distribution although the differences are smaller for $M_{\rm vir} > 5 \times 10^{14} h^{-1} M_\odot$ halos. At higher redshifts, $z = 1$, both components rotates with similar angular velocity.

2.3.1 Subboxes

At this point, all halos are identified but the amount of data to take into account to analyse them from the snapshot itself is quite vast. To lighten the necessary computational resources we have gathered all data around each halo. All information from particles around $\sim 2 - 3\, R_{\rm vir}$ is retrieved from the original simulation and saved into the halo file, we may coin as a *subbox*. The result is a subbox for every halo containing all particles plus a spare region of particles which may be of use for other studies in the future. In summary, a large fraction of particles that has no effect in the analysis of a particular halo is discarded, and the we have the original full snapshot is splitted into chunks surrounding the area we will focus in this thesis.

Note that this procedure not only speeds up the analysis due to the fact that positions of the considered particles are highly constrained towards the halo, but also allows to run any new computations on all halos without the full simulation. The drawback is the large amount of files generated. Fortunately, most of the halos found by the hierarchical FOFare unresolved and we will only create the subboxes for those halos with sufficient number of particles.

2.3.2 Halo counting

After running the FOF algorithm on MUC simulation, 975517 halos were identified at $z = 0$ with more than 50 particles. In order to speed up the analysis process we have created the subboxes for the 18193 biggest halos.

Notice that the more massive the halos the less important are non-gravitational physics to compute its global properties. Hence, we are choosing the clusters were the adiabatic regime is more dominant on the overall evolution of cluster dynamics. Besides, the number of subboxes built depends on resolutions and simulation due to the different cluster properties. For the other simulations: MUCL has 6109 subboxes while, MUW, MU2W and MUWHS ranges between ~ 3000 and 4300.

To do a preliminary analysis of substructure on MUC halos at $z = 0$ we used a modified version of the `AMIGA Halo Finder` Knollmann & Knebe (2009). This version is adapted to the binary format of subboxes and, thus, simplify any parallel implementation to a series of one-subbox runs in serial. The result allow us to classify every halo by dynamical state comparing the total masses of the main halo (M_1) and the biggest substructure with its $R_{\rm vir}(M_2)$:

Relaxed M_2 is smaller than 10% of M_1.

Minor merger M_2 is between 10% and 50% of M_1.

Major merger M_2 is bigger than 50% of M_1.

We find that 79.9% clusters are in relaxed state. Besides, 19.7% are experiencing a minor merger and only 0.4% are undergoing a major merger event. In figure 2.3 we show the amount of relaxed clusters at $z = 0$ distributed by total mass. Least massive object are $\sim 80\%$ in relaxed state, although there is a slight tendency to have more relaxation for $5 \times 10^{14} - 10^{15} h^{-1} M_\odot$. Bins with $M_{\rm vir} > 10^{15} h^{-1} M_\odot$ must not be considered because the number of clusters per bin is too small to be statistically significant.

Extending to higher redshifts, or even lower resolutions simulations, results into abnormal ratios of relaxed halos. Halos at increasing redshift are smaller and puffier than at $z = 0$ because during its formation they grow by merging and matter accretion. Furthermore, substructure finding intrinsically depends on the number of particles of these subclumps. Hence if the hosts are already smaller themselves, the underlying substructures are unresolved.

On the observational side, X-ray selected samples have confirmed that galaxy clusters are more disturbed at higher redshifts, i.e. Jeltema et al. (2005), Maughan et al. (2008a).

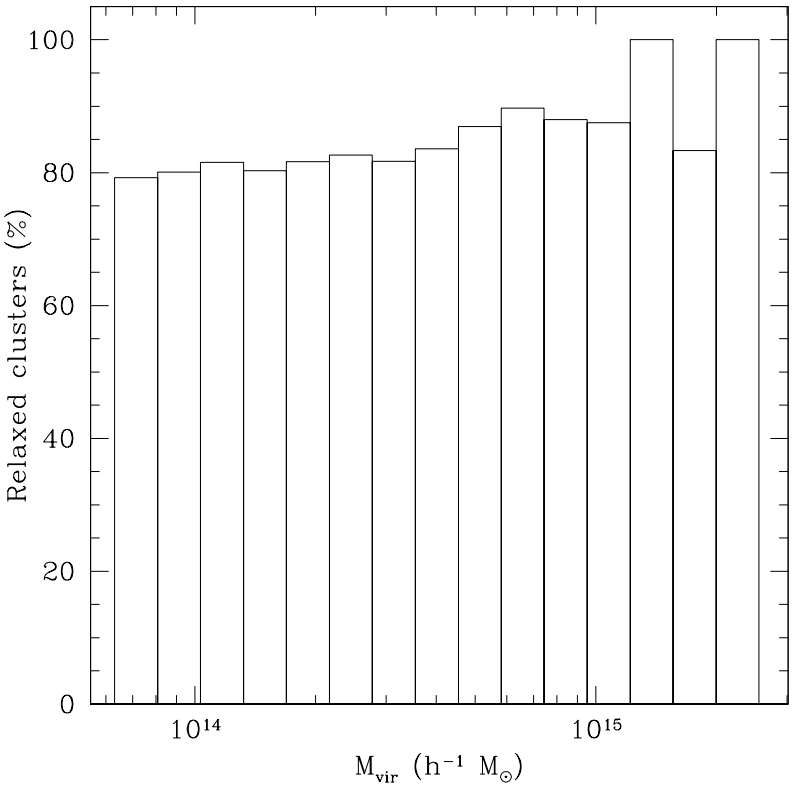

Figure 2.3: Percentage of relaxed clusters in MUC at $z = 0$ per $M_{\rm vir}$ bin.

2.4 Gas distribution

Observations indicate that most of the baryonic matter in the Universe does not reside in galaxies. At high redshifts, nucleosynthesis predicts deuterium abundances in agreement with the observed estimates through H I absorption lines in the spectra of distant quasars (Miralda-Escudé et al. 1996). In that age, the vast majority of baryons are located in photoionized intergalactic medium. Later on, when growth of structures begins, these clouds sparse or form the present structures such as galaxies, groups or clusters. Clearly, this evolutionary scheme changes the thermodynamical state of matter to the present values. In fact, recent estimates establish that at low redshifts $\sim 50\%$ of matter is not in intergalactic clouds, hot intracluster gas, stars or cold intergalactic matter. This is the so-called *missing baryon* problem which is still a hot topic on the scientific community (Nicastro et al. 2008).

As we described on section 1.2, hierarchical clustering is a highly non-

linear evolutionary process and the baryon content can only be studied through cosmological simulations. They predict that, as Universe evolves, baryons in the diffuse intergalactic medium accelerate towards the densest regions and get heated by shock waves. The amount of these clouds that do not lay inside the dense spots forms the filamentary structure of thin warm matter, the so-called warm-hot intergalactic medium (WHIM). Simulations not only serve as a tool to study collapsed objects such as clusters or galaxies, thanks to them we may also determine the overall distribution of gas in the Universe.

Baryons in the Universe can be listed in three broad phases depending on its temperature. The standard criterion is:

Hot ($T > 10^7 K$) Gas bounded to galaxy clusters and groups, forming the ICM.

Cold ($T < 10^5 K$) Photoionized intergalactic gas, stars and cool galactic gas.

Warm-hot ($10^5 K < T < 10^7 K$) WHIM in filaments making the cosmic web. Hardly observed yet.

Although the exact distribution of gas in theses phases is sensitive to details of the simulation, we can analyze them quantitatively by comparison with other works. In this thesis we have analyzed the distribution of those baryons for simulation MUC. Figure 2.4 shows the evolution of each phase at redshifts $z = 3, 2, 1.5, 1, 0.5$ and 0. It shows that WHIM fraction is 39% at the present epoch, in agreement with other predictions of $30\% - 40\%$ from numerical simulations reported in Davé et al. (2001) and Smith et al. (2010) and slightly smaller than other predictions such as Cen & Ostriker (1999) and Cen & Ostriker (2006) which claim half the baryons in the Universe are in warm-hot state.

The comparison of simulations with and without radiative cooling in Davé et al. (2001) shows that gravitational shock heating is the dominant heating mechanism for WHIM gas. This is an important point, as it suggests that radiative cooling has a secondary importance. We may expect from that cooling only affects WHIM at earlier times, when intergalactic gas is denser and, accordingly, can cool significantly. Davé et al. (2001) reports that after $z \sim 3$ the rate of growth of the WHIM fraction is kept constant no matter cooling and feedback are switched on in simulations, suggesting that WHIM is no longer affected by cooling. Notwithstanding, non-gravitational processes can efficiently suppress the X-ray emission outlining its importance in the chances of direct detection of gas filaments.

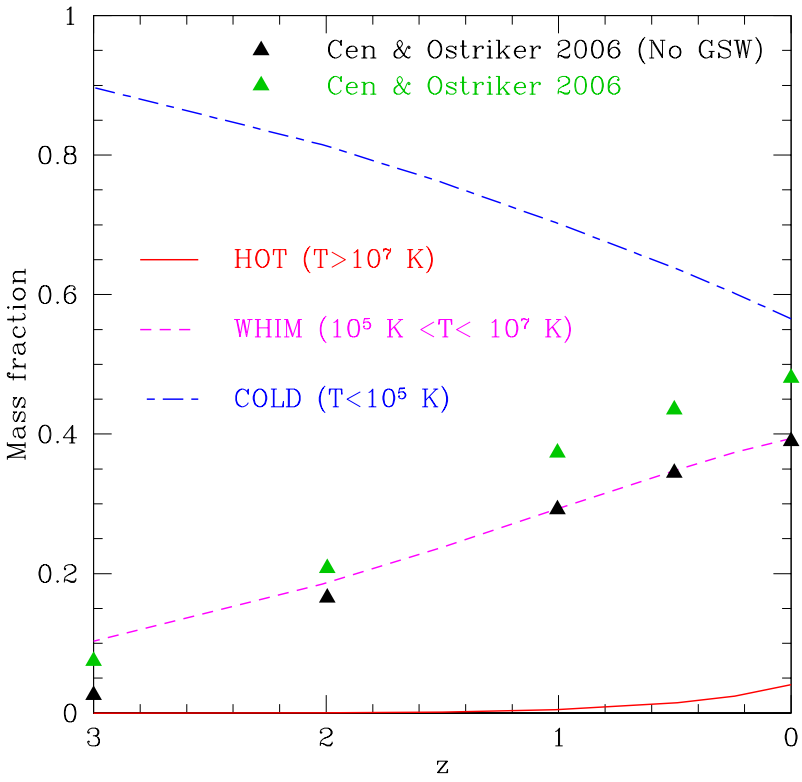

Figure 2.4: Abundance of baryons phases from $z = 3$. Evolution of hot, whim and cold baryons are represented in red, magenta and blue respectively. Results from Cen & Ostriker (2006) simulations are plotted on black and green triangles (see text).

On the other hand, the energy injection by feedback is the secondary responsible for heating the WHIM with no more than 20% the energy required as concluded in Cen & Ostriker (2006). However, the presence of galactic superwinds is needed in order to increase the WHIM fraction. Winds act as a mean of transportation for the energy emitted by feedback affecting larger regions. In figure 2.4 we compare the WHIM fraction from MUC with simulations including radiative cooling, feedback, non-instantaneous metal enrichment and, with and without winds (Cen & Ostriker 2006). The coincidence is remarkable from $z \lesssim 2$ proving that non-adiabatic physics plays a negligible role except for galactic winds. Eventually, the winds effect on WHIM fractions is an increase of $\sim 5 - 10\%$ at all redshift.

Chapter 3

X-ray properties and systematics

> Size matters not. Look at me. Judge me by my size, do you? Hmm? Hmm. And well you should not.
> For my ally is the Force, and a powerful ally it is. Life creates it, makes it grow. Its energy surrounds us and binds us.
> Luminous beings are we, not this crude matter. You must feel the Force around you; here, between you, me, the tree, the rock, everywhere, yes.
>
> *The Empire Strikes Back*, Master Yoda

For this thesis, we are mainly concerned with a few X-ray properties of clusters: temperature ($T_{\rm X}$), total mass ($M_{\rm tot}$), baryon content ($f_{\rm gas}$ or $M_{\rm gas}$), SZ proxy ($Y_{\rm X}$) and luminosity ($L_{\rm X}$). In this chapter we set the definitions of physical magnitudes used hereafter. In addition, the analysis performed on our simulated clusters is also explained.

3.1 Analysis overview

Once dark matter halos are identified by the FOF algorithm, we compute masses and other halo properties using both gas and dark matter present in the subbox for every cluster. Center of masses are computed by recursively computing from the initial FOF guess in a shrinking sphere up to few tens of

kpc to avoid spurious results from poor numerical data. The displacement between the initial dark matter center from FOF and the final center from the whole distribution happens to be negligible, unless the halo is fragmented in several pieces of comparable masses.

The extension of a cluster is somehow arbitrary because there is no sharp edge. Notwithstanding, current X-ray instruments are limited by their beam-size so cluster profiles are limited to density contrasts of 500 times the critical density in the cluster's rest-frame. In this work we have followed the standard convention of scaling cluster properties to $\Delta = 500$, although $\Delta = 200$ may be used in some particular analysis.

To have homogeneous properties with most works in the literature we choose an inner cut in the radial profile to exclude the central region which is strongly affected by radiative cooling. The inner cut is set to a fraction of the cluster radius as promoted by Kravtsov et al. (2006), $0.15\,R_{500}$, rather than a fixed radius. In summary all cluster properties reported in this thesis are integrated between $0.15\,R_{500} < r < R_{500}$, denoted as $\Delta = 500c$, to minimize scatter and make comparison with other simulations possible.

3.2 Cluster temperatures

Temperatures play an important role in cluster properties because it is directly measurable from X-ray spectra. However, the comparison between simulated and real data shows a mismatch between the spectroscopic temperature estimated from the observed spectrum and its simulated counterpart. Different proxies have been proposed to properly define temperature, most of them differ from each other in the weighting assigned to each gas element. In general, the ICM temperature can be written as

$$T = \frac{\sum w_i T_i}{\sum w_i}, \tag{3.1}$$

where T_i is the temperature of the i-gas element, which contributes with the weight w_i.

The easiest definition is the mass-weighted temperature (T_{mw}), computed using the mass particle as weight. Physically it matches with the electron temperature T_e for a fully ionized plasma. Notwithstanding, Mathiesen & Evrard (2001) found that T_{mw} is roughly $10 - 20\%$ higher than spectral fit

temperature in the CHANDRA bandpass.

To solve this large discrepancy, the emission-weighted (T_{ew}) was introduced as an observational-oriented proxy which is obtained by weighting with the particle emissivity, both including or excluding the cooling function (see section 3.3). The idea behind is to mimic the observational bias towards the luminous regions. Unlike T_{mw}, T_{ew} is more accurate to represent simple thermal structures but yet there is a tendency to derive higher temperatures when the thermal structure is more complex.

In the last years two more definitions have arisen to disentangle the still present mismatch between observations and simulations. Mazzotta et al. (2004) and Vikhlinin (2006) introduced the idea that the overall spectrum is a superposition of single-temperature spectra coming from a different thermal phase. In principle, a multi-plasma spectrum cannot be described by a single-temperature. However, in X-ray telescopes cooler phases are more relevant to provide the high energy cut-off of the spectrum given they work on finite energy bands. To account for this effect, Mazzotta et al. (2004) introduced the spectroscopic-like temperature (T_{sl}) by using $w_i = \rho_i \; m_i \; T_i^{-0.75}$ as weight for each SPH gas particle. With this expression, T_{sl} can reproduce observed temperatures for clusters with $T > 2 - 3 \; keV$.

Another approach is, as in Vikhlinin (2006), to develop a fitting expression that reproduce the temperature obtained from a spectroscopic fit. The key issue is separating the contribution from continuum and lines into two distinct temperatures and combine them according to their relative fluxes. Consequently, the obtained temperature (T_{spec}) is an accurate prediction for clusters with temperatures above $\sim 0.5 \; keV$ for arbitrary metallicity. In this work, we will make use of T_{spec} to compute cluster temperatures.

3.3 Cluster luminosities

The total ICM luminosity is obtained from the total emissivity by integrating over the plasma volume, which can be factorized in two parts. The first one depending on density and the other on temperature and metallicity, called *emission measure* (EM) and *cooling function* (Λ) respectively:

$$L_{\rm X} = \int_V \epsilon_{bol} \, dV = \Lambda(T, Z) \int_V n_e \, n_H \, dV, \tag{3.2}$$

where n_e and n_H are electron and hydrogen (whether ionized or not) number densities.

The EM is the responsible for the normalization of the spectrum. It is defined as $EM = \int n_e\, n_H\, dV$. On the contrary, the cooling function includes all the atomic physics and cooling properties of metals and molecules present balanced by their abundances. Hence, the spectrum's shape is determined by the plasma temperature and metallicity.

3.3.1 Metal cooling

Different metals have a distinct signature in cooling the plasma. Thus, the cooling function is strongly dependent upon the metallicity. Figure 3.1 illustrates the contribution of individual elements to the bolometric cooling function. It becomes clear how different temperature regimes are dominated by different coolants, in some cases the emissivity comes from a particular element. For instance, the $2 \times 10^5 K$ maximum due to the atomic transitions from Oxygen and Iron ions is the responsible for the bump at $\sim 10^6 K$. Notice that at high temperatures ($T > 10^8 K$) Hydrogen and Helium are guilty for the emission due to the bremsstrahlung free-free transitions; and so the slope is the predicted from thermal bremsstrahlung $\Lambda \propto T^{1/2}$. Furthermore, metals take the leading role in cooling the plasma when temperature drops below $10^6 K$.

In summary a number of spectral transitions are common in most X-ray spectra. In spite of the complexity described above, there are a couple of strong transitions that are used to determine most of the information in the spectrum. Several of those emission lines comes from C VI, N VII, O VII, O VIII, Ne IX, Ne X, S XXV, S XXVI and highly ionized Iron from Fe XVII to Fe XXVI. All the elements that have a major contribution in the emission for $T \lesssim 10^6 K$ are shown in fig. 3.1.

3.3.2 Cooling function models

The more widely used chemical abundances are the solar ones derived by Anders & Grevesse (1989) which differ significantly from more recent estimates (for example, Lodders (2003)), in particular for iron and oxygen which are eventually less abundant. Nevertheless, Anders & Grevesse (1989) abundances are still far more frequent in the literature and will be used throughout this thesis.

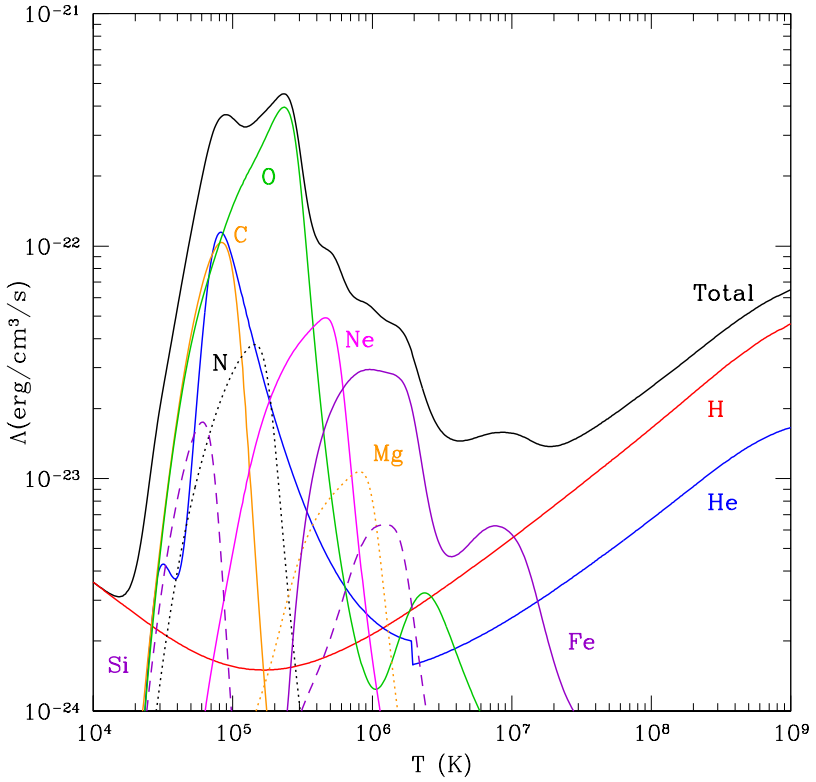

Figure 3.1: Bolometric cooling contribution for metals included in MEKAL plasma code. Metallicity is $0.3Z_{\odot}$ with a relative abundance of metals matching Anders & Grevesse (1989), in $0.01 - 100\,keV$ bandpass. Black line represent the total emissivity which has been used for the rest of this thesis.

There are a number of codes that calculate the X-ray spectrum using an extensive set of excitation and recombination rates. In general, the inputs are the thermal temperature, gas density, metal abundance and the energy range of interest. A set of cooling curves are given in the Sutherland-Dopita code (Sutherland & Dopita 1993), however these are useful only under CIE conditions. When the plasma can no longer be considered as optically-thin the photoionization processes become more important and corrections are needed.

Another widely used code is MEKAL (Mewe et al. (1985), Liedahl et al. (1995)) included in the spectral fitting package XSPEC. MEKAL evolved from the work started by Mewe in 1970, it is based on CIE models although has significantly grown and now includes non-equilibrium ionization modeling. MEKAL

models the effect of thousands of spectral lines from ions of H, He and 13 additional metals.

3.3.3 Computing luminosities

For the purpose of this thesis, we are only interested in applying the previous discussion to the practical computation of luminosities for lagrangian simulations. Since every gas particle in the simulation maps the surrounding region and the average density and temperature is given as an output the calculation of the emission measure and cooling function is much simpler than in observed clusters. Firstly, the EM becomes just a simple sum over all particles within the desired volume by computing the electron and hydrogen number densities as a function of densities, $n_e = \rho_{\rm gas}/(\mu_e\, m_e)$ and $n_H = \rho_{\rm gas}/(\mu\, m_H)$, being μ_e and μ the mean molecular weights of electron and particles.

$$EM = \frac{1}{(\mu_e\, m_e)(\mu\, m_H)} \sum_{i=1}^{N_{part}} \rho_{{\rm gas},i} m_i \tag{3.3}$$

Finally, the cooling function can be simply obtained from gas temperatures and metallicity. Because of the adiabatic nature of the simulations (section 2.2) there are no physical processes that may enrich the metal content of the ICM. This means that a given metallicity must be assumed. On average, the overall abundance of metals is about $0.3\, Z_\odot$ in clusters up to $z \sim 1$, as pointed out by Tozzi et al. (2003), which is the whole range of redshifts considered in this work.

For the temperature dependence, we have made use of the TCL script `ccreate_curve`[1] to construct cooling function out of the XSPEC package. This piece of software, developed by Dave Strickland under GNU license, runs from inside XSPEC. The script uses a pre-defined model (MEKAL with $Z = 0.3\, Z_\odot$ in this case) and builds up all spectral emissivities for a specified range of temperatures. The output is just the integration over frequencies of all these emissivities resulting in the cooling functions in $erg\ s^{-1}\ cm^{-3}$. Moreover, `ccreate_curve` comes with a set of shell scripts to handle the output for fully-customizable synthetic cooling functions. For instance, each metal contribution to the total emissivity shown on fig. 3.1 has been extracted using these additional scripts.

[1] This script can be downloaded from http://proteus.pha.jhu.edu/∼dks/Code/Coolcurve_create

In summary, we have build the cooling function at $z = 0$ for a $Z = 0.3\,Z_{\odot}$ with relative abundance of metals according to Anders & Grevesse (1989) using the MeKaL as a model for plasma emission. Unabsorbed rest-frame cluster luminosities are computed by interpolating the temperature on the generated look-up table to compute the cooling function, and normalizing by the emission measure (eq. 3.2).

All luminosities are *bolometric*, unless otherwise stated, which by definition in this thesis stands for the emission in the $0.01 - 100\ keV$ energy band. In X-ray astronomy it is common to use the range $0.01 - 10\ keV$ as bolometric measure, however we have decided to increase the upper threshold which extends the validity of the bremsstrahlung approximation to higher temperatures. Nonetheless, in the simulations described above not a single particle reach such high temperatures.

3.3.4 Sunyaev-Zel'dovich

As discussed on section 1.4.1, ICM is filled by high-speed electrons due to the almost fully ionized hot gas. Approximately 1% of the photons from the cosmic microwave background passing through a cluster experience inverse-Compton scattering producing a distortion in the nearly perfect blackbody spectrum. In this process, known as the Sunyaev-Zel'dovich (SZ) effect, Sunyaev & Zel'dovich (1972), energy is transferred from ICM electrons to CMB photons. As a result, the CMB spectrum is slightly distorted and shifted to larger frequencies (see Fig. 3.2) around $217\ GHz$ (Carlstrom et al. 2002). As a consequence, galaxy clusters can be seen as cold spots at low frequencies and as hot spots at high frequencies.

The most promising aspect of SZ observations is the absence of redshift dimming, which allows to identify clusters at almost any redshift. Since the effect measures the integral of the gas pressure and assuming that baryons and dark matter are in approximate hydrostatic equilibrium, SZ may provide a robust measure of clusters total mass almost independent of redshift. Although it is easy to understand this relation in general, details on the normalization and evolution are still needed. For future surveys, the redshift dependence of the SZ-mass relation and the mass function must be known with less than $\sim 5\%$ and $\sim 10\%$ uncertainty (Carlstrom et al. 2002).

The strength of the SZ decrement/increment is characterized by the Compton y-parameter which results from the line-of-sight integral of the thermal pressure,

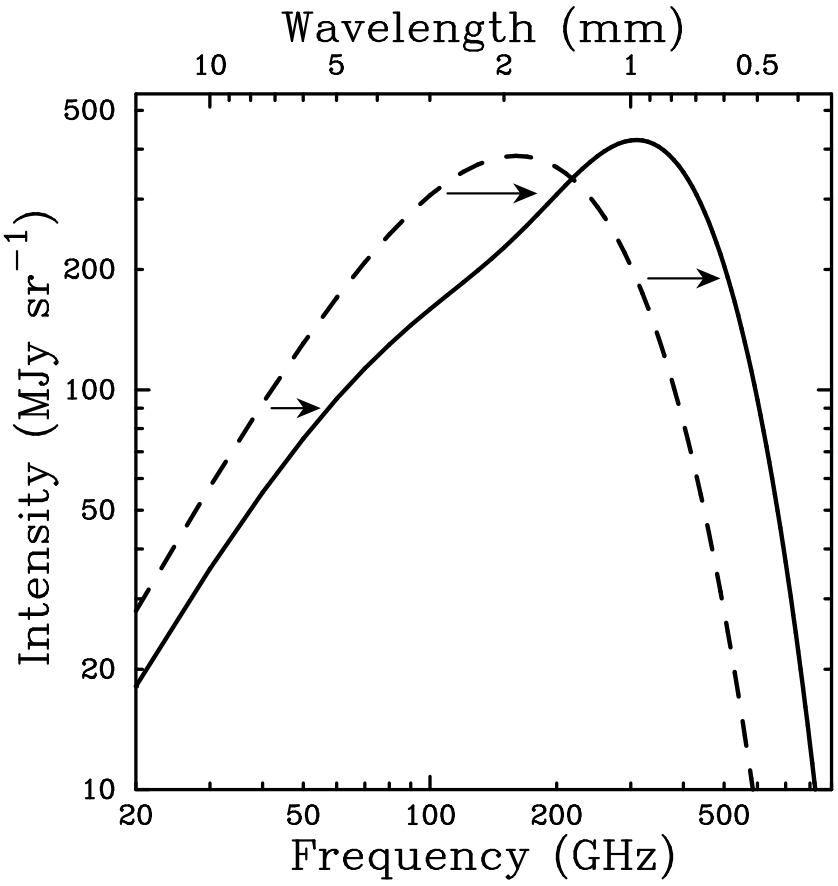

Figure 3.2: CMB spectrum, undistorted (dashed line) and distorted by Sunyaev-Zel'dovich effect (solid line). The distortion is produce for a fictional cluster 1000 times more massive than a typical cluster. Taken from Carlstrom et al. (2002)).

$$y \equiv \frac{k_B \sigma_T}{m_e c^2} \int T_e n_e dl, \tag{3.4}$$

where T_e and n_e are the temperature and electron number density respectively. σ_T is the Thomson cross-section, c the speed of light in vacuum and m_e is the electron rest mass. The temperature fluctuation of the CMB spectrum at a frequency ν is

$$\frac{\Delta T}{T_{CMB}} = y g(x), \tag{3.5}$$

where $g(x)$ is the frequency distribution of the thermal SZ effect, and depends on the dimensionless frequency $x = h\nu/k_B T_{CMB}$. From equation 3.5, the strength of the thermal SZ effect is on y-parameter while $g(x)$ represents the qualitative distortion on the spectrum shown on fig. 3.2. In the Rayleigh-Jeans limit ($\nu \ll 200\, GHz$), this simplifies to $\Delta T/T_{CMB} \simeq -2y$. A relativistic correction can sometimes be included on the value of $g(x)$ as in Itoh & Nozawa (2004), but the net correction is smaller than 1% for clusters with $T < 10keV$.

We also define the integrated comptonization parameter Y as the integral over a solid angle,

$$Y = \int y d\Omega = \frac{1}{d_A^2(z)} \Big(\frac{k_B \sigma_T}{m_e c^2} \Big) \int_V n_e T_e dV, \tag{3.6}$$

being d_A the angular distance, $d\Omega = dA/d_A^2$ is the solid angle and dV the cluster volume.

Since Y is a function of angular distance in this work we will consider the intrinsic thermal SZ signal, defined as (see Nagai (2006)),

$$Y_{\rm X} \equiv Y d_A^2(z) \propto f_{\rm gas} M_{\rm tot} T_m, \tag{3.7}$$

where T_m is the gas mass-weighted temperature and $f_{\rm gas}$ is the baryon to total mass ratio of gas that contributes to the SZ.

Expressed in this way, $Y_{\rm X}$ is an unbiased estimator of the integrated Compton y-parameter (Bonamente et al. 2008) which can be inferred from the X-ray properties of observationally and theoretically. Besides, recent works (Kravtsov et al. (2006), Nagai (2006), Hallman et al. (2007)) indicate that it is a low-scatter proxy for the cluster total mass and correlates strongly with other X-ray properties (Maughan 2007).

In this thesis we have decided to compute X-rat temperatures as the product of gas mass and T_{spec}, for similarity with observational analysis, in order to reduce possible systematics. In any case, when the cluster core is excised the spectral temperature is closer to the T_{mw} which ideally should be used in equation 3.7.

3.4 Resolution in Scaling Relations

It was shown in chapter 2 that the simulations used in this thesis have different mass resolutions. Since we will investigate on the implications of cosmological parameter variation further on this thesis, we must first assess the spurious numerical results due to unresolved cluster structure.

We will only focus on how different mass resolution may alter cluster properties for a single cosmological model by making use of halos simulated with different, but still constant, particle masses. In summary, we will employ clusters in simulations MUC, MUCL and a re-simulation subsample of some of these clusters. Incidentally, we will contrast the local scaling laws in these two resolutions at different overdensity and we will compare with the results of observations and other simulations from the literature.

It is important to note that the scope of this chapter is not a formal discussion on convergence and discreetness since we lack the appropriate simulations, as described at Binney (2004). Nevertheless, there are a number of papers discussing this issue on the literature. Above all, we stand out Power et al. (2003) which establishes the optimal parameters to assess effective convergence on mass profiles using N-body codes.

3.4.1 Local scaling relations

Here we examine the differences on scaling relations $z = 0$ clusters at for $\Delta = 500c$ in MUC and MUCL simulations. We begin constructing a volume-limited sample of clusters at $z = 0$. We choose a mass threshold for this sample that avoid resolution effects for unresolved small clusters while maximize the mass range and sample size. The mass threshold is selected from the MUCL mass functions which shows a flattening in the low-mass end due to the limited subbox extraction. For masses below $M_{\rm tot}$ $3 \times 10^{13} h^{-1} M_{\odot}$ the volume sample is incomplete and those clusters are discarded.

The internal structure of halos can also be affected by limited resolution. Poorly resolved halos tend to be more diffuse and their shallower potential leads to a more extended gas distribution. Besides, clusters have smoother density fields because the substructure of smaller objects is not resolved.

In table 3.4.1 we report the scaling laws obtained by fitting our clusters, according to the following relations:

Relation (Y-X)	Simulation	State	α	β
$M_{\rm tot} - T_{\rm X}{}^{\dagger}$	MUC	All	14.480 ± 0.009	1.86 ± 0.03
	MUC	Relaxed	14.472 ± 0.007	1.88 ± 0.02
	MUCL	All	14.345 ± 0.009	1.77 ± 0.04
	MUCL	Relaxed	14.33 ± 0.01	1.75 ± 0.05
$M_{\rm tot} - Y_{\rm X}$	MUC	All	5.27 ± 0.08	0.654 ± 0.006
	MUC	Relaxed	5.21 ± 0.06	0.658 ± 0.004
	MUCL	All	5.4 ± 0.1	0.640 ± 0.008
	MUCL	Relaxed	5.4 ± 0.1	0.639 ± 0.009
$L_{\rm X} - T_{\rm X}{}^{\dagger}$	MUC	All	44.77 ± 0.01	2.09 ± 0.03
	MUC	Relaxed	44.76 ± 0.01	2.10 ± 0.04
	MUCL	All	44.650 ± 0.008	2.05 ± 0.03
	MUCL	Relaxed	44.64 ± 0.01	2.03 ± 0.05
$f_{\rm gas} - M_{\rm tot}$	MUC	All	0.11 ± 0.01	-0.0100 ± 0.0007
	MUC	Relaxed	0.13 ± 0.01	-0.0113 ± 0.0009
	MUCL	All	-0.15 ± 0.04	0.009 ± 0.003
	MUCL	Relaxed	-0.16 ± 0.05	0.009 ± 0.003

† Temperatures are measured in units of 3 keV.

Table 3.1: Local scaling relations in simulations MUC and MUCL at $\Delta = 500c$. Parameters shown correspond to the best fit of $\log Y = \alpha + \beta \log X$. Relaxed only and all halos fit was done independently to compare possible dynamical state bias. Errors in the parameters are 1σ.

$$\begin{aligned}
M_{\rm tot} - T_{\rm X}: &\quad \log\left(\tfrac{M_{\rm tot}}{h^{-1}M_{\odot}}\right) &=& \alpha_{MT} + \beta_{MT}\, \log\left(\tfrac{T_{\rm X}}{3\,keV}\right) \\
M_{\rm tot} - Y_{\rm X}: &\quad \log\left(\tfrac{M_{\rm tot}}{h^{-1}M_{\odot}}\right) &=& \alpha_{MY} + \beta_{MY}\, \log\left(\tfrac{Y_{\rm X}}{M_{\odot}keV}\right) \\
L_{\rm X} - T_{\rm X}: &\quad \log\left(\tfrac{L_{\rm X}}{h^{-2}\,erg/s}\right) &=& \alpha_{LT} + \beta_{LT}\, \log\left(\tfrac{T_{\rm X}}{3\,keV}\right) \\
f_{\rm gas} - M_{\rm tot}: &\quad \log\left(\tfrac{f_{\rm gas}}{\Omega_{\rm bar}/\Omega_{\rm m}}\right) &=& \alpha_{fM} + \beta_{fM}\, \log\left(\tfrac{M_{\rm tot}}{h^{-1}M_{\odot}}\right)
\end{aligned} \tag{3.8}$$

Given that most of the clusters are less massive, a direct least-square fit would produced biased results towards the small objects. To avoid this, we decided to bin the data into 7 bins evenly spaced in mass. In each bin we compute the mean and standard deviation of $M_{\rm tot}$, $Y_{\rm X}$, $L_{\rm X}$, $T_{\rm X}$ and $f_{\rm gas}$. And finally, the mean values are fitted using a least-square fit weighted by the stan-

dard deviations. An additional advantage of this procedure is that a measure of the intrinsic scatter is taken into account, which we will use in following chapters.

We begin by comparing the scaling laws in two different subgroups, on the one hand the sample of all clusters regardless their dynamical state, and on the other only relaxed clusters are considered. All relations result to be compatible within 1σ, proving that dynamical state does not have a significant effect on this relations. The inclusion of radiative cooling, star formation and thermal feedback does not alter this results, as it has been reported by Jeltema et al. (2008) using simulations performed by the `ENZO` code. Besides, according to Yang et al. (2009) and Balogh et al. (2006), dynamical state is not a significant source of intrinsic scatter on $M_{\rm tot} - T_{\rm X}$ or $L_{\rm X} - T_{\rm X}$ either, since the net effect of merging is changing $L_{\rm X}$, $M_{\rm tot}$ and $T_{\rm X}$ in such a way that clusters move along the scaling relations.

Seeing that relaxation state should not be a complication for the rest of the thesis and the fact that lower σ_8 simulations may have poorer number of clusters to work with, we have chosen skip to dynamical states differentiation for the next chapters. In addition, the limitations in observed clusters not always allow to determine the relaxation state so, for the sake of similitude, we follow that same approach.

The best-fit slopes deviates from the self-similar prediction even in the absence of non-gravitational physics. In Ascasibar et al. (2006) we show that non-gravitational clusters are well-fit by a polytropic model in hydrostatic equilibrium with the host dark matter halo. The structure of the ICM is eventually determined by the concentration parameter. The effects of polytropic index and concentration tend to cancel each other, leading to scaling relations close to the self-similar model.

$M_{\rm tot} - T_{\rm X}$ relation

The $M_{\rm tot} - T_{\rm X}$ relation is of fundamental importance since theory is expressed in terms of mass, not temperature. The mass can be estimated in several ways but there are inherent unknowns associated with each one. The classic technique to estimate cluster masses is from observations of the radial velocity of its member galaxies. In X-rays, the cluster mass estimates come the relations between cluster mass and the indicators $T_{\rm X}$, $Y_{\rm X}$ and M_{gas} Vikhlinin et al. (2009).

In figure 3.3 we compare $M_{\rm tot} - T_{\rm X}$ on WMAP1 at three different resolu-

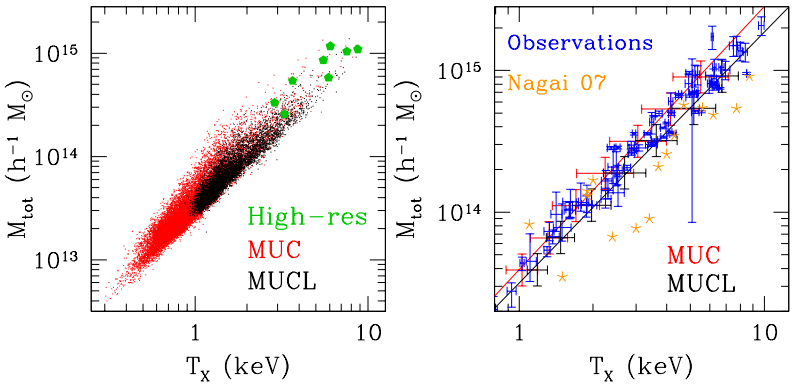

Figure 3.3: Mass vs Temperature relation for MUC and MUCL at $z = 0$. *Left:* All halos at 2048^3, 1024^3 and 512^3 effective resolution in green, red and black respectively. *Right:* Binning and comparison of the best-fit local $M_{\rm tot} - T_{\rm X}$ scaling relation for low and medium resolution. On blue, observed clusters from Vikhlinin et al. (2006), Vikhlinin et al. (2009) and Mantz et al. (2009). Orange stars represents simulated clusters from Nagai et al. (2007b).

tions. On the top we show selected re-simulated clusters at $\Delta = 500c$, MUC and MUCL, 2048^3, 1024^3 and 512^3 effective resolution, respectively. We do not see a significant deviation on this relation, although clusters in MUCL are less scattered. The tight correlation between MUC and the re-simulated clusters indicates that the $M_{\rm tot} - T_{\rm X}$ relation converges at 1024^3 resolution. Our measurement at 512^3 has a $\sim 0.14\,dex$ lower normalization that, despite being inconsistent with the 1024^3 value, visually appears to lay within scatter. On the bottom, the best-fit $M_{\rm tot} - T_{\rm X}$ for MUC and MUCL are plotted together with the clusters reported in Nagai et al. (2007b) and a compilation of observations.

The blue error bars represent high-quality observations compiled from the literature, see chapter 6. It is important to note that our results for WMAP1 agree well within the current observational uncertainties.

$M_{\rm tot} - Y_{\rm X}$ relation

The most robust X-ray mass estimator is the quantity $Y_{\rm X}$ recently proposed by Kravtsov et al. (2006). $Y_{\rm X}$ is a proxy of the total thermal energy of the ICM and also the integrated low-frequency SZ flux. Hydrodynamic simulations of Kravtsov et al. (2006) indicate that the $M_{\rm tot} - Y_{\rm X}$ relation shows less scatter for $M_{\rm tot}$ for a fixed $Y_{\rm X}$. Furthermore, it appears not to be very sensitive to

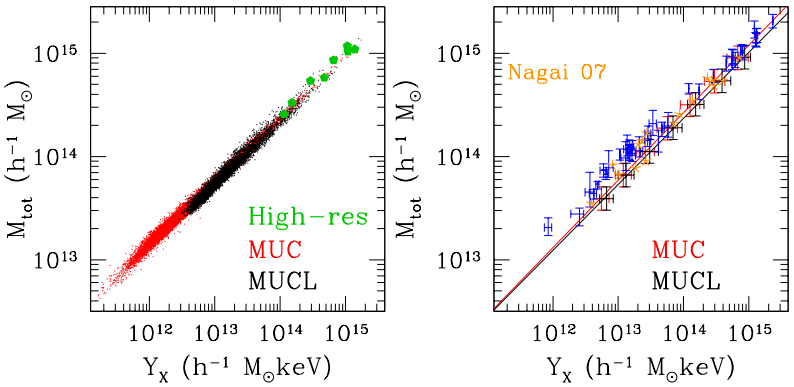

Figure 3.4: Same as fig. 3.3 for the $M_{\rm tot} - Y_{\rm X}$ relation.

gas cooling, star formation and feedback (Nagai 2006) which makes adiabatic simulations like our a very good tool to study it.

Figure 3.4 plots the $M_{\rm tot} - Y_{\rm X}$ relations for the samples in MUC and MUCL, as in the previous relation. Although we get similar results as in $M_{\rm tot} - T_{\rm X}$, $M_{\rm tot} - Y_{\rm X}$ is a more tight relation which apparently has less scatter even at 512^3 resolution. As stated by Nagai (2006), adding radiative processes during cluster formation as it is the case for Nagai et al. (2007b) simulations (plotted as orange asterisk) has little importance in the $M_{\rm tot} - Y_{\rm X}$, at least at $z = 0$.

Besides, we find no traces of poorly resolved halos which indicates that this relation is very robust not only with dynamical states and radiative gas processes. In table 3.4.1, $M_{\rm tot} - Y_{\rm X}$ relations between MUC and MUCL are compatible within 1σ whether in $M_{\rm tot} - T_{\rm X}$ have a larger distortion. According to this, $M_{\rm tot} - Y_{\rm X}$ is also less dependent on the resolution and requires less resolution to get convergent results.

$L_{\rm X} - T_{\rm X}$ relation

Historically, $L_{\rm X} - T_{\rm X}$ is the most studied relation in X-ray properties of galaxy clusters for two main reasons, clusters are selected by flux and because it involves the two direct observables X-ray properties. It is also the first observational evidence against the self-similar model. The dependence of luminosity and gas density, $L_{\rm X} \propto n_H^2$ (Greene 1959), leads to unrealistic determination X-ray luminosities in adiabatic simulations.

However, we have decided to include the $L_{\rm X} - T_{\rm X}$ relation in our analysis

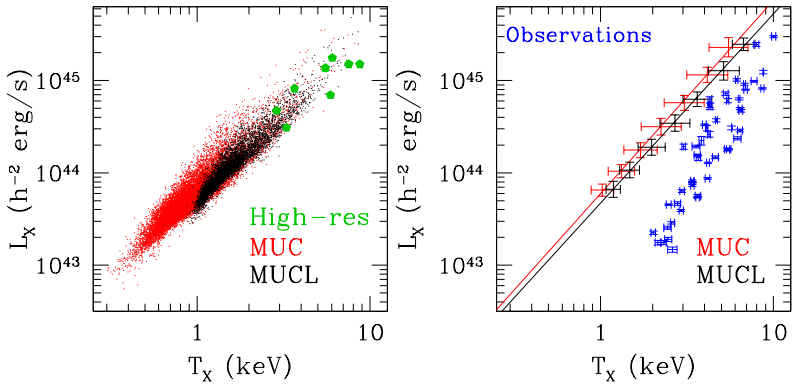

Figure 3.5: Same as fig. 3.3 for the $L_X - T_X$ relation.

although radiative cooling takes its importance mainly in the central region or clusters, where gas is very compressed. When the inner cores are excluded from the computation, the leading role into an accurate reproduction of the ICM state turns to resolution.

Despite the common belief that adiabatic clusters must follow exactly the self-similar expectation, we find significant steeper slopes than $\beta_{LT} = 2$. As shown by Ascasibar et al. (2006) that deviation is a consequence of the different shapes of the gas and dark matter density profiles which produce nearly, but not precisely self-similar luminosities. In fact, that deviation is more stresses more in luminosities than in the others X-ray indicators. From our simulations we can assess how the $L_X - T_X$ changes when the resolution is too low and the shape of the density profiles are not accurately sampled.

In figure 3.5 we compare the $L_X - T_X$ of clusters in MUC and MUCL. On the one hand, the coldest clusters happen to be clearly underesolved which appears as a distinct steepness for $T_X \lesssim 1.5\,keV$ clusters. This steepness must not be mixed with the observed for galaxy groups (Rosati et al. 2002) since it is purely due a spurious numerical result. It is also the responsible for the differences reported in β_{LT} in table 3.4.1 between MUC and MUCL.

On the other hand, we cannot appreciate any significant deviation with resolution in the high-temperature end. Consequently, we may establish that convergence is found but only when clusters with sufficiently large number of particles are taken into account. A more strict constraint must be set in order to a deeper analysis of the $L_X - T_X$ relation, in particular for studies at large radius.

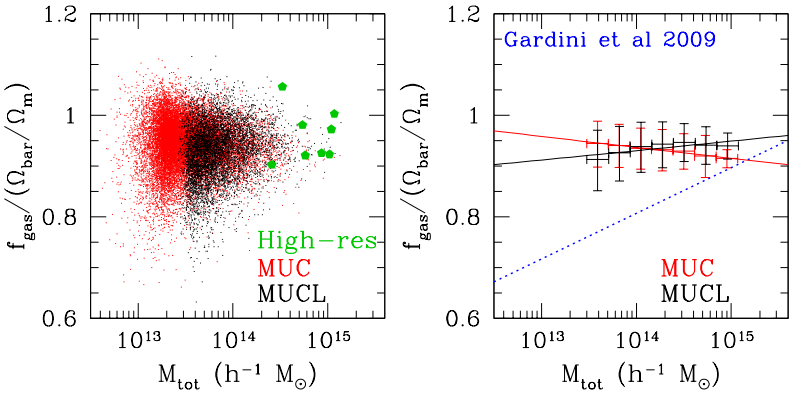

Figure 3.6: Same as fig. 3.3 for the $f_{\rm gas} - M_{\rm tot}$ relation.

Regarding the scatter, we expect that convergence in resolution for scatter is more restrictive than convergence in the best-fit relations according to $M_{\rm tot} - T_{\rm X}$ and $M_{\rm tot} - Y_{\rm X}$. For the luminosities, MUC shows a larger intrinsic scatter that MUC. In both simulations the low-T regime are narrower than their counterparts at the same resolution, indicating that small number of particles within halos leads to a biased low-scatter estimation.

$f_{\rm gas} - M_{\rm tot}$ relation

The observed cluster baryon fraction is an important tool for the determination of cosmological parameters. The usage of non-radiative simulations to determine baryon fractions is definitively a simplification. Kravtsov et al. (2005) studied the effects of cooling and star formation on the baryon fraction in clusters. They show that cooling drags the gas towards the central galaxy during the cluster formation increasing the $f_{\rm gas}$ even at radii as large as the virial radius. As a consequence, the $f_{\rm gas} - M_{\rm tot}$ relation is very sensitive to the internal structure of halos.

In figure 3.6 we show the $f_{\rm gas} - M_{\rm tot}$ relation for our set of clusters. For resolutions 512^3 and 1024^3 we get a scattered cloud around the cosmic fraction, however, we find a significant trend for low-mass cluster in both simulations. MUCL clusters show a dramatic decrease of $f_{\rm gas}$ at $M_{\rm tot} \lesssim 10^{14} h^{-1} M_\odot$ for this reason which, same as in $L_{\rm X} - T_{\rm X}$ relation, resulting into a positive slope.

We find the same baryon fraction decrease in the analysis of the Millennium Run simulation (Crain et al. 2007) and the simulations introduced by Rudd

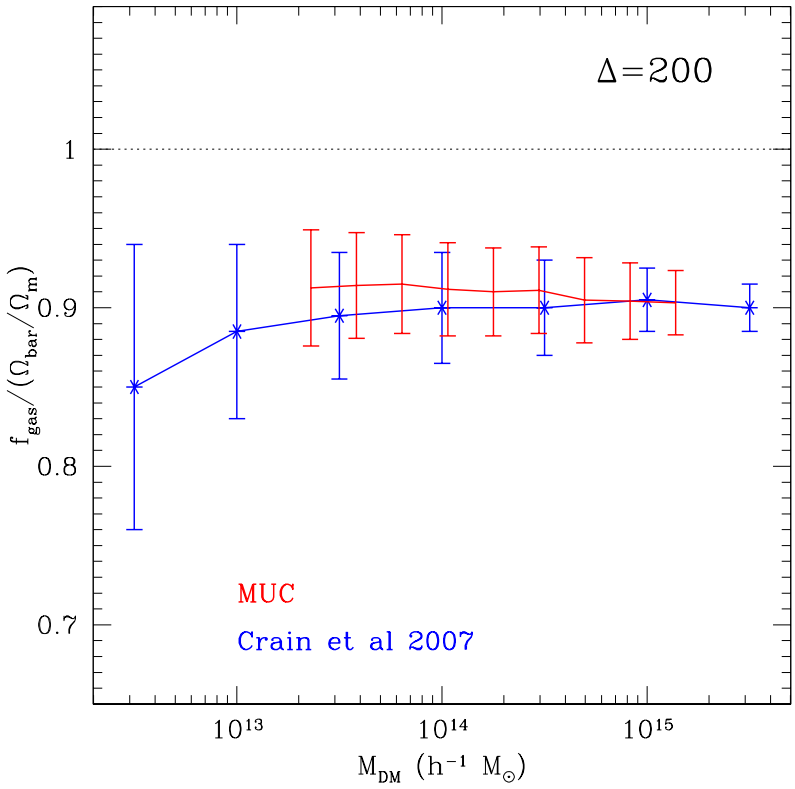

Figure 3.7: Comparison of $f_{\rm gas} - M_{\rm dm}$ for simulations MUC and Millennium Run at $\Delta = 200$. Mass binning has been adapted to match data from Crain et al. (2007).

(2007) performed by ART. The binning and overdensity of MUC clusters have been resized to match their data in figure 3.7. Crain et al. (2007) argue that the downturn is observed for clusters with fewer than ~ 500 particles in two of their simulations. By looking at figure 2 from Crain et al. (2007), we notice that the trend begins at $N_{dm} \sim 2000$ particles ($M_{200} \simeq 3 \times 10^{13} h^{-1} M_\odot$) if we are less conservative than in their simulation HIGH-MASS. MUCL clusters exhibit the same decrease at $N \sim 1500$ particles ($M_{\rm tot} \simeq 10^{14} h^{-1} M_\odot$) in figure 3.6, which seems to be a rough limit to get convergence of results in baryon fraction. Conversely, MUC does not show such decrease for the whole range where our data sample is complete.

At $\Delta = 500c$ MUC, which is not affected by spurious low $f_{\rm gas}$, exhibits negative slope and values below the cosmic mean. We believe that is a relic of the cluster formation, initially having a homogeneous $f_{\rm gas}$ but during the

collapse of the cluster region, dark matter falls faster than gas. This scheme leads to $f_{\rm gas}$ lower than the cosmic value. Furthermore, massive clusters have smaller baryon fraction because the highest density peaks begin to grow first.

Rudd (2007) reports a disagreement between ART simulations and Gottlöber & Yepes (2007) results from MUC at the virial radius. We also find such disagreement in normalization at $\Delta = 500c$. While we obtain mean values of 0.92, Rudd (2007) report a mean $f_{\rm gas}$ of $0.95 - 0.96$ for $M_{\rm tot} > 3 \times 10^{13} h^{-1} M_{\odot}$. This offset is consistent with the known $3\% - 10\%$ systematic difference between SPH and PM-bashed codes for adiabatic simulations (Frenk et al. (1999), Kravtsov et al. (2005)).

3.4.2 Side-effects in temperature

A one-to-one comparison between massive clusters of MUC and MUCL shows discrepancies in cluster properties. Whereas total and gas masses show negligible differences ($\lesssim 3\%$) at 512^3 and 1024^3 resolution, temperatures exhibit systematic larger variations. Contrary to the expectations, massive clusters at low-resolution are up to $2\,keV$ ($\sim 15\%$) hotter than their equivalents at high resolution. This could come from a lower concentration parameter c in lower resolution.

As we mentioned earlier, lower resolution makes shallower gravitational potential and more extended halos. In other words, the density profile of such clusters are less concentrated. As a consequence, the gas distributions spread out in a larger region so that temperature increases by hydrostatic equilibrium.

In order to check for plausible explanation for this deviation, we make use of the toy model developed by Ascasibar et al. (2006). It shows that the structure of the ICM in their non-radiative simulations are well fit by a polytropic model, $P \propto \rho_{\rm gas}^{\gamma}$, in hydrostatic equilibrium with the host halo, where γ is correlated with the halo concentration c.

Ascasibar et al. (2006) also provides with phenomenological formulae to estimate integrated X-ray properties from γ and c at a given overdensity. For the mass-weighted temperature it is (see their equation 11)

$$T_{mw} = T_0 \, \frac{y\,(\frac{\gamma}{\gamma-1}, c_{\Delta})}{\frac{1}{\gamma-1}, c_{\Delta}}, \tag{3.9}$$

where T_0 is the central temperature and the function y is defined as $y(\eta, c) \equiv$

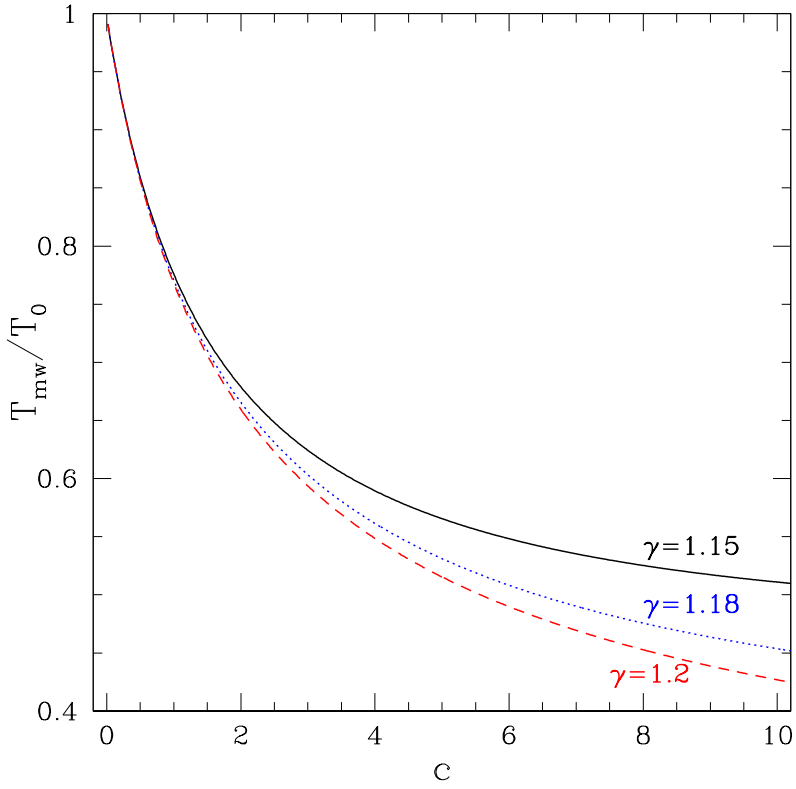

Figure 3.8: Mass-weighted temperature variation with concentration according to the analytical model described in Ascasibar et al. (2006).

$\int_0^c \left[\frac{\ln(1+x)}{x}\right]^\eta x^2 dx$.

Considering the ICM is well described by a polytropic equation of state of index $\gamma \simeq 1.18$ as reported in Ascasibar et al. (2003), we have plot equation 3.9 as a function of concentration for a representative range of polytropic indexes in figure 3.8. This figure proves that the sparser the halo, the more sensitive to temperature variations is.

Typically, clusters of $10^{15}h^{-1}M_\odot$ presents concentrations of $c_{500c} \sim 2-5$ as derived from figure 18 of Vikhlinin et al. (2006). Assuming a polytropic cluster with $\gamma = 1.18$, the model of Ascasibar et al. (2006) predicts temperatures ranging from $T_{mw}^{c=2}/T_0 = 0.665$ to $T_{mw}^{c=5}/T_0 = 0.531$, a 13.4% difference very similar to the $\sim 15\%$ we get from MUC and MUCL clusters. This indicates that the differences in $M_{\rm tot} - T_{\rm X}$ between our simulations are of the same order than typical variations in real clusters.

Chapter 4

Scatter of Scaling Relations

> In any case, were I to invoke logic, logic clearly dictates that the needs of the many outweigh the needs of the few.
>
> *Star Trek II: The Wrath of Khan*, Mr. Spock

So far, we have stated that X-ray properties are eventually related by a set of simple scaling relations. In practice, the internal structure of clusters is so complex that all scaling laws have an intrinsic scatter which is still not well understood. The main sources of scatter are the different environments where clusters are formed, their substructures (Schuecker et al. 2001) and the influence of their cores (O'Hara et al. 2006). Both environment and substructure are purely due to gravitational processes, whereas the core is dominated by radiative cooling and heating from galaxies. We devote this chapter to quantify such intrinsic scatter.

Getting to know the intrinsic scatter is important in two aspects. From the point of view of cosmology, the intrinsic scatter is a measure of the accuracy in the determination of mass functions and baryon fractions (e.g. Voit (2005b), Ettori et al. (2009)). The accuracy of the mass measurements are eventually related to the determination of cosmological parameters.

For astrophysical studies, the intrinsic scatter is closely related to the formation histories of galaxy clusters. Studying the sources of the scatter will help us understand all the physical processes involved and its relative importance at different cosmic times.

Given the adiabatic nature of our simulations, we can only focus on the contribution of mergers and substructure disregarding the net effect of cluster cores in the intrinsic scatter. However, the large amount of clusters simulated and the high resolution to resolve the substructure allow us to accurately assess the contribution of gravitational heating to the intrinsic scatter. To this end we have computed the X-ray properties of our samples of clusters at $\Delta = 500c$, where the cluster cores are subtracted inside $r < 0.15\, r_{500}$ to effectively remove the bias produced by including cores which are not well physically modeled.

In the previous chapter we already stated that the $f_{\rm gas} - M_{\rm tot}$ relation determines a minimum mass below which, galaxy clusters are unresolved. Here, we have removed those objects from the following analysis by selecting mass-complete samples on datasets. For simulation MUC we have only considered clusters with $M_{\rm tot} > 4{\times}10^{13}\, h^{-1} M_{\odot}$ while for MUCL, MUW+MU2W and MUWHS the two lees massive bins have been removed by setting the threshold at $M_{\rm tot} > 9 \times 10^{13}\, h^{-1} M_{\odot}$.

All scaling laws considered are fitted, as in section 3.4, by means of evenly-spaced mass bins to avoid bias towards low-mass clusters[1]. The scaling relations considered are described in equations 3.4.1.

Given that our datasets comes from simulation with two different resolutions, we can study the influence of cosmology and numerical resolution. In this chapter we chose MUCL as the basis for comparative purposes. The combination of simulations MUCL, MUW, MU2W and MUWHS sweep WMAP cosmological frameworks with a common 512^3 resolution. With them we make a comprehensive study of the intrinsic scatter as a function of cosmology. On the other hand, MUC and MUCL differ only in numerical resolution, making the comparison of them a proxy of the systematics in the intrinsic scatter due to numerical resolution.

Notwithstanding, resolution effects are still present given that less-massive clusters contain lower number of particles than high-mass ones. This could translate into systematic differences between resolutions that, in principle, are less important than systematic variation from simulation-to-simulation.

[1] A comprehensive description of Malmquist and Eddington biases can be found in the appendix of Mantz et al. (2009)

Intrinsic scatter

Nowadays, numerical codes and computer resources allow scientists to perform simulations of large patches of the Universe with enough number of galaxy clusters to account not only for the scaling relations, but also for the scatter of such scaling laws. Besides, the number of observed galaxy clusters has equally increased with the advent of X-ray observatories in space.

The measure scatter in the scaling relations lead to a better understanding of the cluster formation. Moreover, it is necessary to determine the uncertainty of X-ray properties when they are calculated via the scaling relations. To illustrate this we will take the estimation of cluster masses. Vikhlinin et al. (2009) estimate two different masses for each cluster from the observed $T_{\rm X}$ and $Y_{\rm X}$ by employing normalized $M_{500} - T_{\rm X}$ and $M_{500} - Y_{\rm X}$. Hence, the uncertainties of cluster masses are ultimately determined by the width of each scaling relation at a fixed temperature and SZ proxy.

The intrinsic scatter quantifies the dispersion between two X-ray properties. There are a wide variety of methods used in the literature, although all are meant to be the same, i.e. the measure of the scaling relation's width for a whole sample of objects. Consequently, once the mean scaling relation is fit (equations 3.4.1) we proceed to compute the intrinsic scatter.

In the literature the scatter is usually defined as (see Morandi et al. (2007))

$$S = \left[\sum_j (\log Y_j - \alpha - \beta \log X_j)^2/(N-2)\right]^{1/2} \tag{4.1}$$

where α and β are the scaling relation's slope and normalization, X_j and Y_j are the cluster X-ray properties considered and N is the number of data. In other words, clusters are assumed to follow a Gaussian distribution in (X,Y) whose dispersion is described by the variance of the sample. The assumption of normal variance of X-ray properties is a common element of the likelyhood analysis used in cluster cosmology studies, i. e. Rykoff et al. (2008). Ventimiglia et al. (2008), Stanek et al. (2006), Morandi et al. (2007), Vikhlinin et al. (2009) to name some, follow this definition for a number of simulated and observed clusters.

In our work, the outstanding number of simulated objects allow us to extend that work not only to the computation of such variance. Moreover, we will fully describe the whole distribution of clusters with respect to the scaling relations. Besides, skewness and kurtosis will also be computed in order to

check against the gaussianity hypothesis which is one of the foundations for the estimates in future experiments in cluster cosmology (e.g., Lima & Hu (2005), Rykoff et al. (2008)).

We begin by measuring the residuals of the clusters to the best-fit scaling law.

$$Res_j = \log Y_j - \alpha - \beta \log X_j. \tag{4.2}$$

Then, we construct a histogram of residuals of the dependent variable $\log Y$. At this point, the residuals distribution in our working space ($\log X$, $\log Y$) should be a normal distribution characterized by a mean and standard deviation. The latter is the measure of dispersion and, by definition in this work, will be called the *intrinsic scatter* of property $\log Y$ and is denoted as $\sigma_{\log Y}$ hereafter. Finally, it is important to note that $\sigma_{\log Y}$ and equation 4.1 are the same only if clusters are accurately described by a Gaussian.

Nonetheless, we eventually check for the similitude to a Gaussian distribution by computing the skewness and kurtosis of residuals histogram. To compute kurtosis we use the *excess kurtosis* with respect to a normal distribution defined as

$$\gamma_2 = \frac{\Sigma(x_i - \bar{x})^4}{(n-1)\,\sigma^4} - 3 \tag{4.3}$$

A positive γ_2 indicates a `peaked` distribution whereas a negative γ_2 indicates a `flat` distribution. A Gaussian distribution has zero excess kurtosis by construction.

Equally important is the skewness that we have estimated by using a cumulative expansion. Given that a gaussian distribution has a skewness of zero, the skewness of a datasets indicates whether deviations from the mean are going to be positive or negative. The skewness parameter is defined as

$$\alpha_{skew} = \frac{6\,(\bar{x} - x_{median})}{\sigma}\,\left(1 + \frac{\gamma_2}{8}\right) \tag{4.4}$$

A positive α_{skew} means that the right tail is longer or the most frequent values of the distribution are concentrated towards lower values. Conversely, a negative value for α_{skew} shows a concentration towards the higher values.

Lastly, we want to point out that in the considered scaling relations it is unclear which variable should be considered as (in)dependent. For this reason, we decided to compute the intrinsic scatter for each X-ray property at each scaling relation. Hence, the above procedure is performed in the vertical and horizontal directions of $M_{\rm tot} - T_{\rm X}$, $M_{\rm tot} - Y_{\rm X}$ and $L_{\rm X} - T_{\rm X}$.

Scatter residuals

A more accurate description of the scatter can be obtained only when the statistics of galaxy clusters is very large. Thanks to the huge number of clusters in our simulations we can determine the scatter as a function of the fixed variable for the first time. For instance, Ventimiglia et al. (2008) analyse the impact of low-mass clusters in the overall scatter.

To this end we compute the deviation in log space $\sigma_{\log Y|X}$ from the mean $\log Y$ at a fixed value of $\log X$. In other words, we provide residual functions that model the intrinsic scatter at fixed $\log X$. In our case we can compute the residuals of $M_{\rm tot} - T_{\rm X}$ independently at different temperatures ($\sigma_{\log M_{\rm tot}|T_{\rm X}}$), providing with the function $\sigma_{\log M_{\rm tot}|T_{\rm X}}$ versus $T_{\rm X}$.

For a better understanding the procedure is explained in section 4.1, taking the $M_{\rm tot} - T_{\rm X}$ relation as an example.

4.1 $M_{\rm tot} - T_{\rm X}$ relation

The $M_{\rm tot} - T_{\rm X}$ relation has historically played an important role in estimating cluster masses from X-ray observations. Recently, cosmological simulations have tested that $M_{\rm tot} - T_{\rm X}$ is one of the best proxies to estimate cluster masses from direct X-ray observables.

Although $M_{\rm tot}$ can be estimated from the cluster surface brightness assuming hydrostatic equilibrium, in the practice there are systematics uncertainties from non-thermal pressures components (Nagai et al. 2007b) involved in the computation of $M_{\rm tot}$. According to Vikhlinin et al. (2009) the best way to accurately determine $M_{\rm tot}$ is to use corrections suggested by simulations. Besides, simulating large number of clusters allow us to assess the intrinsic scatter which is one of the most important source of uncertainty in the $M_{\rm tot}$ estimation.

Intrinsic scatter

To compute the intrinsic scatter we proceed to apply the observational prescription, beginning by computing the scaling relations of all datasets. Table 4.1 report the results along with the minimum mass threshold considered and the Pearson product-moment correlation coefficient which account for the degree of linear dependency between $M_{\rm tot}$ and $T_{\rm X}$. All datasets show a Pearson's correlation coefficient better than 0.996, establishing a very strong linear dependency.

In figure 4.1 we show the intrinsic scatter for simulation MUC as an example. The reader is referred to figures B.1, B.2 and B.3 on appendix B for similar plots from cluster samples of MUCL, MUW+MU2W and MUWHS.

All clusters considered for the $M_{\rm tot} - T_{\rm X}$ fitting are plotted as black dots in the main panel. All bins and the resulting scaling law are overplotted in red[2]. The top panel shows the histogram of logarithmic distances between MUC clusters $M_{\rm tot}$ and the masses derived from $M_{\rm tot} - T_{\rm X}$ at fixed temperature. Accordingly, the right panel shows a similar histogram for the temperatures differences at fixed cluster mass using the analogous $T_{\rm X} - M_{\rm tot}$ relation. Both histogram are overplotted in blue representing the best-fit gaussians in order to get $\sigma_{\log {\rm M}}$ and $\sigma_{\log {\rm T_X}}$.

The result of applying the same procedure to all MARENOSTRUM simulations is summarized in table 4.2. It shows the parameters which characterize

[2]Green lines are explained at the end of the current chapter.

$M_{\rm tot} - T_{\rm X}^{\dagger}$

Simulation	Minimum Mass	Norm	Slope	Correlation
MUC	$4 \times 10^{13} h^{-1} M_{\odot}$	14.480 ± 0.007	1.85 ± 0.03	0.9995
MUCL	$9 \times 10^{13} h^{-1} M_{\odot}$	14.357 ± 0.007	1.70 ± 0.03	0.9993
MUW+MU2W	$9 \times 10^{13} h^{-1} M_{\odot}$	14.35 ± 0.01	1.55 ± 0.08	0.9964
MUWHS	$9 \times 10^{13} h^{-1} M_{\odot}$	14.38 ± 0.01	1.60 ± 0.06	0.9979

† Temperatures are measured in units of 3 keV

Table 4.1: Best-fit for $M_{\rm tot} - T_{\rm X}$ at $\Delta = 500c$. Slopes and normalizations are reported at 1σ accuracy. Last column reports the Pearson's correlation coefficients of binned data.

the intrinsic scatter, skewness and kurtosis of all histogram analysis.

We begin the discussion by looking at the intrinsic scatter. As a baseline value we have chosen MUCL simulation because it is the only one which shares the same resolution with MUW+MU2W and MUWHS and the same cosmological framework with MUC, for resolution comparison.

A direct correlation between $\sigma_{\log \rm M}$, $\sigma_{\log \rm T_X}$ and the normalization of the initial power spectrum for the lower resolution simulations is found. For WMAP3 $\sigma_{\log \rm M}$ is being reduced by $0.27dex$ with respect to MUCL, while for a WMAP5-like cosmology we find that $\sigma_{\log \rm M}$ is closer decreasing just $0.14dex$, lying in between the WMAP1 and WMAP3 results.

The analysis on the temperature scatter results into the same behavior but showing smaller differences. From the higher to lower σ_8 values, we get $0.10dex$ and $0.06dex$ decrement in $\sigma_{\log \rm T_X}$ for MUW+MU2W and MUWHS, respectively. This results demonstrates, that cosmological model parameter plays a major role in determining the scatter of scaling relations.

To account for the effects of resolution we proceed to compare MUC and MUCL cluster samples. In chapter 3 we already mentioned that, visually, the MUC dataset could present a larger scatter than its lower resolution counterpart. Indeed, the results on table 4.2 indicates $0.22dex$ and $0.06dex$ increments in $\sigma_{\log \rm M}$ and $\sigma_{\log \rm T_X}$, respectively, when resolution is enhanced in MUC.

The question that still remains is, how much would galaxy formation modify the adiabatic intrinsic scatter? To answer it we may take the results of

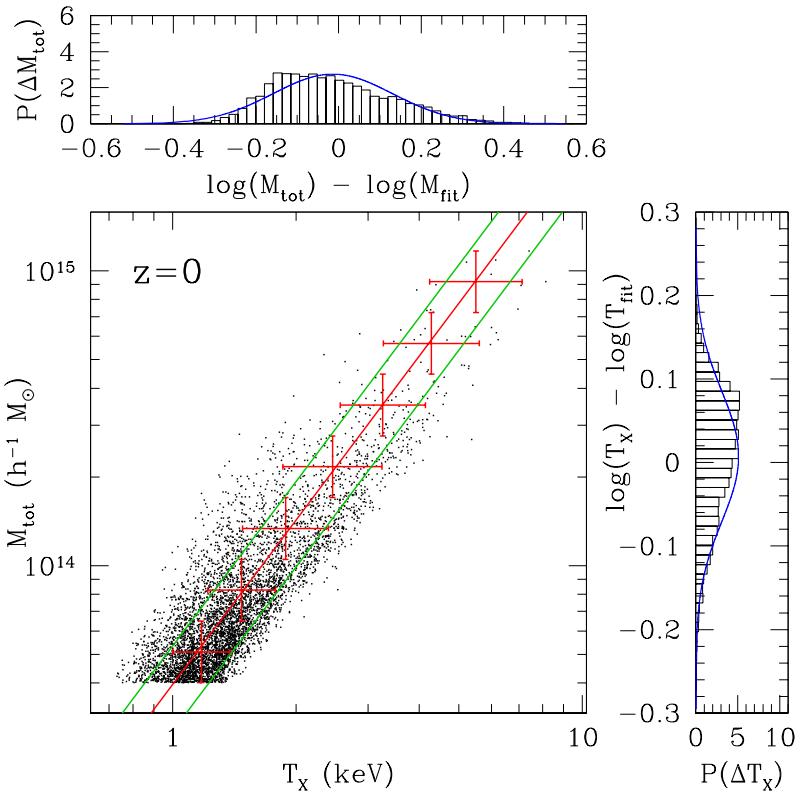

Figure 4.1: Intrinsic scatter for the $M_{\rm tot} - T_{\rm X}$ relation in simulation MUC at $z = 0$ and $\Delta = 500c$. *Top:* Histogram of logarithmic differences between cluster $M_{\rm tot}$ and best-fit relation. *Right:* Histogram of logarithmic differences between cluster $T_{\rm X}$ and best-fit relation. *Bottom:* Halos (black dots) and $2\sigma_{\log {\rm M}}$ scatter (green surface).

Nagai et al. (2007a) which uses the code ART to simulate 16 high resolution galaxy clusters in WMAP1. They present measurements of the scaling relations and scatter in the simulations with cooling. In that study the X-ray observables are derived from mock CHANDRA analysis.

Nagai et al. (2007a) report a scatter of 0.136 for their sample with radiative cooling, star formation, metal enrichment and stellar feedback. That result is just slightly smaller than our $\sigma_{\log {\rm M}}$ for MUC reported on table 4.1, even though their measurements include the cluster cores and they have a higher spatial resolution. We believe that the additional source of scatter due to non-radiative physics is overcompensated by the removal of substructure by using mock CHANDRA X-ray images. Examination of the data used in Nagai et al.

$M_{\rm tot} - T_{\rm X}^{\dagger}$

Simulation	Scatter		Skewness		Kurtosis	
	$\sigma_{\log \rm M}$	$\sigma_{\log \rm T_X}$	$\alpha_{\rm logM}$	$\alpha_{\rm logT_X}$	$\gamma_{\rm logM}$	$\gamma_{\rm logT_X}$
MUC	$0.145\,(0.22dex)$	$0.078\,(0.06dex)$	0.084	-0.083	-0.082	-0.084
MUCL	0.123	0.072	0.081	-0.082	-0.285	-0.286
MUW+MU2W	$0.096\,(-0.27dex)$	$0.062\,(-0.10dex)$	0.084	-0.077	0.070	0.063
MUWHS	$0.109\,(-0.14dex)$	$0.068\,(-0.06dex)$	0.088	-0.086	-0.179	-0.183

† Temperatures measured in units of 3 keV

Table 4.2: Best fit and intrinsic scatter for $M_{\rm tot} - T_{\rm X}$ at $\Delta = 500c$. On parenthesis the increment with respect to MUCL simulations results.

(2007a) indicates that the systematics in the estimation of $M_{\rm tot}$ in real clusters exhibit a scatter decrease, $0.019dex$, of the same order that our mismatch between 1024^3 and 512^3 resolutions.

Unfortunately, we cannot compare the scatter directly to observations because for real clusters, the scatter is dominated by measurements uncertainties and intrinsic scatter altogether.

Finally, we check the assumption of gaussianity in $M_{\rm tot} - T_{\rm X}$ by discussing the skewness and kurtosis of the mass and temperature histograms. The difference between the listed values and zero is a measure of the overall deformation from gaussian in the frequency distribution. While deviations from gaussianity are present in all measures, common features are still present. All histograms show equal deviations in skewness, positive $\alpha_{\rm logM}$ and negative $\alpha_{\rm logT_X}$. Close inspection at histograms in figures 4.1, B.1, B.2 and B.3 reveal and excess of clusters towards lower masses and higher temperatures than the means.

As shown in Stanek et al. (2010), from the analysis of the MGS simulation, such a deviation in skewness is expected for simulated clusters with similar resolution than our MUC. Briefly, Stanek et al. (2010) conclude that their two datasets present negative skewness in the temperature distribution, from one simulation including preheating and cooling and another gravitation-only.

In contrast, kurtosis show larger deviations between simulations. MUC and MUW+MU2W are slightly off gaussianity whereas MUCL and MUWHS are lower kurtosis. Put it in another way, larger γ_2 values indicates that the

distributions are more peaked. Visual inspection seems to indicate that the variations reported in table 4.2 are not significant.

Summarizing, although the clusters histogram may not deviates from the assumed gaussianity, it is still a fairly good estimator at large distances from the mean values. We find a good agreement at the wings of the gaussians, beyond $\sim 2\sigma$, which indicates that the region $\pm 2\sigma$ contains approximately 95% of all clusters. In other words, a gaussian is a good approximation of scatter for $logM_{\rm tot} - logT_{\rm X}$ when a sufficiently large number of clusters are taken into account so that we have a good sampling in the outer regions.

Coming back to figure 4.1, the green lines in the main panel delimit the 2σ confidence region computed from the $M_{\rm tot}$-histogram. In other words, the region where 95% of the clusters lie.

Scatter residuals

So far we have only considered the intrinsic scatter of the $M_{\rm tot} - T_{\rm X}$ relation for the full sample of clusters. Now, we are interested in which clusters have a larger contribution to that scatter. In the following we restrict our analysis to the $T_{\rm X}$-dependence since it is the observable property from where $M_{\rm tot}$ is derived. The reverse process ($M_{\rm tot} \rightarrow T_{\rm X}$), although possible, it is of no practical use from the point of view of observations.

Firstly, the residuals of all clusters are computed as $\log M_{\rm tot} - \log M_{fit}$, being M_{fit} the total mass predicted by the scaling relation for a cluster with temperature $T_{\rm X}$ equal to the cluster temperature.

Then we have binned in temperature by using 20 uniform logarithmic bins. An illustration of this step for simulation MUC is represented in the top panel of figure 4.2, which shows the number counts of cluster per $T_{\rm X}$-bin. Further simulations can be found in section C.1 at appendix C.

Finally, the standard deviation of residuals is computed in each bin, noted as $\sigma_{\log M_{\rm tot}|T_{\rm X}}$. In our example at figure 4.2 this is plotted as a red line in the bottom panel. Clearly we notice two different regimes, at low temperature where $\sigma_{\log M_{\rm tot}|T_{\rm X}}$ decreases until completeness, then it remains fairly linear up to the highest temperatures where some noise is found due to low number of massive clusters. This limitation is eventually driven by the simulation boxsize.

As in the intrinsic scatter, high and low-$T_{\rm X}$ behavior must be treated carefully to alleviate biases. We can naturally avoid them by disregarding all bins

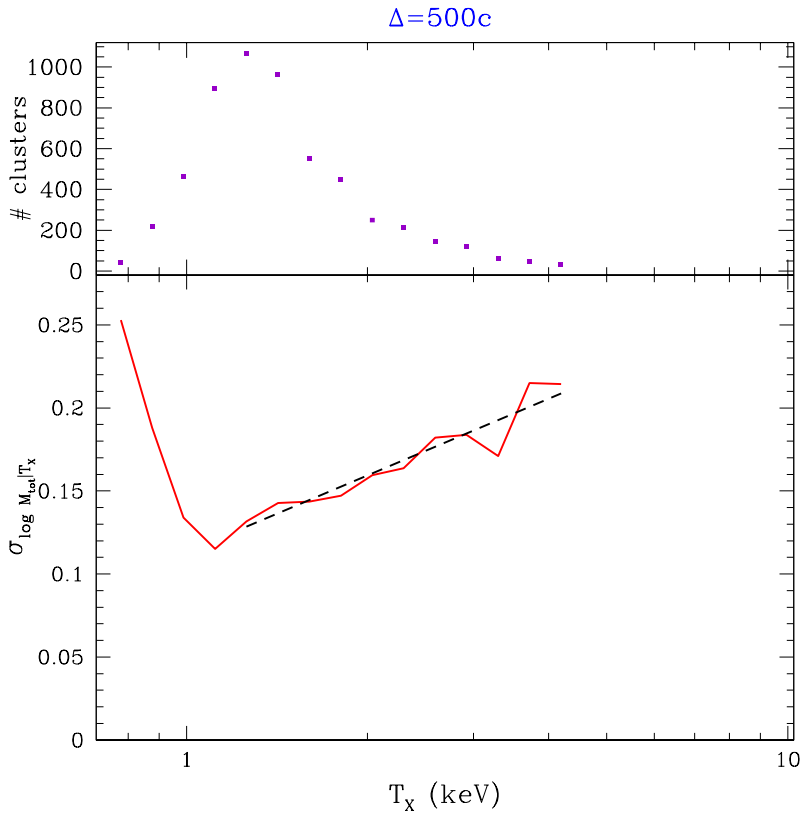

Figure 4.2: Temperature and mass scatter residuals in the $M_{\rm tot} - T_{\rm X}$ relation for MUC at $z = 0$ and $\Delta = 500c$. *Top:* Histogram of number counts of clusters per temperature bin. Bins with less than 30 clusters have been removed. *Bottom:* Solid line represent standard variance of residuals. Dotted line show the best-fit residual function in the temperature range (see text and table 4.3).

at high temperature which has less than 30 clusters because the statistical sample is too low to account for any dispersion. In the low-temperature end, we remove all bins in the region where the sample is not complete. In figure 4.2 that maximum is found at $T_{\rm X} < 1.25\,keV$. Those remaining bins are fitted to a power-law, represented by a black dashed-line in fig 4.2.

Summarizing, we obtain a residual function whose validity is restrained to a range of temperatures. In table 4.3 these functions are reported for all datasets considered, along with the valid range of temperatures.

We begin the discussion by examining the effect of resolution in the scatter residuals. The clearest manifestation is found when the high and low resolution

Simulation	Residual function	Range
MUC	$\sigma_{\log M_{\rm tot}\|T_{\rm X}} = (0.15 \pm 0.02)\ (T_{\rm X}/3\,keV) + (0.186 \pm 0.003)$	$1.26 < T_{\rm X} < 4.20$
MUCL	$\sigma_{\log M_{\rm tot}\|T_{\rm X}} = (0.13 \pm 0.03)\ (T_{\rm X}/3\,keV) + (0.115 \pm 0.003)$	$2.15 < T_{\rm X} < 4.19$
MUW+MU2W	$\sigma_{\log M_{\rm tot}\|T_{\rm X}} = (0.25 \pm 0.02)\ (T_{\rm X}/3\,keV) + (0.111 \pm 0.002)$	$2.34 < T_{\rm X} < 3.02$
MUWHS	$\sigma_{\log M_{\rm tot}\|T_{\rm X}} = (0.29 \pm 0.03)\ (T_{\rm X}/3\,keV) + (0.119 \pm 0.003)$	$2.11 < T_{\rm X} < 2.99$

Table 4.3: Scatter dependence on mass and temperature for all simulations at $\Delta = 500c$. Best-fit values are rounded to the last significant figure. High temperature bins with less than 30 halos have been excluded to fit the scatter, see text for the full procedure explanation.

simulations of WMAP1 are compared. MUC and MUCL exhibit slopes which are consistent within the uncertainties. In both simulations we find increasing residuals with temperature, which indicates that high-$T_{\rm X}$ clusters contribute more to the intrinsic scatter regardless the resolution. The fact that $\sigma_{\log M_{\rm tot}|T_{\rm X}}$ slopes are consistent eventually means that resolution affects systematically to all clusters regardless of their mass.

Normalization, conversely, indicates a large trend between 1024^3 and 512^3 resolution. Obviously, the larger normalization found in the residuals is the responsible for the overall larger intrinsic scatter reported in table 4.2 for simulation MUC.

Finally, the range of temperatures where our $\sigma_{\log M_{\rm tot}|T_{\rm X}}$ is valid remain very similar in the two simulations. The maximum $T_{\rm X}$ is determined by the initial normalization of the power spectrum which ultimately dictates the abundance of massive clusters[3]. The different spatial resolution in MUC and MUCL does not alter the amount of clusters, only the sampling of the radial profile.

The minimum temperature limitation, on the contrary, is set by the completeness of the datasets. At lower resolution smaller halos are more diffuse, so that they are more difficult to be detected by the FOF algorithm. Thus, MUC is a complete down to smaller $T_{\rm X}$ values.

So far we have only looked at WMAP1 simulations to examine their residuals. The next stage is to consider the MUCL, MUW+MU2W and MUWHS datasets which match in resolution. This will allow us to examine the impact of different cosmological frameworks on the scatter.

[3]This will be reviewed in chapter 5 devoted to galaxy clusters abundances.

We find significant differences among the three cosmological models. Contrary to effect of resolution, slopes exhibit larger discrepancies than normalizations when cosmology changes.

MUW+MU2W and MUWHS, which only differ in the initial normalization of the power spectrum, present consistent slopes within 1σ. The larger σ_8 value for MUWHS makes more massive clusters to have a larger deviations from the mean $M_{\rm tot}-T_{\rm X}$ law, although this effect is minimal. In contrast, WMAP1 shows a slope roughly a factor 2 smaller than MUW+MU2W and MUWHS, having a more constant intrinsic scatter at all temperatures.

Normalizations, on the other hand, do not change much with cosmological models. Variations in normalizations between MUC, MUW+MU2W and MUWHS are ~ 0.004, same order of their individual uncertainties.

Lastly, the validity range in temperature for functions $\sigma_{\log\, M_{\rm tot}|T_{\rm X}}$ is clearly larger for WMAP1. This is a consequence of having a larger initial normalization of the power spectrum with respect to the other datasets. We would expect that MUWHS will also have a larger maximum temperature because its σ_8 is larger than WMAP3. However, the volume considered in the MUW+MU2W dataset is doubled than the MUWHS standalone sample precisely to increase the number of massive clusters. A detailed analysis of the number count of clusters for each simulation is discussed on chapter 5.

4.2 $M_{\rm tot} - Y_{\rm X}$ relation

We have already stated that the scatter of scaling relations is a limiting factor in the accurate determination of masses from galaxy cluster observables properties. In essence it is a source of systematic uncertainty when total masses are to be estimated from cluster temperatures. With the development of new instruments and the construction of X-ray observatories outside the atmosphere, an increasing large number of galaxy clusters are being observed, and even more will be available at higher redshifts in the near future. For this reason, intrinsic scatter takes now a fundamental role and low scatter scaling relations need to be developed.

The SZ effect has turned up to be one of the main observational properties to take into account in order to study high redshift galaxy clusters thanks to its property of being almost redshift independent. However, the SZ signal of the ICM lays at sub-mm frequencies which would require observations in both X-ray and radiowaves.

Nevertheless, the insights driven by the Sunyaev-Zel'dovich effect can still be useful on the X-ray regime. The quantity $Y_{\rm X}$, introduced by Kravtsov et al. (2006), is an analogy to the total integrated SZ flux of a galaxy cluster but measured from X-ray observable properties. Computed as the simple product of cluster gas mass and the temperature, it is proportional to the pressure in the ICM. Moreover, it relates two directly observable properties.

The important features for us are the facts that $M_{\rm tot} - Y_{\rm X}$ shows lower scatter than $M_{\rm tot} - T_{\rm X}$ and it seems not to be very sensitive to gas cooling, star formation and energy feedback (Nagai 2006). It is then assumed that $Y_{\rm X}$ can be an excellent proxy for the cluster total mass from observational measurements.

Consequently, our sample of clusters match perfectly with the requirements for a in-depth scatter analysis on $M_{\rm tot} - Y_{\rm X}$. This section is devoted to such analysis and a comparison with the previous results from the $M_{\rm tot} - T_{\rm X}$ scaling relation.

Intrinsic scatter

We begin by computing the intrinsic scatter as it was described at the beginning of the current chapter. Results from the best-fit scaling relations are reported in table 4.4 including the minimum mass threshold considered in

$M_{\rm tot} - Y_{\rm X}$

Simulation	Minimum Mass	Norm	Slope	Correlation
MUC	$4 \times 10^{13} h^{-1} M_{\odot}$	5.23 ± 0.05	0.657 ± 0.003	0.9999
MUCL	$9 \times 10^{13} h^{-1} M_{\odot}$	5.6 ± 0.1	0.624 ± 0.008	0.9997
MUW+MU2W	$9 \times 10^{13} h^{-1} M_{\odot}$	6.2 ± 0.3	0.58 ± 0.02	0.9985
MUWHS	$9 \times 10^{13} h^{-1} M_{\odot}$	6.0 ± 0.1	0.599 ± 0.008	0.9997

Table 4.4: Best-fit for $M_{\rm tot} - Y_{\rm X}$ at $\Delta = 500c$. Slopes and normalizations are rounded matching the error accuracy. Last column reports the Pearson's correlation coefficients of binned data.

each dataset and the correlation coefficients of the data bins.

For all our datasets the correlation between $M_{\rm tot}$ and $Y_{\rm X}$ is better than 0.998, underlying the assumption of a robust linear dependency between mass and the SZ-proxy. Furthermore, each simulation exhibits even a better correlation for $M_{\rm tot} - Y_{\rm X}$ than the measured on table 4.1 for the $M_{\rm tot} - T_{\rm X}$ scaling relation. In particular, simulation MUC has the best correlation of all which turns into smaller uncertainties in the scaling parameters.

Once the mean scaling relation is found we proceed to compute the intrinsic scatter. As an illustration, figure 4.3 shows the results for our highest resolution dataset. Clearly MUC evidence of a lower scatter when $Y_{\rm X}$ is employed to scale masses rather than temperatures. Similar plots for simulations MUCL, MUW+MU2W and MUWHS are drawn in appendix C; respectively, figures B.4, B.5 and B.6.

The discussion begins by visually comparing the distributions of figures 4.1 and 4.3. The reason is that they represent two scaling relations of the same cluster sample. Apparently, the shape of the histograms is similar in both analysis and yet, the assumption of gaussianity is not fully accomplished for the $M_{\rm tot} - Y_{\rm X}$ histograms either. However, most of the clusters lay near the peaked region of the Gaussian ($\lesssim 2\sigma$).

The results in tables 4.2 and 4.5 indicate that MUC has an intrinsic scatter in mass, $\sigma_{\log \rm M}$, approximately a factor 2.5 smaller than in the $M_{\rm tot} - T_{\rm X}$ relation, whereas $\sigma_{\log \rm T_X}$ and $\sigma_{\log \rm Y_X}$ remain almost unchanged. Put it in another way, for a galaxy cluster whose $Y_{\rm X}$ has been determined observationally, the estimated $M_{\rm tot}$ would have a uncertainty of roughly 2.5 times smaller than if

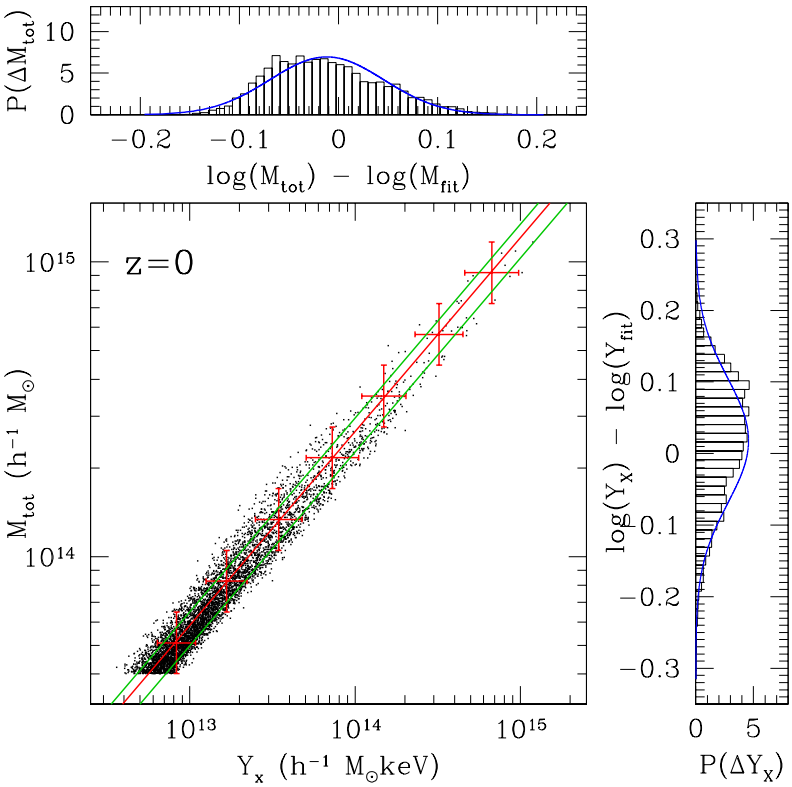

Figure 4.3: Same as figure 4.1 for $M_{\rm tot} - Y_{\rm X}$ relation.

X-ray temperature is directly used to estimate the total mass.

Kravtsov et al. (2006) and Nagai et al. (2007a) report mass scatters of $\sigma_{\log \rm M} \simeq 0.05 - 0.07$ using Mock CHANDRA images of clusters simulated with star formation and thermal feedback in a WMAP1 model. Besides, Kravtsov et al. (2006) claim that the anti-correlation of residuals for gas mass and temperature is the reason why the behavior of $Y_{\rm X}$, on average, has smaller scatter. The results for that cosmology in our work indicate compatible $\sigma_{\log \rm M}$ between Kravtsov et al. (2006) and MUC and MUCL.

Moreover, the temperature and gas mass variations due to resolution described in section 3.4.2 lead to scatter variations of $\sigma_{\log \rm M} \sim 0.004$ in our $M_{\rm tot} - Y_{\rm X}$ relations, which are eventually much lower that the uncertainty produced by non-gravitational process during the cluster formation.

Finally, we focus on the cosmological dependence by looking at simulations MUCL, MUW+MU2W and MUWHS. WMAP3 and WMAP5-like cosmolo-

$M_{\rm tot} - Y_{\rm X}$

Simulation	Scatter		Skewness		Kurtosis	
	$\sigma_{\log \rm M}$	$\sigma_{\log \rm Y_X}$	$\alpha_{\rm logM}$	$\alpha_{\rm logY_X}$	$\gamma_{\rm logM}$	$\gamma_{\rm logY_X}$
MUC	$0.057\,(0.04dex)$	$0.087\,(0.02dex)$	0.063	−0.063	−0.165	−0.166
MUCL	0.053	0.085	0.087	−0.087	−0.244	−0.245
MUW+MU2W	$0.044\,(-0.09dex)$	$0.075\,(-0.10dex)$	0.068	−0.067	−0.141	−0.143
MUWHS	$0.048\,(-0.05dex)$	$0.081\,(-0.04dex)$	0.078	−0.078	−0.122	−0.123

Table 4.5: Intrinsic scatter for $M_{\rm tot} - Y_{\rm X}$ at $\Delta = 500c$. In parenthesis, the increment with respect to MUCL simulations results.

gies present lower $\sigma_{\log \rm M}$ of $0.09dex$ and $0.05dex$ respectively, and $0.10dex$ and $0.04dex$ for $\sigma_{\log \rm Y_X}$. As in the $M_{\rm tot} - T_{\rm X}$ relation, we come across to the correlation between intrinsic scatter and σ_8; the more powerful a cosmological models is to build up massive halos, the larger the scatter we get. In any case, the uncertainty in scatter due to resolution is less important than the indetermination from cosmological modeling. Probing that $M_{\rm tot} - Y_{\rm X}$ is also a more robust that $M_{\rm tot} - T_{\rm X}$ to discriminate from cosmological parameters adjustment, in particular it is very sensitive to σ_8 variations since we find large variations in scatter between MUW+MU2W and MUWHS datasets.

Last but not least we examine the shape of the mass and $Y_{\rm X}$ distributions by means of the skewness and kurtosis. While deviations from gaussianity are apparent in all simulations, the variations among them are very similar with the exception of MUCL which presents a more negative skewness and kurtosis.

Worth noting is the fact that the shapes of the $M_{\rm tot} - Y_{\rm X}$ distributions are closer to a Gaussian than the values found in the $M_{\rm tot} - T_{\rm X}$ relation. Stanek et al. (2010) find the same trend between scaling relations in the sample of clusters at $\Delta = 200$ in their two samples, adiabatic clusters and preheated gas.

Scatter residuals

Here we are interested in determining what is the contribution of clusters to the intrinsic scatter. Undoubtedly the most interesting case is taking $Y_{\rm X}$ as independent variable to estimate total masses from observation of gas mass

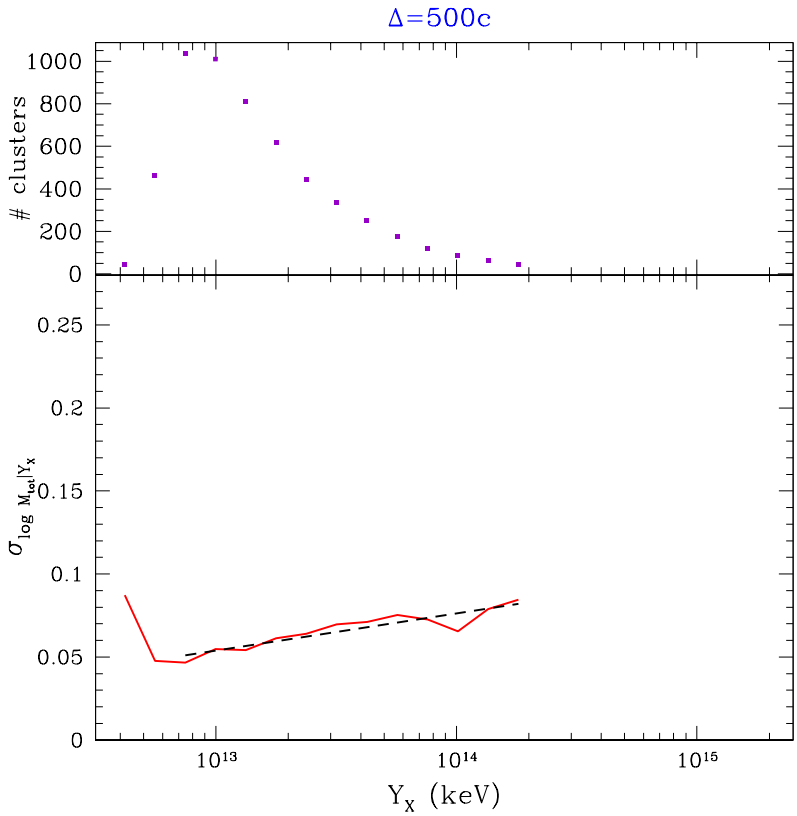

Figure 4.4: Same as figure 4.2 for the $M_{\rm tot} - Y_{\rm X}$ relation.

and temperature. Thus, this section is devoted exclusively to the analysis of residuals in mass at fixed $Y_{\rm X}$.

As in the $M_{\rm tot} - T_{\rm X}$ section, the residuals in mass are binned in equally spaced logarithmic bins along the independent variable. Following the procedure previously explained results into the residuals functions ($\sigma_{\log M_{\rm tot}|Y_{\rm X}}$) reported in table 4.6.

As an illustration, figure 4.4 plots the results obtained for the MUC simulation. Analogous plots for simulations MUCL, MUW+MU2W and MUWHS are inserted in appendix C in figures C.4, C.5 and C.6.

We begin the discussion by comparing $M_{\rm tot} - T_{\rm X}$ and $M_{\rm tot} - Y_{\rm X}$ for simulation MUC. In both relation we find increasing scatter with $T_{\rm X}$ and $Y_{\rm X}$ although $M_{\rm tot} - Y_{\rm X}$ has a flatter slope and lower normalization. Notice that these objects have equal mass resolution but increasing spatial resolution in their cluster profiles towards more massive halos. Less massive clusters has

Simulation	Residual functions	Range
MUC	$\sigma_{\log M_{\rm tot}\|Y_{\rm X}} = (0.023 \pm 0.003)\ Y_{\rm X} - (0.23 \pm 0.04)$	$7.45 \times 10^{12} < Y_{\rm X} < 1.81 \times$
MUCL	$\sigma_{\log M_{\rm tot}\|Y_{\rm X}} = (0.000 \pm 0.003)\ Y_{\rm X} + (0.06 \pm 0.05)$	$3.44 \times 10^{13} < Y_{\rm X} < 2.08 \times$
MUW+MU2W	$\sigma_{\log M_{\rm tot}\|Y_{\rm X}} = (0.03 \pm 0.02)\ Y_{\rm X} - (0.4 \pm 0.2)$	$3.47 \times 10^{13} < Y_{\rm X} < 9.36 \times$
MUWHS	$\sigma_{\log M_{\rm tot}\|Y_{\rm X}} = (0.03 \pm 0.01)\ Y_{\rm X} - (0.4 \pm 0.2)$	$2.72 \times 10^{13} < Y_{\rm X} < 1.03 \times$

Table 4.6: Same as table 4.3 for the $M_{\rm tot} - Y_{\rm X}$ relation.

lower spatial resolution and, hence, higher temperatures (see section 3.4.2). On the contrary gas masses are smaller, so the product $Y_{\rm X} = M_{\rm gas} T_{\rm X}$ is more robust that $T_{\rm X}$ alone.

Clearly the same can be shown in simulations MUCL which presents a completely flat function and lower overall values for $\sigma_{\log M_{\rm tot}|Y_{\rm X}}$. However the discrepancies are more prominent between 1024^3 and 512^3 resolution that if we consider clusters from the same simulation.

Finally, we look at simulations MUCL, MUW+MU2W and MUWHS to examine the impact of cosmology in the scatter residual function. We find two distinct behaviors between WMAP1 and the other cosmologies. MUCL is the only one with slope consistent with zero, but also a higher normalization. In addition, the range of validity of $\sigma_{\log M_{\rm tot}|Y_{\rm X}}$ is shifted towards bigger values of $Y_{\rm X}$ because that cosmological model has a larger σ_8 value.

On the other hand, MUW+MU2W and MUWHS has exactly the same $\sigma_{\log M_{\rm tot}|Y_{\rm X}}$ functions although figures C.5 and C.6 indicate noisier residuals for WMAP5-like cosmology. According to these results the change in σ_8 does not alter significantly the relative contribution of clusters to the intrinsic scatter. In other words, galaxy clusters seem to have roughly the same scatter in the whole $Y_{\rm X}$ range.

In summary, we have presented a set of measurements that indicate that $M_{\rm tot} - Y_{\rm X}$ not only a more robust estimator of scaling relation than $M_{\rm tot} - T_{\rm X}$. Besides, it is a better estimator for total masses due to the smaller scatter and it is less dependent on resolution and cosmology.

4.3 $L_X - T_X$ relation

The scaling relations which is more directly observable is the correlation between X-ray luminosity and global spectroscopic temperature. $L_X - T_X$ not only involves two directly observables, but it also plays an important role in discerning the physics behind the formation of galaxy clusters. It has been known long ago that the slope of the relation appears to fit $L_X \propto T_X^3$ (i.e. Edge & Stewart (1991), Fabian et al. (1994)) rather than $L_X \propto T_X^2$ as derived from the self-similar model. Many theoretical models have been proposed to explain such disagreement.

One of the proposed solutions is the so-called *preheating* of the ICM. It assumes that there is a source of heating, other that gravity, which increases the thermal energy of the gas at high redshift. This additional heating would decrease the central gas density and hence, the X-ray luminosity.

It has also been argued by Allen & Fabian (1998) that *cooling flows*, which can account up to 70% the total luminosity of a cluster, could be the responsible for the observed discrepancy in the slope of $L_X - T_X$. The ICM is the largest reservoir of energy in a galaxy cluster since it retains the energy released during the initial contraction. The hot atmosphere continuously loses energy by the emission of X-rays; but in the inner core, where the densest gas is located, the energy loss is higher and a *cooling flow* is formed. This region is where the cooling rate of gas is sufficiently high so that gas particle lose energy to radiation.

Unfortunately, cooling flows may not only be responsible for slope deviation. Fabian et al. (1994) and Markevitch (1998) report a large deviation from the mean $L_X - T_X$ because of them, making cooling flows to be one of the main sources of scatter. What is worse, strong cooling flows are present in more than half the low-redshift clusters (e.g. Edge et al. (1992)).

Given that cooling flows only cover a small region and the difficulties in their modeling, most authors exclude them from their analysis. Hence, the scatter is significantly reduced in studies where either clusters cores are excised (Markevitch 1998), or clusters are selected on the basis of having weak cooling cores (Arnaud & Evrard 1999).

The nature of the MARENOSTRUM simulations does not allow us to accurately model cluster cores. Yet, the overdensity criterion adopted ($\Delta = 500c$) implicitly exclude the inner region where cooling flows dominate the bolometric luminosity.

$L_{\rm X} - T_{\rm X}^{\dagger}$

Simulation	Minimum Mass	Norm	Slope	Correlation
MUC	$4 \times 10^{13} h^{-1} M_{\odot}$	44.768 ± 0.009	2.11 ± 0.03	0.9993
MUCL	$9 \times 10^{13} h^{-1} M_{\odot}$	44.64 ± 0.01	2.09 ± 0.05	0.9992
MUW+MU2W	$9 \times 10^{13} h^{-1} M_{\odot}$	44.77 ± 0.01	2.01 ± 0.06	0.9987
MUWHS	$9 \times 10^{13} h^{-1} M_{\odot}$	44.81 ± 0.02	1.9 ± 0.1	0.9930

† Temperatures are measured in units of 3 keV

Table 4.7: Best-fit for $L_{\rm X} - T_{\rm X}$ at $\Delta = 500c$. Slopes and normalizations are rounded matching the error accuracy. Last column reports the Pearson's correlation coefficients of binned data.

Intrinsic scatter

Following the same steps as in the previous sections of this chapter we report the best-fit $L_{\rm X} - T_{\rm X}$ for our datasets in table 4.7. In figure 4.5 we plot the analysis of $L_{\rm X} - T_{\rm X}$ intrinsic scatter for simulation MUC, as an illustration. We have chosen this simulations because it is the dataset with larger number of galaxy clusters and allow us to measure the distribution with great statistical precision. Moreover, the high mass resolution of MUC also translates into a larger spatial resolution due to the special features of the lagrangian codes.

The results for the other simulations considered in this chapter, namely MUCL, MUW+MU2W and MUWHS, are reported in table 4.8 and plotted in section B.3. Once again, we see a tight correlation in all datasets as in the $M_{\rm tot} - T_{\rm X}$ and $M_{\rm tot} - Y_{\rm X}$ scaling relations.

The best-fit laws show that, contrary to $M_{\rm tot} - T_{\rm X}$, the assumed cosmological model play an important role in the exact value of normalization, while the slope not so affected. Similar conclusion is drawn by Allen et al. (2001), although the cosmological parameters considered there has larger variations.

It is well-known that $L_{\rm X}$ is extremely sensitive to mergers due to the tremendous compression that gas suffers, so the radiation emitted is hugely boosted. Total mass and temperature must also be increased but to a lesser extent. Our results reported on tables 4.2 and 4.8 conclude that there is a systematic increase in the $\sigma_{\log {\rm L_X}}$ with respect to $\sigma_{\log {\rm M}}$. $\sigma_{\log {\rm T_X}}$, on the contrary, has not significant variation.

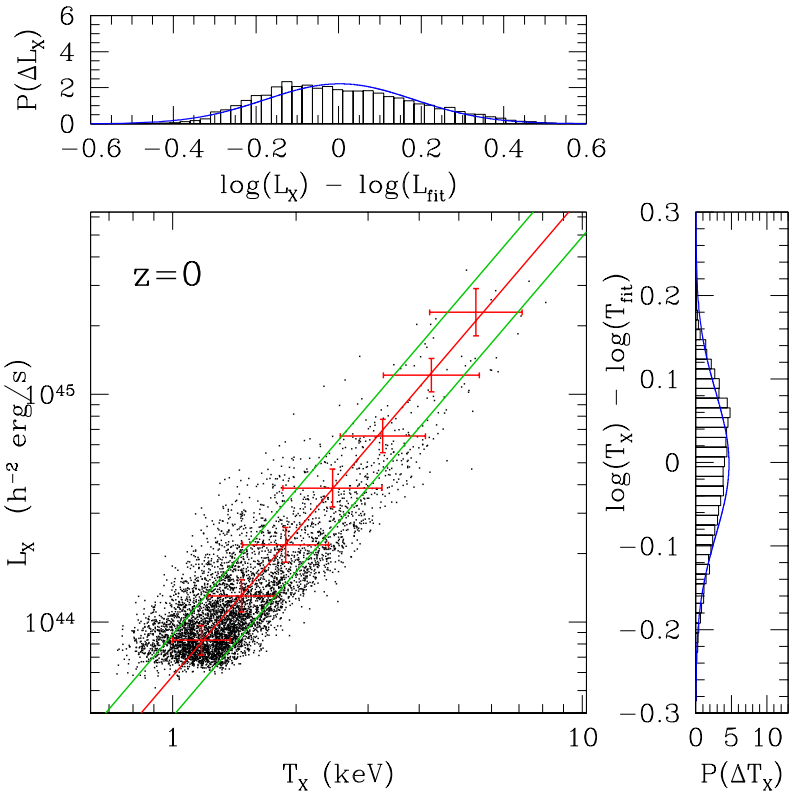

Figure 4.5: Same as figure 4.1 for $L_X - T_X$ relation.

The effect of merging as a source of scatter has been examined by Balogh et al. (2006), who came to the conclusion that galaxy clusters move along the $L_X - T_X$ scaling relation during those events. According to Balogh et al. (2006), merging has a negligible effect on increasing the intrinsic scatter and the discrimination by dynamical state is unnecessary in the estimation of scatter. Under this scheme, it is unclear whether merging and substructure is responsible for the L_X scatter.

Now we compare the scatter in $L_X - T_X$ among our datasets. As in the previous scaling relations simulations MUC shows larger scatter than its lower resolution counterpart, MUCL. Notwithstanding, L_X proves to be very sensitive to resolution according to the variations from MUCL to MUC, $\Delta\sigma_{\log L_X} = 0.37dex$ and $\Delta\sigma_{\log T_X} = 0.17dex$, the largest in the three scaling relations considered until now for these simulations.

Finally, simulations MUCL, MUW+MU2W and MUWHS allow us to establish

$L_{\rm X} - T_{\rm X}^{\dagger}$

Simulation	Scatter		Skewness		Kurtosis	
	$\sigma_{\log \rm L_X}$	$\sigma_{\log \rm T_X}$	$\alpha_{\rm logL_X}$	$\alpha_{\rm logT_X}$	$\gamma_{\rm logL_X}$	$\gamma_{\rm logT_X}$
MUC	$0.180\,(0.37dex)$	$0.085\,(0.17dex)$	0.047	−0.046	−0.344	−0.345
MUCL	0.143	0.068	0.032	−0.034	−0.495	−0.496
MUW+MU2W	$0.115\,(-0.28dex)$	$0.057\,(-0.11dex)$	0.050	−0.049	0.069	0.064
MUWHS	$0.134\,(-0.09dex)$	$0.070\,(0.02dex)$	0.031	−0.029	−0.432	−0.444

† Temperatures measured in units of 3 keV

Table 4.8: Best fit and intrinsic scatter for $L_{\rm X} - T_{\rm X}$ at $\Delta = 500c$. On parenthesis the increment with respect to MUCL simulations results

reasonable limits to the intrinsic scatter uncertainties due to cosmology. We find uncertainties up to $0.28dex$ in $L_{\rm X}$ and $0.11dex$ in temperatures for a reasonable range of values in the ΛCDM models considered here. It is worth noting the remarkable similarity between MUCL and MUWHS cosmologies.

Scatter residuals

Now we examine the distribution of scatter with $T_{\rm X}$. For this relation where both X-ray properties are directly observable we consider temperatures as independent. To this end we perform the same analysis discussed at the beginning of the chapter to estimate the behavior of $\sigma_{\log\, L_{\rm X}|T_{\rm X}}$in all our datasets. The best-fit functions for $L_{\rm X} - T_{\rm X}$ residuals in every simulation along with their validity range are listed in table 4.9.

We choose the clusters on the highest resolution simulation MUC, plotted in fig 4.6, as a example in this section. The analogous plots for simulations MUCL, MUW+MU2W and MUWHS available in figures C.7, C.8 and C.9, respectively.

Once again, we begin by focusing on the resolution effects derived from simulations MUC and MUCL. Both datasets present increasing scatter with cluster temperature, with very similar slopes. Normalizations, on the contrary, differ when the resolution is enhanced indicating an overall larger scatter for MUC clusters with an statistical accuracy of 4σ.

This is due to the higher spatial resolution in cluster profiles in massive

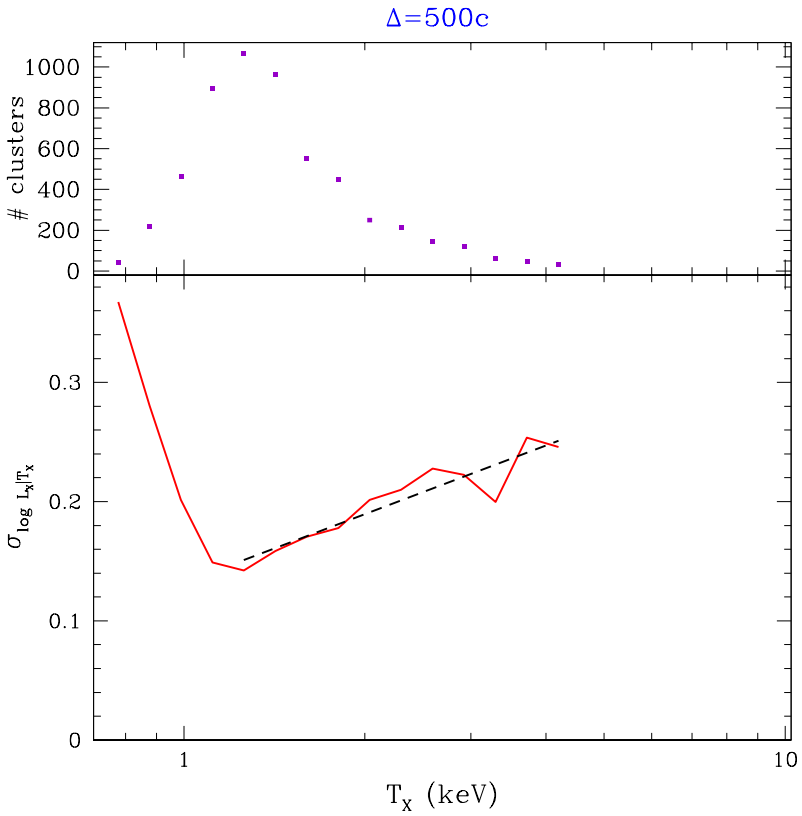

Figure 4.6: Same as figure 4.2 for the $L_X - T_X$ relation.

halos. In the SPH representation of gas of GADGET2, less massive clusters have a low number of particles to sample the ICM state so the mass show a more smoother distribution compared to the biggest clusters.

Although this is present in T_X and Y_X too, luminosities are more sensitive to the particular details of each cluster ICM and hence the effect is more prominent in the $L_X - T_X$ scatter.

Finally, simulations MUCL, MUW+MU2W and MUWHS will help us to investigate on how the intrinsic scatter is distributed according to cosmology. Unfortunately, a little can be argued from $\sigma_{\log L_X|T_X}$ functions because MUWHS is dominated by noise. Besides, both datasets MUW+MU2Wand MUWHS has a very limited temperature range of validity (see figs C.8 and C.9).

Variations driven by cosmology indicates a large dispersion in the slopes. In particular WMAP3 has the largest slope, almost 3 times the MUCL value. Regarding normalizations, no significant variations are found when cosmologi-

Simulation	Residual functions	Range
MUC	$\sigma_{\log L_X \mid T_X} = (0.19 \pm 0.02)\ (T_X/3\,keV) + (0.223 \pm 0.004)$	$1.26 < T_X < 4.20$
MUCL	$\sigma_{\log L_X \mid T_X} = (0.14 \pm 0.03)\ (T_X/3\,keV) + (0.128 \pm 0.003)$	$2.15 < T_X < 4.19$
MUW+MU2W	$\sigma_{\log L_X \mid T_X} = (0.37 \pm 0.03)\ (T_X/3\,keV) + (0.125 \pm 0.002)$	$2.34 < T_X < 3.02$
MUWHS	$\sigma_{\log L_X \mid T_X} = (0.26 \pm 0.07)\ (T_X/3\,keV) + (0.134 \pm 0.007)$	$2.11 < T_X < 2.99$

Table 4.9: Same as table 4.3 for the $L_X - T_X$ relation.

cal parameters are changed. Only simulation MUWHS present a slightly larger normalization but still consistent with WMAP1 and WMAP3 within the 1σ uncertainties.

In summary, we may conclude that enhancing the resolution of simulations increase the overall scatter of clusters with respect to $L_X - T_X$, keeping the temperature dependence of the residuals roughly constant. On the other hand, when cosmological parameters are changed the behavior seem to be the opposite. More massive clusters show larger dispersion to the mean relation while the normalization of $\sigma_{\log L_X \mid T_X}$remains constant.

4.4 $f_{\rm gas} - M_{\rm tot}$ relation

Baryon fraction in galaxy clusters provide a wealth of accessible cosmological information. They can be used to study the mix of dark matter and gas in the scales of *Mpc*. Apparently there is no efficient mechanism to segregate baryons and dark matter at these scales. Consequently it is often stated that $f_{\rm gas}$ within clusters must reflect the universal baryon fraction $\Omega_{\rm bar}/\Omega_{\rm m}$.

Using a non-radiative gas approach to explore baryon fraction is a reasonable approach simplification since the most of the ICM has a cooling time that exceeds the age of the Universe. During the last decade a number of studies have considered the cluster baryon fraction in the adiabatic regime. The main results of these studies are:

1. The baryon fraction evolves very weekly with time. We will address this point in chapter 6, devoted to the evolution of the scaling relations.

2. The baryon fraction is, in general, $\approx 10\% - 15\%$ lower than the universal average. For instance, Eke et al. (1998) report $0.85 - 0.9$ at the virial radius and the Santa Barbara Cluster Comparison Project (Frenk et al. 1999) established 0.92 averaged over all codes, finding a substantial scatter among codes and a systematic offset between SPH codes and grid-based ones. Kravtsov et al. (2005) found that baryon fractions with the ART code are about $3\% - 5\%$ higher than GADGET simulations of the same clusters.

3. Additional physics to the adiabatic modeling of gas can results into variations in the baryon fraction. Bialek et al. (2001), Muanwong et al. (2002) and Kay et al. (2003), to name some, report an enhancement in the "baryon depletion" by strong preheating. More recently several groups have presented analysis of simulations including gas cooling and star formation, e.g. Ettori et al. (2006), showing that radiative cooling can increase the total baryon fraction (gas+stars) and change the dependence on cluster mass.

Furthermore, some studies (i.e. Ettori (2003), McCarthy et al. (2007)) indicate slight discrepancies in the universal baryon fractions inferred from X-ray satellites and WMAP1 and WMAP3. This concludes that not all the ingredients in the cluster baryonic budget are considered, and up to $\sim 40\%$ of the total baryons in the Universe are actually located in the Warm-Hot

$f_{\rm gas} - M_{\rm tot}$

Simulation	Minimum Mass	Norm	Slope	Correlation
MUC	$4 \times 10^{13} h^{-1} M_{\odot}$	0.12 ± 0.02	-0.010 ± 0.001	-0.9719
MUCL	$9 \times 10^{13} h^{-1} M_{\odot}$	-0.12 ± 0.04	0.006 ± 0.003	0.7368
MUW+MU2W	$9 \times 10^{13} h^{-1} M_{\odot}$	-0.6 ± 0.1	0.042 ± 0.007	0.9408
MUWHS	$9 \times 10^{13} h^{-1} M_{\odot}$	-0.21 ± 0.09	0.013 ± 0.006	0.6698

Table 4.10: Best-fit for $f_{\rm gas} - M_{\rm tot}$ at $\Delta = 500c$. Slopes and normalizations are rounded matching the error accuracy. Last column reports the Pearson's correlation coefficients of binned data.

Intracluster Medium (see discussion in section 2.4, Cen & Ostriker (2006) and He et al. (2005)).

In the current section we explore the baryon fraction at $\Delta = 500c$ by means of our set adiabatic simulations to test the impact of cosmological models in the baryon fraction of galaxy clusters. A similar study using the MUC clusters alone at the virial radius can be found at Gottlöber & Yepes (2007). At this point it is important to underline that observations of several X-ray observatories, i. e. Roussel et al. (2000), Lin et al. (2003), Sadat et al. (2005), McCarthy et al. (2008), suggest that non-gravitational heating is largely unimportant for $T_{\rm X} \gtrsim 3keV$ ($M_{\rm tot} \gtrsim 2 \times 10^{14} h^{-1} M_{\odot}$) clusters.

Intrinsic scatter

In section 3.4.1 we stated that baryon fraction is extremely sensitive to lower resolution because of the poorer sampling of less massive clusters. In terms of the $f_{\rm gas} - M_{\rm tot}$ relation, the slopes tend to be more negative when those objects are not excluded from the cluster sample.

Previous studies on baryon fraction scaling relations are based in simulations with lower resolution than MUC which makes of them candidates to be bias. To name some Crain et al. (2007) has recently reported the results from the MGS, the second highest gasdynamical simulation in resolution at large-scale after MUC. According to our understanding, Crain et al. (2007) data may be misinterpreted to have a lower $f_{\rm gas}$ tale in the low $M_{\rm tot}$ regime.

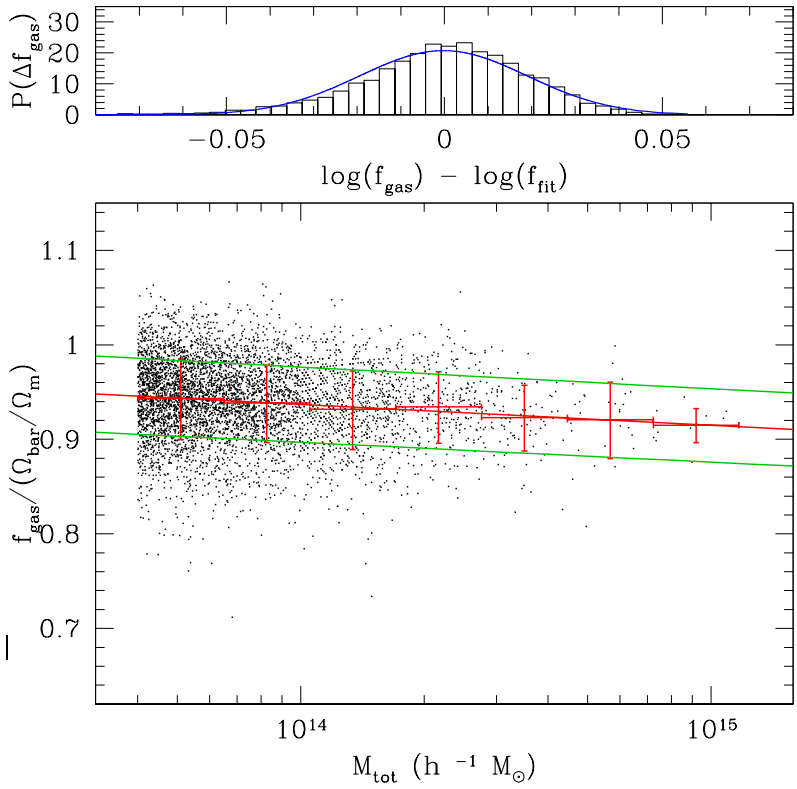

Figure 4.7: Intrinsic scatter for the $M_{\rm tot} - T_{\rm X}$ relation in simulation MUC at $z = 0$ and $\Delta = 500c$. *Top:* Histogram of logarithmic differences between cluster $M_{\rm tot}$ and best-fit relation. *Bottom:* Halos (black dots) and $2\sigma_{\log f_{\rm gas}}$ scatter (green surface).

To avoid this, we have carefully chosen the mass cut-off introduced at the beginning of this chapter. Despite the removal of these clusters, we have no arguments to discard that the scatter in low-$M_{\rm tot}$ clusters is unaffected. For this reason the conclusion of this section, especially for 512^3 resolution simulations, must be understood as estimates.

To compute the intrinsic scatter we begin by fitting the mean $f_{\rm gas} - M_{\rm tot}$ relation. The best-fit scaling relations and correlation coefficients of all our datasets are reported in table 4.10. Then, we build the histograms of cluster distance from the mean relations.

Contrary to the rest of X-ray properties, the baryon fraction can not be considered as a complete sample. As a consequence we can only study the

$f_{\rm gas} - M_{\rm tot}$

Simulation	Scatter $\sigma_{\log f_{\rm gas}}$	Skewness $\alpha_{\log f_{\rm gas}}$	Kurtosis $\gamma_{\log f_{\rm gas}}$
MUC	$0.019\,(-0.006dex)$	-0.094	1.185
MUCL	0.025	-0.189	1.156
MUW+MU2W	$0.029\,(0.004dex)$	-0.176	1.919
MUWHS	$0.024\,(-0.001dex)$	-0.100	1.004

Table 4.11: Best fit and intrinsic scatter for $f_{\rm gas} - M_{\rm tot}$ at $\Delta = 500c$. On parenthesis the increment with respect to MUCL simulations results.

intrinsic scatter when $M_{\rm tot}$ is the independent variable. In figure 4.7 we show such computation in the MUC clusters. Further plots the other datasets can be found in appendix B under section B.4. The parameters characterizing the $f_{\rm gas}$-histogram are reported in table 4.11.

Comparison between simulations in the $f_{\rm gas} - M_{\rm tot}$ best-fit relations show small discrepancies. In particular MUW+MU2W and MUWHS show larger deviations compared to WMAP1 simulations. What is more noticeable is that linear correlation, in general, is worse than in the previous relations due to the bias at lower-$M_{\rm tot}$ clusters.

On the one hand, MUC simulation which is less affected by biasing indicates a strong linear dependency. On the other, MUCL and MUW+MU2W indicates a blending in the $f_{\rm gas} - M_{\rm tot}$ clusters. Nevertheless, MUC and MUCL presents similar $f_{\rm gas}$ even in the low mass regime ($M_{\rm tot} \sim 10^{14} h^{-1} M_{\odot}$) proving that the low mass biasing has a minor effect at 512^3 resolution. Hence, the differences on $f_{\rm gas} - M_{\rm tot}$ reported in table 4.10 for WMAP3 and WMAP5-like cosmology are basically due to the different cluster formation history in each cosmology.

Nevertheless, such discrepancies between our set of simulations are of the same order of $f_{\rm gas}$ reported for other authors as Frenk et al. (1999) and Kay et al. (2004).

Looking at the intrinsic scatter in table 4.11 we do not find significant variations between the simulations at 512^3 resolution, with the exception of a higher kurtosis in MUW+MU2W. Table 4.11 also establishes a very similar

$\sigma_{\log f_{\rm gas}}$ between MUC and MUCL, but in contrast to the other scaling relations the higher resolution decrease the amount of intrinsic scatter.

Very little can be found in the literature about the scatter of baryon fraction to compare with. The recently released study from Young et al. (2010) using the MGS simulations is of particular interest for $f_{\rm gas} - M_{\rm tot}$. They use the MGS simulations and a semi-analytic model on top of them to compute $f_{\rm gas}$ measurements at $\Delta = 500$. Their adiabatic simulation, despite having a smaller mean $f_{\rm gas}$ value, presents an intrinsic scatter $\sigma_{\log f_{\rm gas}} = 0.018$ for their gravity-only run very similar to our measurements in MUC $\sigma_{\log f_{\rm gas}} = 0.019$ drawn from table 4.11 although they include cluster cores in their computation.

Probably, a more realistic estimate is given in Stanek et al. (2010), which study the same simulations but without the semi-analytic model. They explicitly compute the intrinsic scatter of $f_{\rm gas}$ reporting $\sigma_{\log f_{\rm gas}} = 0.036 \pm 0.001$ for their gravitation-only simulation at $\Delta = 200$. The fact that it is referred to a lower overdensity may be unimportant since baryon fraction profiles seem to converge at $\Delta \gtrsim 1000$ (see figure 6 in Kay et al. (2004)).

Stanek et al. (2010) is also compatible with the study by Crain et al. (2007), that report a rms scatter of 3% for halos chosen at random from their suite of simulations. However, Crain et al. (2007) scatter is computed for all halos with more than 500 particles, that may have low bias $f_{\rm gas}$ as we discussed in section 3.4.1. In both papers the scatter of adiabatic simulations agrees with our results although MUC has a slightly lower scattered, probably as a consequence of a better mass resolution with respect to MGS and the core removal in our sample.

Scatter residuals

Thanks to the analysis of the function $\sigma_{\log\, f_{\rm gas}|M_{\rm tot}}$ we can assess the mass-dependence of the scatter in our simulations. Results from the computation of the residuals functions are reported in table 4.12. Owing to the completeness of our samples in $M_{\rm tot}$, the range of valid results for the $\sigma_{\log\, f_{\rm gas}|M_{\rm tot}}$ distributions will be down to the mass threshold defining the datasets. Only high-mass bins need to be removed to avoid low statistical results.

Once again, we plot the MUC analysis as an example in figure 4.8 while other simulations samples are put off to section C.4.

We begin the discussion comparing the same WMAP1 model at two different resolutions. MUC and MUCL reflects, in terms of scatter, the same behavior

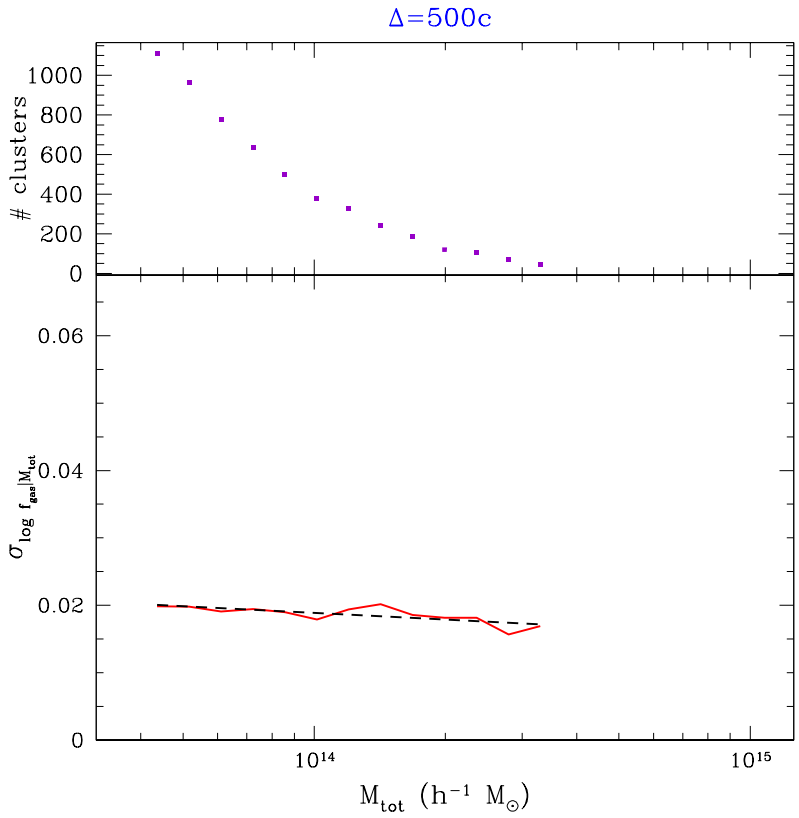

Figure 4.8: Same as figure 4.2 for the $f_{\rm gas} - M_{\rm tot}$ relation.

as in the scaling relation. Not only we found a decrease in the mean $f_{\rm gas}$ but also we notice increasing residuals towards at low $M_{\rm tot}$. While $\sigma_{\log\, f_{\rm gas}|M_{\rm tot}}$ remains almost completely flat at high resolution for the whole mass range, MUCL present a significant negative slope.

MUC clusters and the better resolved clusters in MUCL, the most massive ones, points to a common value of $\sigma_{\log\, f_{\rm gas}|M_{\rm tot}} \sim 0.02$ which eventually is the result obtained in the overall intrinsic scatter. Indeed, we conclude that MUC dataset has achieved convergence in resolution for $f_{\rm gas}$. In the lower mass regime, resolution produces a difference of $0.005\, dex$ for clusters at $M_{\rm tot} = 10^{14} h^{-1} M_\odot$.

Finally, we explore whether the discrepancies found in the intrinsic scatter with cosmological models are reproduced in the residuals functions of simulations MUCL, MUW+MU2W and MUWHS. All models tend to a common value of 0.02 at high masses. However, at low-$M_{\rm tot}$, WMAP1 and WMAP3 show a larger

Simulation	Residual functions	Range
MUC	$\sigma_{\log f_{\rm gas}\|M_{\rm tot}} = -(0.0033 \pm 0.0008)\ M_{\rm tot} + (0.07 \pm 0.01)$	$4.36 \times 10^{13} < M_{\rm tot} < 3.30 \times$
MUCL	$\sigma_{\log f_{\rm gas}\|M_{\rm tot}} = -(0.009 \pm 0.002)\ M_{\rm tot} + (0.14 \pm 0.03)$	$9.60 \times 10^{13} < M_{\rm tot} < 3.07 \times$
MUW+MU2W	$\sigma_{\log f_{\rm gas}\|M_{\rm tot}} = -(0.012 \pm 0.004)\ M_{\rm tot} + (0.20 \pm 0.04)$	$9.49 \times 10^{13} < M_{\rm tot} < 2.00 \times$
MUWHS	$\sigma_{\log f_{\rm gas}\|M_{\rm tot}} = (0.003 \pm 0.008)\ M_{\rm tot} + (0.0 \pm 0.1)$	$9.51 \times 10^{13} < M_{\rm tot} < 1.86 \times$

Table 4.12: Same as table 4.3 for the $f_{\rm gas} - M_{\rm tot}$ relation.

residual than simulation MUWHS. We believe this result is not significant since MUWHS has a large noise in the residual function.

Chapter 5

Cosmological dependence on cluster abundance

> Your eyes can deceive you; don't trust them.
>
> *Star Wars*, Obi-Wan Kenobi

The simplest way to quantify the cluster space density is to compute the X-ray Luminosity Function (XLF) by using a flux-limited sample and its corresponding survey volume (Rosati et al. 2002). A similar method but observationally quite different is to measure the intra-cluster gas temperature. Since $T_{\rm X}$ is related to cluster mass with the $M_{\rm tot} - T_{\rm X}$ relation we may study the cluster mass function through the X-ray Temperature Function, hereafter XTF.

From the discussion on chapter 4 it seems clear that the best observable property to trace cluster number density would be using $Y_{\rm X}$ instead of luminosity or temperature due to the small intrinsic scatter the $M_{\rm tot} - Y_{\rm X}$ relation has. Unfortunately, there is no flux-limited sample which takes into account cluster baryon masses.

5.1 Mass Functions

During this chapter we have considered the radius of clusters at $200\,\rho_{\rm crit}$ overdensity for analogy to the observational data we are going to compare with in the further sections. In figure 5.1 we plot the cumulative mass functions for

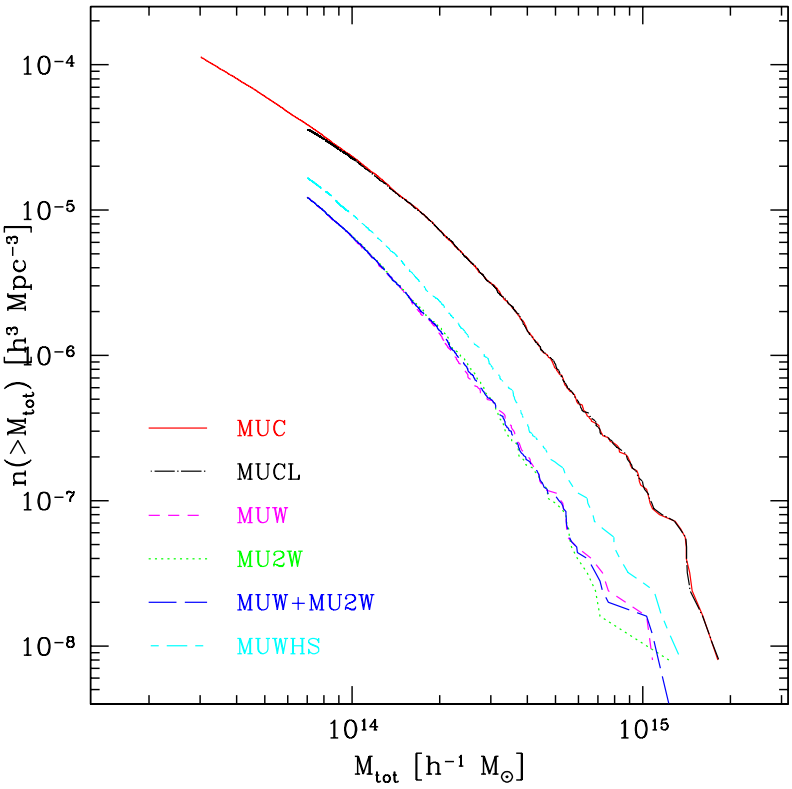

Figure 5.1: Cumulative mass functions of all simulations at $\Delta = 200$ and $z = 0$.

all simulations described in section 2.2. Red and black lines represent WMAP1 simulations at different resolution, 1024^3 and 512^3 respectively. Pink and green stand for the two WMAP3 simulations (MUW and MU2W) whereas blue line corresponds to the combination of them. Finally the cyan line represents the MUWHS mass function, a higher σ_8 cosmology based on WMAP3 cosmological parameters.

During this chapter the clusters sets we will use are determined by a minimum mass due to the limited mass of the subboxes extracted out of the original snapshots (see section 2.3.1). This minimum mass threshold is determined by the mass begin to flatten. They are $M_{200} = 3 \times 10^{13} h^{-1} M_\odot$ for the higher resolved simulation MUC and $M_{200} = 7 \times 10^{13} h^{-1} M_\odot$ for the 512^3 simulations.

As can be deduced from this figure, there are no significant resolution effects on the number of objects as a functions of resolution. The mass functions for simulation MUC and MUCL nicely overlap each other along the whole mass

range despite the fact that they differ by a factor of 8 in mass resolution and a factor of ~ 3 in spatial resolution.

On the other hand, there is a significant difference in the number of clusters depending on the cosmological model. The number density of objects with total masses $M_{200} \geq 5 \times 10^{14} h^{-1} M_{\odot}$ in both simulation with the low-normalization, WMAP3 cosmological parameters (MUW and MU2W), is ~ 10 times smaller than for the simulations of the concordance ΛCDM model. The MUWHS simulation with $\sigma_8 = 0.8$ has a number density ~ 2 higher than the simulations with WMAP3 cosmology, but still a factor of ~ 5 smaller than in the WMAP1 cosmology.

For the first time in this work, we have included simulations MUW and MU2W separately in order to account for the cosmic variance in the massive clusters tail. Figure 5.1 also shows that the effects of cosmic variance are not important in determining the abundance of clusters at these scales since the agreement of the mass functions for the two different realizations of the WMAP3 cosmological model clearly confirm this.

Therefore, we conclude that the estimation of the cluster mass functions from our set of simulations is robust and not likely to be affected by numerical effects. Now our purpose is to compare them with the data coming from X-ray observations of clusters. As our simulations include gas dynamics, we can directly measure the X-ray temperature from the gas content of our halos. In DM-only simulations, one has to rely on the mass-X-ray temperature relation to transform mass into temperature. Here, we will do the same exercise and compare the calculated X-ray temperature functions, hereafter XTF.

5.2 X-ray Temperature Function

The most recent published data for the XTF of nearby clusters uses temperatures derived from X-ray observations mainly by the *ASCA* satellite (Ikebe et al. (2002); Henry (2004b)) as a measure of the mean temperature of the ICM. The differences shown in the temperature of clusters from these two data sets reflect the systematic errors in then observed XTF.

In figure 5.2 we show the cumulative XTF as a function of the temperature for all clusters found in our set of simulations. We also represent the observational data as points with error bars as described in Henry (2004b). The observational data were rescaled to units of $h = 1$.

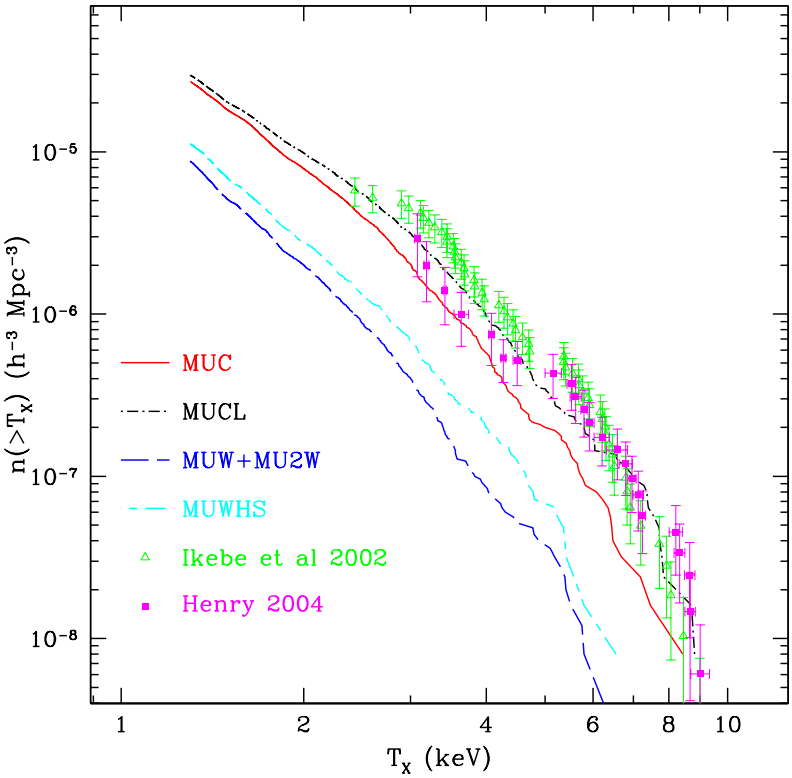

Figure 5.2: Mass functions of all simulations at $\Delta = 200$ and $z = 0$.

The predicted number density of X-ray clusters above a given temperature for the MUC and MUCL simulations with $\sigma_8 = 0.9$ are in good agreement with the observed data. We note that the level of agreement is considerably better that agreement achieved between simulations and data several years ago (e.g., Pierpaoli et al. (2001)).

Again, as in the case of mass, the WMAP3 most-favoured cosmological scenario underpredicts the density of X-ray clusters with respect to the observations by a factor of ~ 10 for clusters with $T_{\rm X} > 4\,keV$. The situations is slightly better for the higher normalization simulation MUWHS, but still predicts a factor of ~ 6 fewer density number of clusters hotter than $T_{\rm X} > 4\,keV$ than in reality.

We showed in figure 5.1 that effects of resolution are negligible in the estimate of the cumulative mass functions for massive clusters. This is not the case for the temperature estimates from the gas particles as we saw on the

discussion about the effects of resolution in the $M_{\rm tot} - T_{\rm X}$ relation on section 3.4.1. In order to check whether the XTF could be affected by resolution, we present in figure 5.2 a comparison between MUC and MUCL simulations. As can be seen, the spectroscopic temperature estimate of clusters is biased high when the low-mass resolution is used in a SPH simulation. Thus, we expect that the difference in the XTF shown between the MUC concordance model simulation with 1024^3 particles and the WMAP3 lower resolution simulations (512^3) is in fact a lower limit. Increasing the mass resolution of the latter will eventually lead to even larger differences respect to the MUC and the observational data.

5.3 $M_{200} - T_{\rm X}$ best-fit relations

The estimates previously introduced are based on the results from non-radiative gasdynamical simulations of clusters. There is still no clear answer to what extent cooling and star formation are important in the thermodynamics of the ICM. The extreme complexity of the processes involved presents a serious challenge for accurate simulation in a cosmological setting. Results from simulations that incorporate some modeling of these processes have shown that the $M_{200}-T_{\rm X}$ relation is not strongly affected by non-gravitational heating (Borgani et al. (2004), Nagai et al. (2007b)).

An important ingredient in the determination of the XTF from mass-functions is the intrinsic scatter of the $M_{200}-T_{\rm X}$ relation. If the scatter is large, a rather low normalization power spectrum can in principle give a high enough XTF to be compatible with observations. In the case we are dealing, simulations MUW, MU2W and MUWHS show lower number density of cluster and thus require lower normalization in their $M_{200} - T_{\rm X}$ relation. Given the very good statistical sample of objects in our simulations, we can accurately compute the $M_{200} - T_{\rm X}$ relation and also reliably estimate the intrinsic scatter due to the cluster dynamics. In this section we establish whether the intrinsic scatters of these simulation are sufficiently large to reconcile WMAP5-like cosmologies and X-ray observations.

The results of the $M_{200}-T_{\rm X}$ least-square fit for each simulation are reported in table 5.1. We have parametrized the relation as

$$\log\left(\frac{M_{200}}{h^{-1}M_{\odot}}\right) = M_0 + \alpha\,\log\left(\frac{T_{\rm X}}{3\,keV}\right) \tag{5.1}$$

where errors reported for slope (α) and normalization (M_0) correspond to

$M_{200} - T_{\rm X}$ best-fit

Simulation	α	M_0	ΔM_0 (99%)
MUC	2.03 ± 0.03	14.64 ± 0.01	0.43
MUCL	1.71 ± 0.02	1.492 ± 0.005	0.36
MUW+MU2W	1.52 ± 0.07	14.48 ± 0.02	0.27
MUWHS	1.54 ± 0.06	1.50 ± 0.01	0.30

Table 5.1: Best-fit parameters and scatter for the relation $\log M_{200} = M_0 + \alpha \log T_{\rm X}$. Masses are expressed in $h^{-1}M_\odot$ and temperatures in 3 keV.

1σ errors. We find a Pearson's correlation coefficient better than 0.99 in all simulations.

Furthermore, we have made an estimation for the intrinsic scatter in the $M_{200} - T_{\rm X}$ relation. As we saw in chapter 4, clusters are not distributed as a gaussian function towards the best-fit relation. In this chapter we are more interested in the region covered by the clusters in the mass-temperature plane rather than in a full scatter analysis. To this end we have simplified the procedure to estimate the scatter by defining the $M_{200} - T_{\rm X}$ scatter as the width which covers 99% of all clusters around the least-square fit. In other words, the scatter ΔM_0 reported in table 5.1 is such that encloses 99% within:

$$\log T_{\rm X} = (\log M_{200})/\alpha - M_0/\alpha \pm \Delta M_0/\alpha \tag{5.2}$$

Although formally there is no relation between ΔM_0 and the standard deviation σ, the meaning of ΔM_0 is very similar to the confidence interval at 3σ away from the gaussian mean. For the sake of simplicity, ΔM_0 can be regarded as the 3σ value of a normal distribution.

For our sets of clusters results are quantitatively similar than in chapter 4 for the $M_{\rm tot} - T_{\rm X}$ relation at $\Delta = 500c$. They show the same quantitative behavior depending on resolution and cosmology. As in table 4.2, we measure larger scatter in the higher resolution simulation MUC than in MUCL. Also, the intrinsic scatter raises as σ_8 is increased. Although all 512^3 simulations show very similar scatter values, roughly $\Delta M_0 \sim 30$.

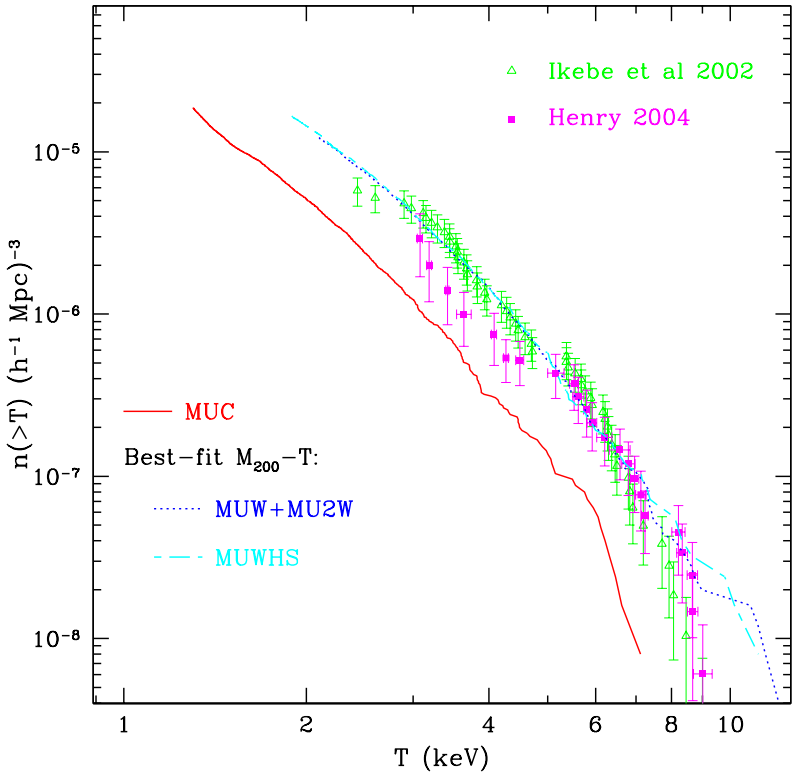

Figure 5.3: Mass functions of all simulations at $\Delta = 200$ and $z = 0$.

5.4 $M_{200} - T_{\rm X}$ predictions

Indeed an important questions arises with all this data: are the differences shown in figure 5.2 between the simulated XTF and data compatible with the intrinsic scatter of the $M_{200} - T_{\rm X}$ relations? In order to provide with a possible answer, we have estimated the M_0 and α parameters needed to accommodate the mass functions shown in figure 5.1 to the observational XTF data by a χ^2 minimization. We show in figure 5.3 the best-fit simulated XTF for the WMAP3-based simulations to the observational data points, together with the simulations results for the high-normalization MUC simulation.

As can be seen, the observational datasets present slight differences. While Henry (2004b) shows less number density of clusters at $T_{\rm X} < 5\,keV$, the abundance of objects at higher temperatures ($T_{\rm X} > 8\,keV$) is larger than in Ikebe et al. (2002) measurements. This could lead to different $M_{200} - T_{\rm X}$ results from the χ^2 minimization. For this reason we have chosen to apply the procedure

	All data		Ikebe et al. (2002) data		Henry (2004b) data	
Simulation	α	M_0	α	M_0	α	M_0
MUC	1.67	14.42	1.75	14.40	1.51	14.49
MUCL	1.68	14.41	1.71	14.40	1.50	14.49
MUW+MU2W	1.64	14.10	1.64	14.09	1.49	14.17
MUWHS	1.67	14.18	1.66	14.18	1.44	14.28

Table 5.2: $M_{200} - T_{\rm X}$ results from χ^2 minimization. Masses are expressed in $h^{-1}M_\odot$ and temperatures in 3 keV.

not only to the combination of datasets, also to each of them separately. It is significant the fact that for WMAP3-based cosmologies the number density of very massive clusters clearly exceeds the observational measurements.

We report the results for the χ^2 minimization in table 5.2. This table regards the obtained needed $M_{200} - T_{\rm X}$ relations to match observational XTF according to the mass functions in each cosmology. The minimization has been applied to Ikebe's and Henry's dataset independently and also to the combination of them. According to table 5.2, the normalization of the $M_{200} - T_{\rm X}$ relation needed to fit the observational XTF for the $\sigma_8 = 0.75$ MUW+MU2W simulations is a factor of $0.31 - 0.39\,dex$ smaller than the best-fit values shown in table 5.1. As we have seen the intrinsic scatter measured from our WMAP3 simulations is $\Delta M_0 = 0.27$. For the $\sigma_8 = 0.8$ MUWHS simulation this factor is $0.22 - 0.32\,dex$ whereas $\Delta M_0 = 0.30$ for this cosmology. In all simulations we find significant higher normalizations when Henry's clusters are considered alone because of the lower abundance at $T_{\rm X} \sim 3 - 5\,keV$ respect to Ikebe's set.

These results are quantitatively highlighted when we plot the χ^2 best-fit next to the simulation best-fit. In figure 5.4 we plot the clusters in MUW, MU2W and MUWHS simulations along with mock $M_{200} - T_{\rm X}$ relation obtained by the χ^2 minimization (blue dashed line). The green shaded region correspond to the surface occupied by the 99% of clusters between the 3σ scatter limits, in magenta lines. At the bottom, we see the percentage of clusters within the region for different values of scatter. The red mark represents the value ΔM_0 which contains 99% of all clusters. In both simulations the predicted $M_{200} - T_{\rm X}$ have a too lower normalization to be compatible with observations within the intrinsic scatter of clusters.

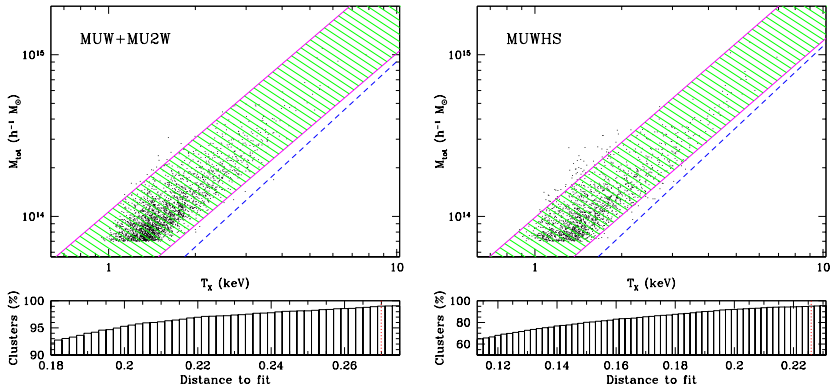

Figure 5.4: M_{200} vs $T_{\rm X}$ plot for clusters in MUW+MU2W (left) and MUWHS (right). *Bottom*: Percentage of clusters in region $\log M_{200} = \alpha \log T_{\rm X} + M_0 \pm \Delta M_0$. Red line correspond to 3σ intrinsic scatter (see text), reported in table 5.2. *Top*: Green shaded region represents the 3σ area around the least-square fit. Blue dashed line is the result from the χ^2 minimization to the XTF data.

5.5 Discussion

It is not clear that non-gravitational heating could affect the thermodynamics of the ICM in such a way that this could account for a factor $\sim 0.30\,dex$ lower normalization with respect to the predictions of the simulations reported here. For instance, the normalization for the emission-weighted temperature $M_{500} - T_{ew}$ from SPH simulations including cooling and star formation (Borgani et al. 2004) is a factor $0.16\,dex$ smaller than the obtained from the MUWHS simulation. If we compare the normalization of the spectroscopic $M_{\rm tot} - T_{\rm X}$ from radiative cluster simulations of Nagai et al. (2007b) with ours, the difference is within $0.17 - 0.20\,dex$.

In conclusion, it seems unlikely that we can reproduce the observational abundances of X-ray clusters with a normalization of the power spectrum as low as the best-fit value given by WMAP3. Recently, Rines et al. (2008) has reported that the revised estimates of cosmological parameters in WMAP5 agree with the mass function from the SDSS. From our results, a slightly higher normalization of $\sigma_8 = 0.8$ alleviates the problem although the cluster abundance still lies below the observational estimates. Considerably steeper slopes and lower normalization of the $M_{200} - T_{\rm X}$ relation are needed to reconcile the predicted mass functions of clusters with the observed XTF in this case. For the standard cosmological model, X-ray clusters of galaxies seem to prefer a

higher σ_8 than predicted by CMB anisotropies in WMAP3, in agreement with the abundance of optical clusters from SDSS standalone as reported in Rines et al. (2007) and Rozo et al. (2007). Very recently, Rozo et al. (2010) has performed a joint analysis of WMAP5 and *maxBCG* cluster catalog obtaining $\sigma_8 = 0.807 \pm 0.020$ in fully agreement with our MUWHS simulation.

CHAPTER 5. COSMOLOGICAL DEPENDENCE ON CLUSTER ABUNDANCE

IS WMAP3 NORMALIZATION COMPATIBLE WITH THE X-RAY CLUSTER ABUNDANCE?

GUSTAVO YEPES AND RAUL SEVILLA
Grupo de Astrofísica, Universidad Autónoma de Madrid, Madrid E-28049, Spain; gustavo.yepes@uam.es, raul.sevilla@uam.es
STEFAN GOTTLÖBER
Astrophysikalisches Institut Potsdam, An der Sternwarte 16, 14482 Potsdam, Germany; sgottloeber@aip.de
AND
JOSEPH SILK
Oxford Astrophysics, Denys Wilkinson Building, Keble Road, Oxford OX1 3RH, UK; silk@astro.ox.ac.uk
Received 2007 May 24; accepted 2007 July 20; published 2007 August 22

ABSTRACT

We present the mass and X-ray temperature functions derived from a sample of more than 15,000 galaxy clusters of the MareNostrum Universe cosmological SPH simulations. In these simulations, we follow structure formation in a cubic volume of 500 h^{-1} Mpc on a side assuming cosmological parameters consistent with either the first- or third-year *WMAP* data and Gaussian initial conditions. We compare our numerical predictions with the most recent observational estimates of the cluster X-ray temperature functions and find that the low-normalization cosmological model inferred from the 3 year WMAP data results is barely compatible with the present-epoch X-ray cluster abundances. We can only reconcile the simulations with the observational data if we assume a normalization of the mass-temperature relation, which is a factor of ~2.5–3 smaller than our nonradiative simulations predict. This deviation seems to be too large to be accounted by the effects of star formation or cooling in the ICM, which are not taken into account in these simulations.

Subject headings: cosmology: theory — galaxies: clusters: general — methods: numerical

Online material: color figures

1. INTRODUCTION

Clusters of galaxies are strong X-ray emitters that can be observed at large distances using the *XMM-Newton* and *Chandra* X-ray telescopes. They are excellent cosmological probes that can be used to put strong constraints on the matter density of the universe, (Ω_m), the normalization of primordial density fluctuations (σ_8), and the associated spectral index (n). The number of massive clusters in cold dark matter–dominated cosmologies is known to be exponentially dependent on σ_8 (Seth & Tormen 2002), as has been extensively confirmed by simulations. Therefore, the determination of the abundance of massive clusters gives one of the best constraints on the normalization of the initial power spectrum of density fluctuations, provided we adopt Gaussian initial conditions. An independent measurement of the cosmological parameters comes from the study of CMB anisotropies. The most recent data from the 3 year *WMAP* results (Spergel et al. 2007; WMAP3) gives a value of $\sigma_8 \sim 0.76 \pm 0.05$ to within 1 σ error. This is smaller than the previous value of $\sigma_8 = 0.84 \pm 0.04$ estimated from the first-year *WMAP* data (Spergel et al. 2003; WMAP1). This difference in the normalization and the matter content ($\Omega_m = 0.24$ vs. $\Omega_m = 0.3$) translates into large differences, up to an order of magnitude as we will show in this Letter, in the number density of the most massive objects formed at present in the universe. Other recent papers independently also argue against the low values of σ_8 obtained from WMAP3 (Evrard et al. 2007; Rozo et al. 2007).

In order to compare the theoretical cluster mass function for a particular cosmological model with the observed abundance of X-ray clusters as a function of the ICM gas temperature, one has to assume that the mass-temperature relation is sufficiently well known. The main obstacle is the accuracy in the determination of this relation. Small differences can lead to large changes in the determination of cluster mass (see, e.g., Henry 2004) from the X-ray temperature. Estimations of the M-T relation from gas dynamical simulations show large discrepancies, mainly due to numerical resolution effects as well as to the physics involved (see Ascasibar et al. 2006 for a review). Most previous numerical studies on the comparison of cluster mass functions and X-ray temperature and/or luminosity functions have either high numerical resolution and a low number of objects or larger statistics but with very low resolution.

The aim of this Letter is to study the X-ray cluster temperature function (XTF) obtained from a set of large-scale nonradiative gas dynamical simulations with sufficient numerical resolution and statistics to cover the range of temperatures for which observational estimates of the cluster abundance are known. Our main goal is to test whether the observed number of X-ray-emitting galaxy clusters can be obtained in a cosmological model with parameters consistent with WMAP3 or WMAP1 data at the present time. For this purpose, we compute the XTF directly from simulations and compare them with the most recent observational estimates. At the same time, we derive the values for the normalization of the M-T relation that best fit the simulation mass functions to the observed XTF and compare them with the M-T resulting from the simulations.

2. SIMULATIONS

To study the X-ray cluster abundance, we have performed a series of nonradiative SPH simulations with the GADGET2 code (Springel 2005) at the Barcelona Supercomputer Center. Starting at redshift $z = 40$, we followed the nonlinear evolution of structures in gas and dark matter (DM) to the present epoch ($z = 0$) within a comoving cube of 500 h^{-1} Mpc on a side. The so-called MareNostrum Universe is the SPH simulation with 2×1024^3 particles (MUC). We assumed a concordance cosmological model with the following parameters: total matter

TABLE 1
MAIN FEATURES OF THE SIMULATIONS USED IN THIS WORK

Name	N_p	Ω_m	h	σ_8	n	α	$\log M_0$	$\Delta \log M_0$
MUC	2×1024^3	0.3	0.7	0.9	1	1.89 ± 0.02	14.64 ± 0.01	0.46
MUCL	2×512^3	0.3	0.7	0.9	1	1.71 ± 0.02	14.52 ± 0.01	0.35
MUWHS	2×512^3	0.24	0.73	0.8	0.95	1.62 ± 0.05	14.56 ± 0.01	0.31
MUW	2×512^3	0.24	0.73	0.75	0.95	1.65 ± 0.04	14.54 ± 0.01	0.28
MU2W	2×512^3	0.24	0.73	0.75	0.95	1.65 ± 0.05	14.56 ± 0.01	0.28
MUW+MU2W	2×512^3	0.24	0.73	0.75	0.95	1.60 ± 0.04	14.54 ± 0.01	0.28

NOTES.—Here α and $\log M_0$ are the best-fit parameters of the $\log (M_{200}/M_0) = \alpha \log (T_X/3 \text{ keV})$ relation. Errors correspond to 1 σ of the linear fit. $\Delta \log M_0$ is the maximum scatter in the normalization (see text).

density $\Omega_m = 0.3$, baryon density $\Omega_b = 0.045$, cosmological constant $\Omega_\Lambda = 0.7$, Hubble parameter $h = 0.7$, slope of the power spectrum $n = 1$, and normalization $\sigma_8 = 0.9$. We also ran the same simulation with exactly the same initial data but lower mass resolution (2×512^3; MUCL), as described in Gottlöber & Yepes (2007).

After the release of the 3 year *WMAP* data, we complemented our numerical data set with new simulations of the same computational box but using WMAP3 cosmological parameters: $\Omega_m = 0.24$, $\Omega_b = 0.0418$, $\Omega_\Lambda = 0.76$, $h = 0.73$, $n = 0.95$, and $\sigma_8 = 0.75$. We have changed both Ω_m and σ_8 (rather than only σ_8) so as to remain on the *WMAP* degeneracy line for these two parameters. As in the concordance model, the power spectrum was kindly provided by Wayne Hu, who computed it by direct numerical integration of the Boltzmann code. We generated the initial conditions for the WMAP3-compatible simulations with 2×512^3 (MUW) particles in exactly the same way as for the MareNostrum Universe. In order to study the effects of cosmic variance, we have completed a second simulation with a different random realization (MU2W). Furthermore, and driven by the results obtained for the XTF from these simulations, we have also repeated the MareNostrum Universe realization of the WMAP3 cosmology, but with a higher normalization of the initial power spectrum ($\sigma_8 = 0.8$), consistent within 1 σ with the WMAP3 best fit (MUWHS). In Table 1 we summarize the main characteristics of the simulations and the corresponding acronyms for reference in what follows. The best-fit values of the mass-temperature relations from clusters obtained in each simulation are also shown in the last two columns (see § 4).

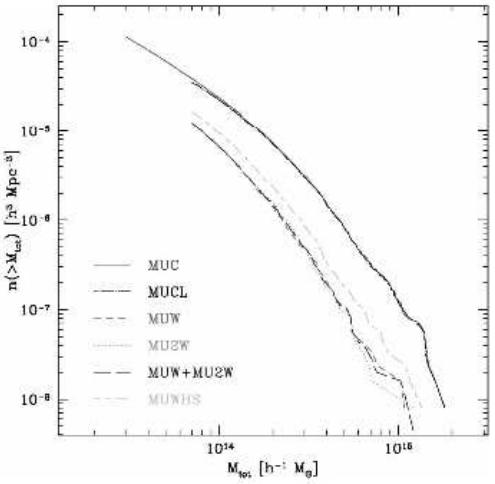

FIG. 1.—Cumulative mass function from the simulations described in the text and Table 1. [*See the electronic edition of the Journal for a color version of this figure.*]

The clusters have been identified in the simulations by means of a hierarchical friends-of-friends (FOF) halo finder, as described in Gottlöber & Yepes (2007). For comparison with observational data, we have estimated total masses (dark+gas) of clusters at different spherical overdensities (200, 500, 2500) with respect to the critical density. To this end, we started at the position of the most massive substructure of the clusters identified with FOF and used the "bound density maxima" algorithm (Klypin et al. 1999) to find the spherical overdensities.

3. CLUSTER MASS FUNCTIONS

In Figure 1 we plot the resulting cumulative mass functions for all the simulations described in Table 1. In this figure, the total mass of objects corresponds to the region enclosing an overdensity of 200 around the center of mass found as described in the previous section. As can be deduced from this figure, there are no significant resolution effects on the number of objects as a function of mass. The mass functions for simulations MUC and MUCL nicely overlap each other despite the fact that they differ by a factor of 8 in mass resolution and a factor of ~3 in spatial resolution. On the other hand, there is a significant difference in the number of cluster-size objects depending on the cosmological model. The number density of clusters with masses $M_{200} \geq 5 \times 10^{14}\ h^{-1}\ M_\odot$ in both simulations with the low-normalization, best-fit WMAP3 cosmological parameters, MUW and MU2W, is ~10 times smaller than for the simulations of the concordance ΛCDM model. The MUWHS simulation with $\sigma_8 = 0.8$ has a number density ~2 higher than the simulations with $\sigma_8 = 0.75$, but still is a factor of ~5 smaller than in the concordance cosmology. Finally, Figure 1 also shows that the effects of cosmic variance are not important in determining the abundance of clusters at these scales. The agreement of the mass functions for the two different realizations of the WMAP3 cosmological model clearly confirms this. On the other hand, we have also checked for the possible effects of small-volume sampling in the determination of the mass function for the most massive objects. To this end, we have compared our mass function for the MUWHS simulation with the mass function obtained from a DM-only simulation of the same cosmological model as MUWHS and the same number of particles, but with a larger computational volume (1.5 Gpc). This simulation has been done also at MareNostrum with the GADGET2 code by P. Fosalba for the

Dark Energy Survey. The agreement between the two mass functions is remarkable for halos with masses $M_{200} > 5 \times 10^{14}\ h^{-1}\ M_{\odot}$.

Therefore, we conclude that the estimation of the cluster mass function from our simulations is robust and not likely to be affected by numerical effects. Now our purpose is to compare them with data coming from X-ray observations of clusters. As our simulations include gas dynamics, we can directly measure the X-ray temperature from the gas content of our halos. In DM-only simulations, one has to rely on the mass–X-ray temperature relation to transform mass into temperature or vice versa. Here we will do the same exercise and compare the calculated XTFs.

4. X-RAY TEMPERATURE FUNCTION

The most recent published data for the XTF of nearby clusters uses temperatures derived from X-ray observations mainly by the *ASCA* satellite (Ikebe et al. 2002; Henry 2004) as a measure of the mean temperature of the ICM. The differences shown in the temperatures of clusters from these two data sets reflect the systematic errors in the observed XTF. For our simulated clusters, we computed several temperature estimations. These include the emission-weighted temperature (T_{ew}), computed by weighting the temperature of each SPH particle within the cluster by its X-ray luminosity. We also computed the spectroscopic temperature (T_X), following the procedure described in Vikhlinin (2006), which is supposed to give a more accurate value of the observed temperature of an X-ray-emitting plasma. Therefore, in what follows we will use T_X for the simulated clusters.

In Figure 2 we show the cumulative XTF as a function of the spectroscopic T_X for the clusters found in simulations described in Table 1. We also represent the observational data as points with error bars as described in Henry (2004). The observational data were rescaled to units of $h = 1$.

The predicted number density of X-ray clusters above a given temperature for the MUC and MUCL simulations with $\sigma_8 = 0.9$ is in good agreement with the data. Again, as in the case of mass, the WMAP3 most-favored cosmological model underpredicts the density of X-ray clusters with respect to the observations by a factor of ~10 for clusters with $T_X > 4$ keV. The situation is slightly better for the higher normalization MUWHS simulation. But still, it predicts a factor of ~6 fewer density of clusters hotter than $T_X > 4$ keV than in reality.

We showed in Figure 1 that effects of resolution are negligible in the estimate of the cumulative mass function for massive clusters. This could not be the case for the temperature estimates from the gas particles. In order to check whether the XTF could be affected by resolution, we also show in Figure 2 a comparison of the XTF between MUC and MUCL simulations. As can be seen, the spectroscopic temperature estimate of clusters is biased high when low-mass resolution is used in a SPH simulation. Thus, we expect that the difference in XTF shown between the MUC concordance model simulation with 1024^3 particles and the WMAP3 lower resolution simulations (512^3) is in fact a lower limit. If we increased the mass resolution of the latter, we would obtain a larger difference with respect to the MUC and data.

5. DISCUSSION

We have shown in the previous sections that the low-normalized WMAP3 cosmological simulations underpredict the abundance of X-ray clusters by a factor that ranges between 6 and 10 with respect to estimates from *ASCA* observations. Now our estimates are based on the results from nonradiative gas dynamical simulations of the ICM. There is still no clear answer to what extent cooling and star formation are important in the thermodynamics of the ICM. The extreme complexity of the processes involved presents a serious challenge for simulating them accurately in a cosmological setting. Results from simulations that incorporate some modeling of these processes have shown that the M-T relation is not strongly affected by nongravitational heating (Borgani et al. 2004; Nagai et al. 2007). A rather more important ingredient in the determination of the XTF from mass functions is the intrinsic scatter of the M-T relation. If the scatter is big, then a rather low normalization power spectrum can in principle give a high enough XTF to be compatible with observations. Given the very good statistical sample of objects in our simulations, we can reliably estimate not only the M-T relation but also the intrinsic scatter due to the cluster dynamics. In Table 1 we report the least-squares fit values of the $M_{200}/M_{\odot}\,h^{-1} = (M_0/M_{\odot}h^{-1})(T_X/3\ \mathrm{keV})^{\alpha}$ for the different simulations where errors in both the slope α and normalization M_0 correspond to 1 σ in the fit. We can also make a reliable estimate of the intrinsic scatter in the M_{200}-T_X relation. The linear fit of the $\log M_{200}$ versus $\log T_X$ has a Pearson's correlation coefficient better than 0.99 for all simulations. The maximum intrinsic scatter, $\Delta \log M_0$, is also shown in Table 1. It is defined as the value for which 99% of all the clusters used in the fit have their spectroscopic temperature within the values $\log T_X = (\log M_{200})/\alpha - \log M_0 \mp \Delta \log M_0$. As can be seen, the values of the scatter are between 0.28 and 0.31 dex (factor ~2 with respect to M_0) for the WMAP3 simulations. But are the differences shown in Figure 2 between the simulated XTF and data compatible with this intrinsic scatter of the M-T relation? In order to give a possible answer to this question, we have estimated the M_0 and α parameters of the M_{200}-T_X relation

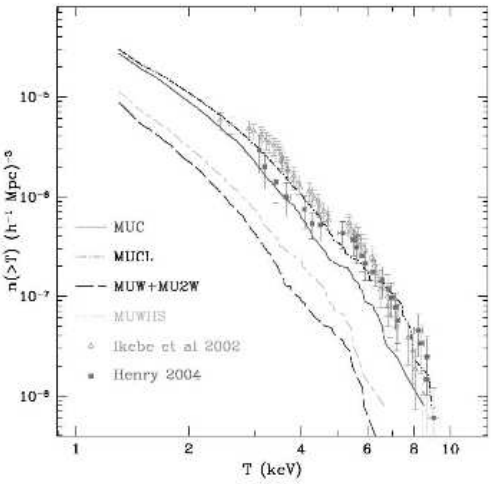

FIG. 2.—Cumulative XTF for two different cosmologies. Same notation as in Fig. 1. Filled triangles and squares represent Ikebe et al. (2002) and Henry (2004) data, respectively. Errors were computed as explained in Henry (2004). [*See the electronic edition of the Journal for a color version of this figure.*]

needed to accommodate the mass functions shown in Figure 1 to the observational XTF data by a χ^2 minimization. We show in Figure 3 the best-fit simulated XTF for the WMAP3 simulations to the observational data points, together with the simulation results for the high-normalization MUC simulation. The χ^2 best-fit values found for the MUW+MU2W simulations are $\alpha^{\rm I} = 1.64$ and $\log M_0^{\rm I} = 14.09$ for the Ikebe et al. data and $\alpha^{\rm H} = 1.49$ and $\log M_0^{\rm H} = 14.17$ for the Henry data. When both observational data sets are taken together in the fit, we obtain $\alpha^{\rm I+H} = 1.64$, $\log M_0^{\rm I+H} = 14.10$. For the higher normalization WMAP3 simulation MUWHS, we find $\alpha^{\rm I} = 1.66$, $\log M_0^{\rm I} = 14.18$ for Ikebe; $\alpha^{\rm H} = 1.44$, $\log M_0^{\rm H} = 14.28$ for Henry; and $\alpha^{\rm I+H} = 1.67$, $\log M_0^{\rm I+H} = 14.18$ for the combined data sets. Now if we fix the slope α to the best-fit value obtained from each simulation (see Table 1), we find a value for the normalization parameter $\log M_0 = 14.10$–14.13 for WMAP3 $\sigma_8 = 0.75$ simulations and $\log M_0 = 14.19$–14.22 for the $\sigma_8 = 0.8$ WMAP3 simulation. Finally, if we assume a self-similar behavior of the M-T scaling relation, $\alpha = 3/2$, then the best-fit values for M_0 are quite similar: $\log M_0 = 14.20$–14.26 for the MUWHS simulation and $\log M_0 = 14.12$–14.17 for the MUW+MU2W simulations. Therefore, the normalization of the M_{200}-$T_{\rm X}$ relation needed to fit the observational XTF for the $\sigma_8 = 0.75$ MUW and MU2W simulations is a factor of 0.40–0.45 dex (~2.5–2.8 times) smaller than the best-fit values shown in Table 1. For the $\sigma_8 = 0.8$ WMAP3 MUWHS simulation this factor is 0.36–0.39 dex (~2.3–2.4 times). As we have seen, the maximum scatter derived from our WMAP3 nonradiative gas dynamical simulations is $\sim \pm 0.28$–0.31 dex (i.e., a factor of ~2). It is not clear that nongravitational heating could affect the thermodynamics of the ICM in such a way that this could account for a factor of ~2.5–2.8 lower normalization with respect to the predictions of the simulations reported here. For instance, the normalization for the emission-weighted M_{500}-$T_{\rm ew}$ from SPH simulations including cooling and star formation (Borgani et al. 2004) is a factor of 1.46 smaller than the value we obtained for our MUWHS simulation. If we compare the normalization of the spectroscopic M_{500}-$T_{\rm X}$ from the radiative cluster simulations of Nagai et al. (2007) with ours, the difference is within a factor of 1.5–1.6.

In conclusion, it seems unlikely that we can reproduce the observational estimates of abundance of X-ray clusters with a normalization of the power spectrum as low as the best-fit value given by WMAP3. A slightly higher normalization of $\sigma_8 = 0.8$ alleviates the problem, although the cluster abundance still lies below the observational estimates. Considerably steeper slopes and lower normalization of the M-T relation are needed to reconcile the predicted mass functions of clusters with the observed XTF in this case. Alternative explanations that retain a low normalization of σ_8 appeal to the effects of primordial non-Gaussianity (Sadeh et al. 2006) or to dynamical dark energy (Bartelmann et al. 2006). However, for the standard cosmological model, X-ray clusters of galaxies seem to prefer a higher σ_8 than predicted by the CMB anisotropies, in agreement with the abundance of optical clusters from SDSS (Rines et al. 2007; Rozo et al. 2007).

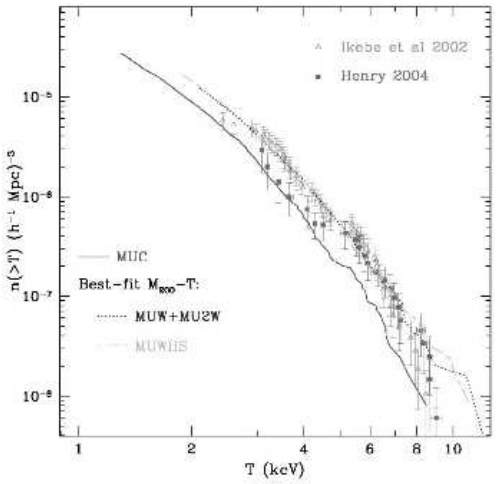

FIG. 3.—Best-fit cumulative XTF to data from WMAP3 simulation mass functions (see Fig. 1) and varying the two free parameters of the M_{500}-$T_{\rm X}$ relation. The XTF from the MUC simulation is shown for comparison. [*See the electronic edition of the Journal for a color version of this figure.*]

The MareNostrum Universe simulations have been done at BSC-CNS (Spain) and analyzed at NIC Jülich (Germany). We thank AI Hispano-Alemanas and DFG for financial support. G. Y. acknowledges support from MEC grants FPA2006-01105 and AYA2006-15492-C03. We thank P. Fosalba, A. Vikhlinin, and W. Hu for providing us with their data.

REFERENCES

Ascasibar, Y., et al. 2006, MNRAS, 371, 193
Bartelmann, M., Doran, M., & Wetterich, C. 2006, A&A, 454, 27
Borgani, S., et al. 2004, MNRAS, 348, 1078
Evrard, A. E., et al. 2007, ApJ, submitted (astro-ph/0702241)
Gottlöber, S., & Yepes, G. 2007, ApJ, 664, 117
Henry, J. P. 2004, ApJ, 609, 603
Ikebe, Y., Reiprich, T. H., Böhringer, H., Tanaka, Y., & Kitayama, T. 2002, A&A, 383, 773
Klypin, A., et al. 1999, ApJ, 516, 530
Nagai, D., Vikhlinin, A., & Karvtsov, A. 2007, ApJ, 655, 98
Rines, K., Diaferio, A., & Natarajan, P. 2007, ApJ, 657, 183
Rozo, E., et al. 2007, ApJ, submitted (astro-ph/0703571)
Sadeh, S., Rephaeli, Y., & Silk, J. 2006, MNRAS, 368, 1583
Seth, R. K., & Tormen, G. 2002, MNRAS, 329, 61
Spergel, D. N., et al. 2003, ApJS, 148, 175
———. 2007, ApJS, 170, 377
Springel, V. 2005, MNRAS, 364, 1105
Vikhlinin, A. 2006, ApJ, 640, 710

Chapter 6

Evolution of Scaling Relations

> You can't stop the change any more than you can stop the suns from setting.
>
> *The Phantom Menace*, Shmi Skywalker

Scaling relations enable us to estimate the masses of clusters from X-ray observables. However, it is necessary to ensure that they are well calibrated over a wide redshift range. At low redshift, scaling relations are reasonably well calibrated, at least for relaxed clusters. However, there are degeneracies between cosmological parameters that eventually lead to the same scaling laws at the current epoch.

Measurements of how the scaling relations evolve in time may broke the degeneracies if the survey spans a range wide enough in mass to include information from the shape of the mass function (Hu 2003). So, we can improve cosmological constraints derived from the mass function.

However, measuring these relations at high-redshift is considerably more challenging. Observations of cluster properties at high-redshift have recently become available owing primarily to the high sensitivity of CHANDRA and XMM-Newton. Observationally, several studies of X-ray scaling relation evolution have been carried out in the recent years, (e.g., Vikhlinin et al. (2002), Ettori et al. (2004b), Kotov & Vikhlinin (2005), Maughan et al. (2006), O'Hara et al. (2007), Morandi et al. (2007)). Unfortunately, the observational picture is far from settled.

From a theoretical point of view, we can now fully begin to exploit simulations to resolved high-redshift clusters and compare their X-ray properties with

real observations. Theoretical studies of cluster formation have mainly concentrated on explaining the lack of self-similarity inherent at low-redshift, rather than the evolution of the scaling laws, by including numerous non-radiative mechanisms. However, Muanwong et al. (2006) proves that the thermal history of the ICM depend on the particular radiative processes considered, so we should see differences in the evolutionary behavior. Therefore, given sufficient amount of quality observational data, it should be possible to rule out unsuitable theoretical models.

Simulations of structure formation without radiative cooling and feedback processes induce clusters that nearly follow the self-similar scaling prescriptions at $z = 0$. Several studies based in observations and radiative simulations (e.g. Maughan (2007), Kotov & Vikhlinin (2005), Branchesi et al. (2007)) indicate that the evolution of the scaling relations derived for more realistic clusters is consistent with the self-similar model in some aspects.

In the recent years of simulation of galaxy clusters, the effort has been focused in having an accurate description of the complex physical processes involving gasdynamics down to scales of parsecs at the expense of numerical resolution. But yet, there has not been a detailed analysis of adiabatic simulations accurately determining how is the evolution of the scaling relations of self-similar clusters.

In the present chapter we revisit the evolution of cluster scaling relations from a theoretical perspective. Our goal is to establish how high-resolution adiabatic scaling laws evolve to serve as a baseline for evaluation of non-radiative physical processes at intermediate and high-redshifts. As far as we are aware of, this is the first time this has been attempted.

6.1 Evolution in the self-similar model

With simple dimensional arguments and neglecting non-gravitational physics, it is possible to express the X-ray properties of the ICM as simple power-law scalings with mass and redshift, it is the so-called *self-similar model* (Kaiser 1986). With the additional assumption that clusters are spherically symmetric systems and that the ICM is in hydrostatic equilibrium with the underlying dark matter potential it is straightforward to derive the self-similar scaling relation (see appendix A).

We define the cluster radius r_Δ as the radius of a spherical volume within the mean matter density is Δ times larger than the critical density at redshift

z, $\rho_{\rm crit,z}$. According to this definition of Δ, all the evolution with redshift is embedded in the dimensionless factor E_z, defined as $E_z^2 = H^2(z)/H_0^2 = \Omega_{\rm m}\,(1+z)^3 + \Omega_\Lambda$ for a flat ΛCDM cosmology.

Note that there are other ways to define the scale radius of clusters. If radius is measured with respect to the mean density of the Universe, $\Omega_{\rm m}\rho_{\rm crit,z}$, the E_z factors are to be replaced by $(1+z)$. Another possibility is to assume a redshift-dependent density contrast Δ_z that is proportional to $\Delta_{vir,z}$. With this choice, the evolutionary factors E_z become $E_z\,\Delta_z^{1/2}$ instead.

With this discussion we want to stress that predictions for the evolution of cluster population are clearly dependent on how the scale radius is defined, so caution must be taken when comparing results from different authors.

6.2 Temporal dependence of the scaling relations

The large volume and high resolution of the MARENOSTRUM simulations allow us to resolve statistically a significant number of clusters at high redshift. In addition, the WMAP1 cosmology has the largest initial normalization of the power spectrum and the abundance of galaxy clusters is larger for the whole redshift range considered in this analysis, and hence, allow us to resolve more objects at earlier epochs. For all this reasons, we have chosen the MUC clusters as a testing ground for this study on evolution.

The cluster sample have been constructed by picking up the galaxy clusters at 5 different redshifts, namely $z = 0, 0.25, 0.5, 0.75$ and 1; using the procedure described in section 2.3 at each redshift. The analysis has been performed at $\Delta = 500c$ and $\Delta = 200$ overdensities with respect to the critical density estimated at the epoch of analysis. Notwithstanding, the main study will focus on $\Delta = 500c$ as it is typically the smallest density contrast accessible to the current X-ray observations at $z = 0$ and neglects the region where gravity does not play the major role. In addition, the X-ray properties within an overdensity of $500c$ exhibit less scatter in their mass-observable relations, due to the core removal and the lower virialization at larger radii, than at smaller overdensities as it is stated by Rudd (2007).

To avoid selection biases we have set-up a minimum mass threshold to define a complete sample, in an analogous way that in previous chapters. However, the minimum mass threshold is set to the value where the $z = 1$ mass

Relation (Y-X-z)	Δ	α	β	γ	r
$E_z M_{\rm tot} - T_{\rm X} - z^{\dagger}$	500c	14.544 ± 0.022	1.723 ± 0.052	0.304 ± 0.105	0.986
	200	14.672 ± 0.014	1.730 ± 0.036	-0.162 ± 0.068	0.993
$E_z M_{\rm tot} - E_z Y_{\rm X} - z$	500c	5.596 ± 0.116	0.632 ± 0.008	0.073 ± 0.051	0.997
	200	5.572 ± 0.095	0.628 ± 0.007	-0.117 ± 0.036	0.998
$E_z^{-1} L_{\rm X} - T_{\rm X} - z^{\dagger}$	500c	44.813 ± 0.020	2.026 ± 0.051	1.261 ± 0.108	0.990
	200	44.835 ± 0.023	2.099 ± 0.064	1.262 ± 0.123	0.987
$f_{\rm gas} - E_z M_{\rm tot} - z$	500c	0.079 ± 0.022	-0.008 ± 0.001	0.021 ± 0.005	0.776
	200	0.064 ± 0.019	-0.007 ± 0.001	0.047 ± 0.004	0.937

† Temperatures are measured in units of 3 keV

Table 6.1: Best-fit for all relations at $\Delta = 500c$ and 200. α, β and γ are defined in eq. 6.1. Seven bins were taken at every redshift to avoid low-mass biasing.

function flattens. Since the universe creates more massive clusters from that epoch, the sample is complete at all redshifts. We have selected all clusters to be $E_z M_{\rm tot}^{500c} > 7 \times 10^{13} h^{-1} M_{\odot}$ and $E_z M_{\rm tot}^{200} > 1.1 \times 10^{14} h^{-1} M_{\odot}$ in order to have a uniform subsets of this sample at all redshifts and overdensities considered. At $z = 0$ we have 18198 clusters in our E_z mass-limited sample, decreasing to 528 clusters at $z = 1$.

Galaxy clusters clearly do follow the self-similar prescription as we have stated in chapter 3.4 at $z = 0$. It is convenient to describe their behavior using a generalized power-law function. In this work we will use the general form

$$\log Y = \alpha + \beta \log X + \gamma \log(1 + z) \tag{6.1}$$

where α sets the normalization, β is the slope of the relation and γ determines the overall evolution in time.

The multi-dimensional fit has been performed by binning the cluster sample into 7 uniform bins at each redshift. By doing this, we guarantee that any redshift contribute equally to the best-fit regardless the abundance of galaxy clusters, otherwise the resulting scaling relations would be bias towards $z = 0$ and low-mass objects which are the more abundant.

Again, the binning is based on cluster masses, however in this case we have preferred evenly spaced bins in $E_z M_{\rm tot}$ (instead of solely $M_{\rm tot}$) since it takes into account the passive evolution of cluster masses. In table 6.1 we report the results which are to be discussed in the following sections.

6.3 $E_z M_{\rm tot} - T_{\rm X} - z$ relation

We now present how the Mass-to-Temperature relation evolve with redshift. In figure 6.1 we present the $E_z M_{\rm tot} - T_{\rm X} - z$ relation at overdensity $\Delta = 500c$. In each panel the simulated galaxy clusters are plotted along with the best-fit relation from table 6.1. Green crosses illustrate the mass bins taken at each redshift which eventually are fitted to get the $E_z M_{\rm tot} - T_{\rm X} - z$ law. Each error bar determines the weight in the fitting procedure independently of redshift.

Besides, we have overplotted the results reported by Kay et al. (2007) of the CLEF simulation. This numerical experiment is very similar to the details of our MUC simulation. It is a large cosmological simulation, $N = 2 \times 438^3$ particles within a $200\,h^{-1}Mpc$ comoving box, where detected clusters create a temperature-limited sample from redshifts $z = 0$ to $z = 1$. Their cosmological model adopted is consistent with WMAP1 as in our simulation, with the only difference that $\Omega_{\rm bar}$ is slightly higher. The initial conditions were evolved using GADGET2 including radiative cooling, star formation and strong energy feedback.

Apart from the numerical and physical similarities between MUC and CLEF, the computation of cluster properties is what makes Kay et al. (2007) sample really adequate for comparison with our data. In their paper, they report evolution of $M_{\rm tot} - T_{\rm X}$ and $L_{\rm X} - T_{\rm X}$ relations for clusters excluding the cores within $50\,h^{-1}kpc$. We leave the qualitative comparison between CLEF clusters evolution and ours for the final discussion at the end of the chapter.

From the observational point of view, several papers have been devoted to the observation of galaxy clusters at high-redshift. Unfortunately, the individual details of each ones makes impossible a comprehensive full comparison of all of them. We have selected those ones that are closer to the definitions used in our simulated clusters:

- Vikhlinin et al. (2009) introduce the result of the *CHANDRA Cluster Cosmology Project* (CCCP). They report a survey of 36 low-redshift and 49 high-redshift clusters observed with CHANDRA and based on the

ROSAT All-Sky Survey, computed assuming a WMAP1 cosmological model. The data reductions procedure includes removal of substructures and the inner core up to $15\%\, r_{500}$, reducing considerably the scatter in X-ray properties. Temperatures have been measured according to the definition of T_{spec} (Vikhlinin 2006), which is the same one we have adopted.

- Kotov & Vikhlinin (2005) report the analysis of 10 galaxy clusters in the redshift range $z = 0.4-0.7$ observed with XMM-Newton, also assuming a WMAP1 model. These data derive total masses and T_{spec} within $70\, kpc < r < r_{500}$ modeling the surface brightness profile by a modified β model.

- Vikhlinin et al. (2006) take a lower redshift range ($z < 0.24$) in their analysis of 13 relaxed galaxy clusters observed with CHANDRA. To compute the distance-dependent quantities they assume the concordance model WMAP1. The X-ray properties reported in this paper are computed at $\Delta = 500$ and $\Delta = 2500$, excluding the central $70\, kpc$ from the T_{spec} computation to avoid strongly cooled temperatures at these radii.

- Kotov & Vikhlinin (2006) present the analysis of 6 relaxed clusters at $z = 0.4-0.54$ in a WMAP1 cosmology. The same approach as in Vikhlinin et al. (2006) is followed to derive the total cluster masses within r_{500} assuming hydrostatic equilibrium but without assuming isothermality of the ICM gas.

- Maughan et al. (2008b) analyze one of the very few clusters with a hydrostatic mass estimate beyond $z = 1$.

- Sun et al. (2009) report a systematic analysis of 40 nearby galaxy groups ($M_{500} = 10^{13} - 10^{14} h^{-1} M_{\odot}$, $z < 0.12$) based on the CHANDRA archival set. Group properties are integrated at different characteristic radii; r_{2500}, r_{1500}, r_{1000} and r_{500}. Data reduction method is similar to the "standard" formalism developed by Vikhlinin et al. (2006). Temperatures are also defined as T_{spec} within the annulus $0.15\, r_{500} < r < r_{500}$; baryon fractions are also provided.

- Mantz et al. (2009) derive X-ray scaling relations using flux-selected galaxy clusters. We have taken the data for 96 clusters in the range $z < 1.7$. Temperatures are obtained by fitting the spectra to a single-temperature thermal emission model integrated in $0.15\, r_{500} < r < r_{500}$, providing results consistent with that of Vikhlinin et al. (2009). They also report core-excised bolometric luminosities.

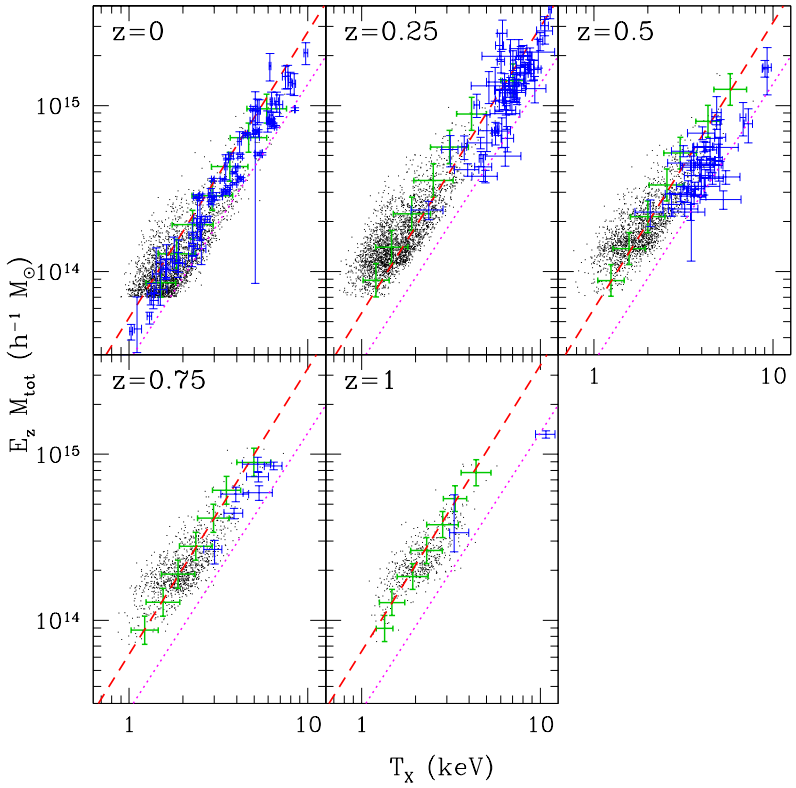

Figure 6.1: $E_z M_{\rm tot} - T_{\rm X} - z$ best-fit reported in table 6.1 for $\Delta = 500c$. Halos (black dots) and binning (green bins) at each redshift range. Red line represents the best-fit $E_z M_{\rm tot} - T_{\rm X} - z$, blue crosses are real clusters data taken from a compilation of observational studies (see text). Magenta line shows the scaling obtained from cooling simulation by Kay et al. (2007).

In the case of duplicity of clusters we have chosen the most recent paper which more closely matches our definitions of temperatures and inner core exclusion.

Note that not all papers reject the cluster profiles at $z < 0.15\, r_{500}$ which eventually makes the relation to have a larger scatter due to the presence of cooling cores. As shown by Kay et al. (2007) in cluster simulations, although cooling and heating processes are more efficient there, the $M_{\rm tot} - T_{\rm X}$ relation at r_{500} is less susceptible to the effects associated with the core.

Data in figure 6.1 has been segregated into 5 redshifts range; $z \leq 0.125$, $0.125 < z \leq 0.375$, $0.375 < z \leq 0.625$, $0.625 < z \leq 0.875$ and $0.875 < z$;

corresponding to the snapshots analyzed in simulation MUC.

The comparison show that the normalization of our simulated clusters are systematically higher by $\approx 25\%$ with respect to the observed clusters, at all redshifts. This bias agrees with further results from simulated clusters where non-adiabatic physics are considered (e.g. Nagai et al. (2007a)). Only the cluster 1226+3332 at $z = 0.8880$, from Vikhlinin et al. (2009), has an offset larger than the overall bias.

Several papers have dealt with the systematics introduced to estimate cluster mass derived from observed surface brightness maps (i.e. Rasia et al. (2006), Nagai et al. (2007a), Jeltema et al. (2008)). They compute that the hydrostatic estimate of the gravitationally bound mass is biased low by $\sim 20\%$. In the above studies, $M_{\rm tot}$ is computed from simulated clusters using two different methods. The first one, by computing the true mass directly from the simulations; and the second one, mocking flux maps from simulations to estimate $M_{\rm tot}$ using standard observational techniques. The goal is to evaluate systematic effects in the observational procedures in recovering the mass measurements.

These papers conclude that reconstructed masses based on the hydrostatic equilibrium are underestimated by $\sim 20\%$. In addition, Jeltema et al. (2008) finds a strong correlation between cluster substructure and bias in the hydrostatic masses supporting the idea that the bias is due to additional pressure support from turbulent gas motions.

Besides, on the observational side, high-redshift galaxy clusters are confirmed to be more disturbed than those at low-z (i.e. Jeltema et al. (2005), Maughan (2007), Hashimoto et al. (2007)). Combined with the correlation between substructure and hydrostatic mass bias, this leads to systematically larger errors in mass estimates at high redshifts. Coming back to figure 6.1, we appreciate that observations present larger bias than MUC clusters up to $z = 0.5$. At larger redshifts, the observations are to scarce for a significant behavior.

It is important to remark that, although cluster cores have been removed in the studies of Rasia et al. (2006) and Nagai et al. (2007a), the size of systematic biases and uncertainties depends on the physical processes included in the simulations themselves. Nevertheless, the comprehensive study of Rasia et al. (2006) underlines that the hydrostatic equation provide a more robust mass estimate than other methods used observationally.

The bottom line is that the intrinsic scatter due to different dynamics in

the clusters formation plays a role as important as radiative processes. And thus, we are able to reproduce $M_{\rm tot} - T_{\rm X}$ observations with a large sample in opposition to radiative runs that can only simulate small number of clusters.

6.4 $E_z M_{\rm tot} - E_z Y_{\rm X} - z$ relation

Recent works have shown that the total gas pressure is a signal that scales with cluster mass with low scatter (LaRoque et al. 2005). In addition, X-ray imaging and spectroscopy has confirmed that $Y_{\rm X}$ strongly scales with $M_{\rm tot}$ as a power-law (e.g., O'Hara et al. (2007), Maughan (2007)). The redshift behavior on galaxy cluster is still not well-known observationally, although recent works has begun to probe evolution in X-rays to $z \sim 1$. The nice properties that $Y_{\rm X}$ has proven to have makes it the first candidate to study galaxy clusters at $z \gtrsim 1$, where evolution can more accurately distinguish between cosmological models.

In figure 6.2 we represent the results obtained for the best-fit $E_z M_{\rm tot} - E_z Y_{\rm X} - z$ relation in table 6.1, MUC clusters and observational results from Vikhlinin et al. (2009), Maughan et al. (2008b), Sun et al. (2009) and Mantz et al. (2009).

From the compilation of observations discussed in the previous section, only Maughan et al. (2008b) and Mantz et al. (2009) explicitly report a M_{gas} measure. To increase the observational sample we have inferred $Y_{\rm X}$ measures from Vikhlinin et al. (2009) and Sun et al. (2009) The former from by computing M_gas from their reported baryon fraction and $M_{\rm tot}$; the latter, extracting data from plots by means of the *g3data* software.

Other studies has also been discarded despite having a large number of high-z cluster measurements because total mass and $Y_{\rm X}$ are not independently determined, e.g. Vikhlinin et al. (2006), Pratt et al. (2010).

Looking at figure 6.2 we find no observational data available at intermediate redshifts, $z = 0.5 - 0.75$. Despite in the previous section those redshifts were populated, most of the data comes from Vikhlinin et al. (2009) who do not report explicitly their $Y_{\rm X}$ measurements. In addition, Vikhlinin et al. (2009) derive total cluster masses through pre-calibrated $M_{\rm tot} - Y_{\rm X}$ and $M_{\rm tot} - M_{gas}$ relations. We have decided to discard that study given that $M_{\rm tot}$ and $Y_{\rm X}$ are not independent.

Nevertheless, our simulations accurately reproduce the observed clusters at

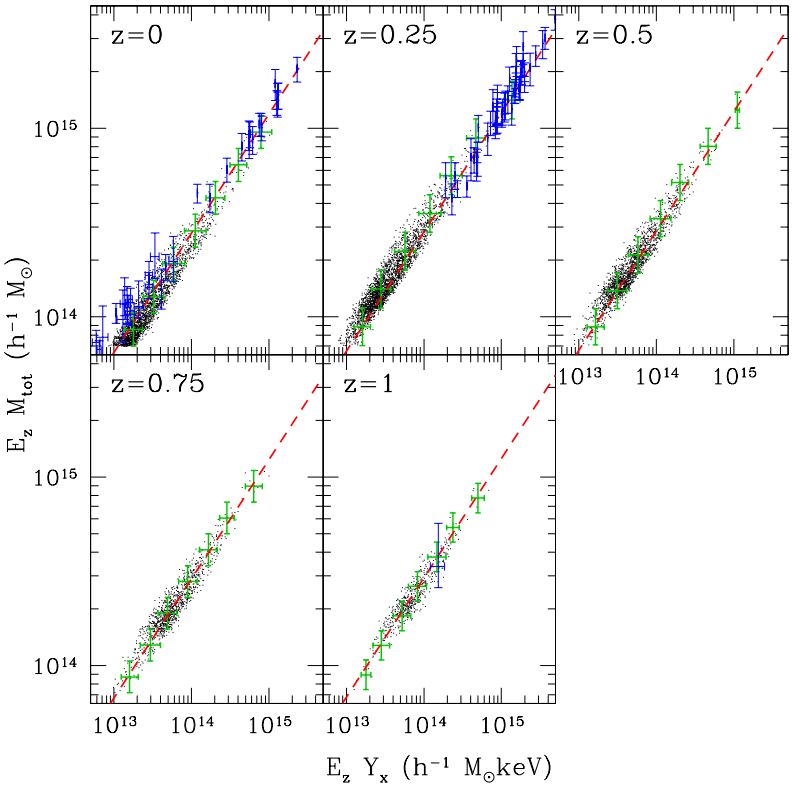

Figure 6.2: $E_z M_{\rm tot} - E_z Y_{\rm X} - z$ relation and best-fit as seen on table 6.1 for $\Delta = 500c$. See text for a detailed overview on the observational data.

all redshifts. At $z = 0$ simulated and real clusters indicate a good agreement. At $z = 0.25$ despite the sample provided by Mantz et al. (2009) comprises objects with higher masses than our sample, the $E_z M_{\rm tot} - E_z Y_{\rm X} - z$ relation is remarkably good. Finally, the global properties of cluster XLSSJ022403.9-041328 (Maughan et al. 2008b) at $z = 1.05$ is consistent also with the $E_z M_{\rm tot} - E_z Y_{\rm X} - z$ relation of table 6.1.

From the comparison between simulated and real clusters we can derive two conclusions related to the number counts of clusters and intrinsic scatter at $z > 0$.

Firstly, although the MUC dataset comprises a number of massive clusters, more massive clusters are needed ($M_{\rm tot} \sim 10^{15} M_\odot$) in order to sample the region surveyed by observations. This point is also seen in fig 6.1 for the $M_{\rm tot} - T_{\rm X}$ observations. To solve it, larger simulation volumes than $500\, h^{-1} Mpc$ are needed.

We have mentioned in previous chapters that $M_{\rm tot} - Y_{\rm X}$ is more robust and has less intrinsic scatter than $M_{\rm tot} - T_{\rm X}$. According to figures 6.1 and 6.2 we may visually assess that at larger redshifts the SZ proxy is also better behaved than $T_{\rm X}$. The second conclusion is that, judging by the error bars in observations, the observational methods to analyze real clusters induce uncertainties which happen to be larger than the intrinsic scatter of the $M_{\rm tot} - Y_{\rm X}$ expected at any redshift.

6.5 $E_z^{-1} L_{\rm X} - T_{\rm X} - z$ relation

Since cluster luminosities relate to mass and temperature we may study their X-ray emission via $L_{\rm X} - M_{\rm tot}$ or $L_{\rm X} - T_{\rm X}$. The practical approach is to use the relation with temperature instead of that between luminosity and mass. This makes sense because the estimation of $M_{\rm tot}$ from X-ray data is always based on $T_{\rm X}$, via the assumption of hydrostatic equilibrium. We have chosen to follow this way to avoid observational systematics in the comparison of real clusters.

In figure 6.3 we plot the $E_z^{-1} L_{\rm X} - T_{\rm X} - z$ data for our cluster sample at $\Delta = 500c$ in black dots. As in the previous relations, the best-fit reported in table 6.1 is represented by the dashed red line and observations by blue bars. In addition, we overplot the results from the CLEF simulation by Kay et al. (2007) as in section 6.3.

$L_{\rm X}$ is indeed the X-ray property more accessible observationally because it is directly measured. X-ray photons are detected in each X-ray instrument within given energy bandpass. For traditional reasons the more widely used is the range between $0.1\,keV$ and $2.4\,keV$ employed by the first breakthrough X-ray observatory, ROSAT.

In contrast, we compute cluster the bolometric luminosities as the integral of the whole emission spectrum (see section 3.3) instead of only in the ROSAT bandpass. The fact that we take into account the whole X-ray emission instead of that in a limited band constrain the available observations to be plotted in fig 6.3.

From the compilation described in section 6.3, only clusters from Kotov & Vikhlinin (2005) and Maughan et al. (2008b) report bolometric luminosities. Besides, Maughan et al. (2008a) and Pratt et al. (2010) also report bolometric $[0.1{-}100\,keV]$ luminosities and spectroscopic temperatures in the $(0.15{-}1)\,r_{500}$ region. In all these studies cores are removed unless clusters show an irregular

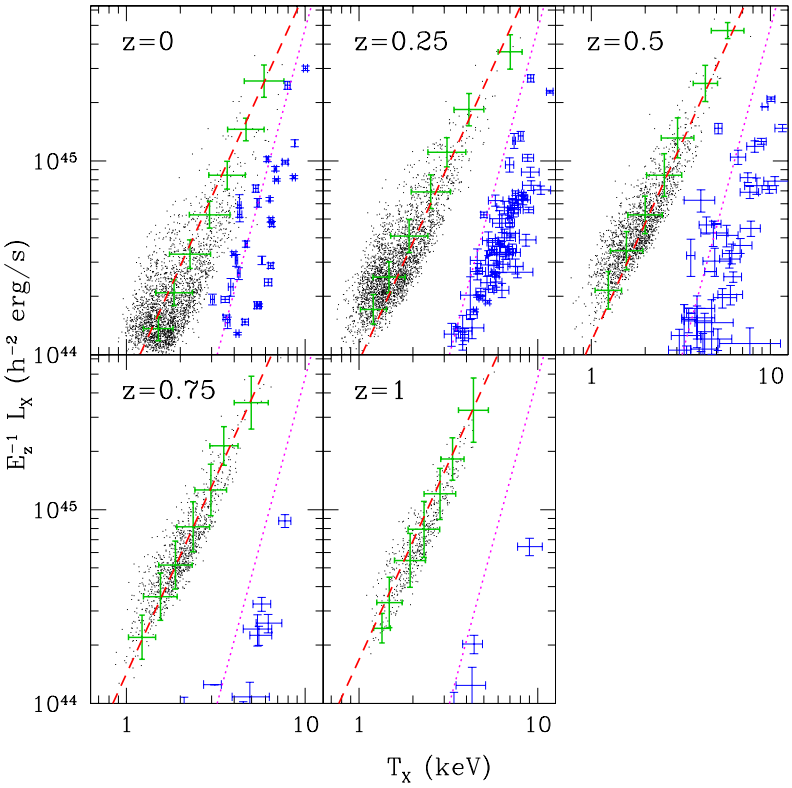

Figure 6.3: $E_z^{-1}L_X - T_X - z$ relation and best-fit as seen on table 6.1 for $\Delta = 500c$. Symbols and lines are the same as in figure 6.1.

morphology.

We can still increase the observational sample by cross-correlating data from different authors. To this end, we have also added the study of Novicki et al. (2002) which measures bolometric luminosities of 85 galaxy clusters at $z < 0.6$ observed by the ASCA satellite. 34 of these clusters are also reported by Vikhlinin et al. (2006), Kotov & Vikhlinin (2006), Vikhlinin et al. (2009) and Mantz et al. (2009), from where we get their T_X results. Novicki et al. (2002) luminosities are computed from $\Delta = 500$ to the very center of cluster and does not differentiate between cool and non-cool clusters. As a consequence we expect larger scatter in these set of observations.

The resulting $E_z^{-1}L_X - T_X - z$ relation from MUC simulation depicted in figure 6.3 indicates a poor agreement with real clusters. The normalization of our simulation is higher producing more luminous objects. More massive

clusters are better modeled than galaxy groups, this is expected since the radiative cooling is more efficient to gas content in poor systems.

The steeper $L_X - T_X$ is justified by additional physical processes in the ICM[1]. This is not surprising since the $L_X - T_X$ relation of several nearby cluster catalogs observed with the first-generation of X-ray satellites showed a departure from the predicted self-similar slope $\beta = 2$, e.g. Edge & Stewart (1991), David et al. (1993) and Rosati et al. (2002), with a measured value of $\beta \sim 3$.

As original suggested by Bryan (2000) and Voit & Bryan (2001), cooling provides a selective removal of low-entropy gas from the hot phase. As a consequence, only gas having a relatively high entropy will be observed as X-ray emitter. In other words, non-radiative clusters present a rich substructure formed by clumps of low-entropy gas that, because of the dependence $L_X \propto \rho^2$, contribute significantly to the luminosity. In radiative runs, this low-entropy gas is removed in high-density regions so that more smooth X-ray structure remains in the ICM.

Although the net effect of this process is very dependent on the details of the radiative physics implemented, we can have an overall idea by returning to figure 6.3 where CLEF simulation results are plotted. Kay et al. (2007) scaling relation show a selective reduction in L_X that bring numerical clusters closer to observations.

However, radiative simulations still presents discrepancies to be solved. For instance, we see that CLEF results still do not match observations for $z > 0.25$ and the slope is too steep even compared with nearby clusters. The latter is a consequence of spurious numerical effects that steepen $L_X - T_X$. When equal mass particles are employed in a given simulation, the smallest clusters have poorer resolution and hence their luminosities tend to be systematically underestimated as compared with more massive ones.

This effect can steepen the slope of the simulated $L - T$ relation. What is worse, at higher redshifts, where clusters are smaller and formed by less number of particles, local details on the density structure may be smoothed and, hence, ICM may be poorly sampled at sufficiently large z. Our simulation is less susceptible to suffer from this because it has larger mass and spatial resolution than all radiative simulation performed so far.

[1] An extensive review of the role played by these processes can be found in Borgani & Kravtsov (2009).

6.6 $f_{\rm gas} - E_z M_{\rm tot} - z$ relation

Since the mass fraction of hot gas measured from observations depends on the luminosity distance at the cluster redshift, tracing the evolution of this fraction as a function of redshift may be a powerful independent geometrical constraint on the dark energy content of the Universe. In combination with tight constraints on $\Omega_{\rm m}$, $f_{\rm gas}$(z) data contain sufficient information to break the degeneracy between $\Omega_{\rm m}$ and the dark energy equation of state, w. The additional combination of $f_{\rm gas}$ and CMB data breaks other important degeneracies between parameters in cosmological analysis (Rapetti et al. (2005), Allen et al. (2008)).

During the last two decades, the new observational facilities have uncovered some puzzles on this area. Incidentally, more specific questions arise to be solved in the next decade (Kravtsov et al. 2009). Among them, we now turn our interest to how the observed baryon budget in clusters constrain models of galaxy formation.

Unfortunately, our set of simulations does not allow us to answer that a question given because no stellar components can be formed in our galaxy clusters. However, an accurate adiabatic model is compulsory to understand of the net effect of the additional physical processes acting at low-scales. The current section is devoted to establish such foundation for future studies on the evolution of the $f_{\rm gas}$.

In figure 6.4 we plot the $f_{\rm gas} - E_z M_{\rm tot} - z$ relation obtained from MUC simulation at $\Delta = 500c$. From the point of view of simulations Young et al. (2010) studies $f_{\rm gas}$ in different formation scenarios using the MGS simulations. Shaded region of fig. 6.4 represent their result of the gravitational-only simulation (GO) which has no substantial mass dependence. Although their reported baryon fraction $f_{\rm gas}/(\Omega_{\rm bar}/\Omega_{\rm m}) = 0.894$ is slightly below our sample, the $f_{\rm gas} - M_{\rm tot}$ relations are compatible within 1σ confidence intervals at all redshifts.

In real clusters, baryons are distributed among stars and hot gas in the ICM whereas in adiabatic simulations are only found in the ICM. The estimation of the amount of baryons in hot gas phase requires high signal-to-noise ratios in the observations, which cannot be achieved for the total sample from most of the X-ray observatories.

Recently Giodini et al. (2009) provides a large and homogeneous set of data with stellar, gas and gravitating mass averaged over individual clusters

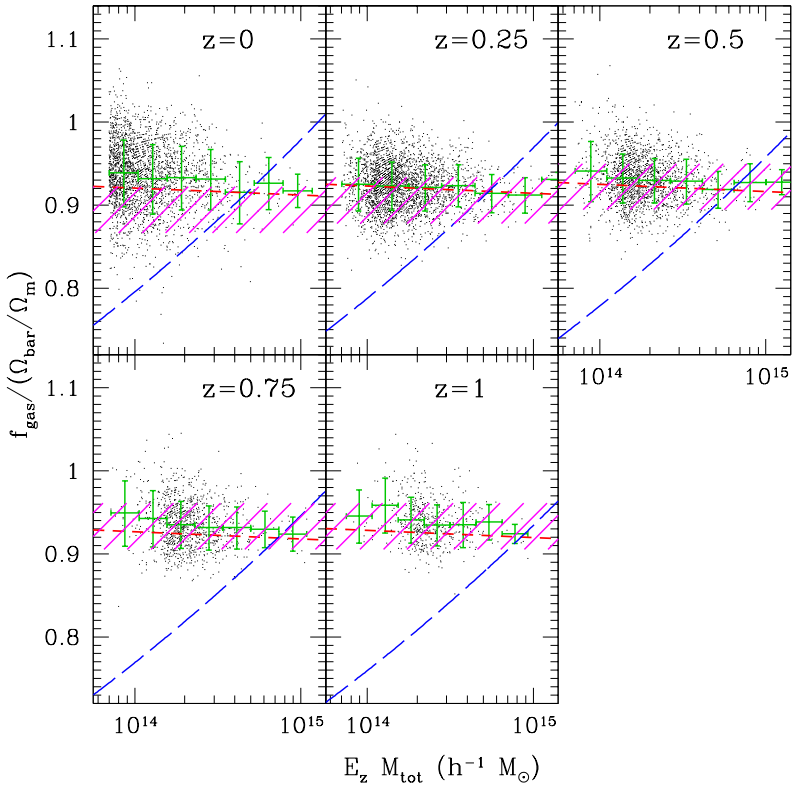

Figure 6.4: $f_{\rm gas} - E_z M_{\rm tot} - z$ relation and best-fit as seen on table 6.1 for $\Delta = 500c$. See text for a detailed overview on the observational data.

at redshifts $z \leq 1$ drawn from the *COSMOS 2 deg*^{2} survey, Vikhlinin et al. (2006), Arnaud et al. (2007) and Sun et al. (2009), under the assumption of $f_{\rm gas} - M_{\rm tot}$ independent of redshift. Their mean total baryon mass function $f_{500}^{stars+ICM}$ is represented in fig. 6.4 by a dotted blue line, adjusting their results the self-similar prediction with the appropriate E_z factors.

Clearly, adiabatic simulation does not bring a good representation since real clusters show lower $f_{\rm gas}$. The fact that the difference is more relevant for less massive clusters indicates that radiative processes deplete the inner regions of baryons and push them towards larger radii.

6.7 Discussion

Although scaling relations of local clusters are sensible to the thermodynamics to the ICM, numerous physical mechanisms can successfully reproduce these observations, at least on average. However, we would not expect the thermal history of the ICM to be the same in each case, so we should see differences in the evolutionary behavior. We have estimated the normalization, slope and evolution to quantify deviations from the self-similar model with unprecedent accuracy.

6.7.1 $E_z M_{\rm tot} - T_{\rm X} - z$

Seeking in the literature we may find that measuring these relations at high-redshift is considerably challenging. Despite the inherent difficulties in observing high-z objects, the measured evolution can be affected by poor statistics due to small sample sizes, the local scaling relation chosen to compare high-redshift data with, different definitions of evolution (as mentioned in section 6.1), whether the core is excised or not, inconsistent cluster selection, ...

As a consequence, no clear consensus on the the evolution of $M_{\rm tot} - T_{\rm X}$ has been found. Some authors studying a combination of low and high redshifts clusters have remarked that the evolution expected from self-similarity appears empirically justified with the appropriate E_z factors, e.g. Kotov & Vikhlinin (2005), Maughan et al. (2006), Vikhlinin et al. (2006). Other studies which include a large sample of clusters (Ettori et al. (2004b) and Mantz et al. (2009)) go even further adopting a model for evolution function of $z + 1$. They report $M_{\rm tot} - T_{\rm X}$ evolution consistent with the self-similar prediction within 1σ. In contrast, our evolution parameter indicates a slight positive evolution, $\gamma = 0.304 \pm 0.105$, 2.9σ above self-similar expectation.

Simulations that study the evolution of X-ray scaling relations are scarce. Ettori et al. (2004a) and Kay et al. (2007) use simulations with different prescription for cooling and stellar feedback and report negative evolution, between -0.12 and -0.20, with $\sim 2 - 5\sigma$.

The most complete papers on the issue are Rudd (2007) and Short et al. (2010) which compare adiabatic, preheating and radiative cooling evolution. In both works they study normalization and slope at each redshift independently, in contrast with our approach. Nevertheless we can check quantitatively our results.

In MUC we get a slope significantly larger than self-similar prediction ($\beta_{SS} = 1.5$) by 4.2σ. In comparison with the local scaling relations obtained in sections 3.4 and 4.1, the inclusion on high-z clusters makes the slope to be shallower. Rudd (2007) results of non-radiative run indicates slopes systematically higher than self-similar with weak tendency to be closer to self-similarity with redshift. Nevertheless, their results are with β_{SS} at all redshifts within $\sim 3{-}5\sigma$.

The same exercise is done by Kay et al. (2007) including radiative cooling and feedback in their simulations. With additional physics their mean slope (1.67) remains consistent with our results and remains constant up to $z \sim 0.5$.

The best-fit normalization, although fixed, is modified by the evolutionary term $\gamma \log(1+z)$ in eq 6.1. Our parameter $\gamma = 0.304 \pm 0.105$ perfectly agrees with the result 0.335 in the adiabatic run from Short et al. (2010)[2]. The resulting relation at $z = 1$ is $0.09\,dex$ higher than at $z = 0$, which also agrees remarkably with the $0.10\,dex$ change in the adiabatic WMAP3 run of Rudd (2007).

CLEF simulation (Kay et al. 2007) presents a very weak evolution in normalization $\gamma = 0.4$ In Short et al. (2010) simulations, preheated clusters normalization show the opposite tendency and becomes slightly negative, whether the feedback run indicates a positive evolution $\gamma = 0.249$ not far from our results.

We can thus conclude that the amount of evolution in normalization is regulated by the nature of the non-gravitational processes, whereas the slope seem to be unaffected.

6.7.2 $E_z M_{\rm tot} - E_z Y_{\rm X} - z$

Same as in the previous analysis, $M_{\rm tot} - Y_{\rm X}$ presents very similar results than $M_{\rm tot} - T_{\rm X}$. Studies with small samples of high-z clusters, i.e. Maughan et al. (2006), Maughan (2007), Maughan et al. (2008b), report that evolution is compatible with the self-similar model. The larger sample recently employed by Vikhlinin et al. (2009) also corroborates this result, reporting a $M_{\rm tot} - Y_{\rm X}$ slope of $beta = 0.57 \pm 0.05$.

In this work we have found a higher slope than the prediction from the self-similar model, $\beta = 0.6$, but yet significantly deviated with 5σ. This agrees with the adiabatic simulation performed by Rudd (2007), where they argue that this is due to the opposite sense of the $M_{\rm tot} - T_{\rm X}$ and $M_{gas} - T_{\rm X}$ relations.

[2]Their results have been rescaled to our definitions in eq. 6.1

Nevertheless, $M_{\rm tot} - Y_{\rm X}$ proves to be closer to self-similarity than $M_{\rm tot} - T_{\rm X}$. Besides, comparison with sections 3.4.1 and 4.2 indicate that slopes tend to shallow and normalizations increase when all-redshifts considered.

The normalization evaluated for MUC ($\gamma = 0.073 \pm 0.051$) evolves more softly than in similar adiabatic simulations of Rudd (2007) and Short et al. (2010), but still 1.4σ above the self-similar expectation. At $z = 1$ our normalizations is only $0.02\,dex$ higher than at $z = 0$ while in Rudd (2007) they find ~ 0.10, slightly lower than their $M_{\rm tot} - T_{\rm X}$ evolution. With respect to Short et al. (2010), they report $\gamma = 0.267 \pm 0.011$ in their gravitation-only run, $\gamma = 0.330 \pm 0.066$ with a preheating model and $\gamma = -0.054 \pm 0.014$ with feedback.

Apparent discrepancies with the adiabatic simulations can be explained by the larger differences that Rudd (2007) and Short et al. (2010) runs have with respect to the self-similar value. This deviations induce a larger apparent evolution in the normalization of scaling relations[3]. This discrepancy between our results and other authors can be resolved when more clusters will be detected at high-z. At the moment, from the largest detected cluster, at $z = 1$ in figure 6.2, it seems that the passive evolution from our model agrees with high-redshift $M_{\rm tot} - Y_{\rm X}$.

6.7.3 $E_z^{-1} L_{\rm X} - T_{\rm X} - z$

There are a number of observational works intended to the study of the $L_{\rm X} - T_{\rm X}$ at large distances. Unfortunately, the results from different studies appear contradictory due to selection biases and the analysis performed. As a consequence the evolution of this law is far from settled despite it is the most sensible to the astrophysical processes involved in cluster formation.

For instance, Ettori et al. (2004b) and Hilton et al. (2007) measure negative evolution. Another study performed by Maughan et al. (2006) who use a sample of 11 clusters in the range $0.6 < z < 1$ conclude that there is no evidence for any evolution beyond that anticipated from self-similar theory. Additionally, Kotov & Vikhlinin (2005), Kotov & Vikhlinin (2006) and Morandi et al. (2007) estimate relations at high-redshift that exhibit positive evolution.

Yet, an interesting description of the evolution is proposed by Voit (2005b) who suggest that self-similar evolution cannot persist to arbitrarily high redshift due to the increasing importance of radiative cooling and feedback from

[3]See appendix A from Short et al. (2010)

galaxy formation. This is observationally supported by Maughan et al. (2006) and Branchesi et al. (2007) which finds $L_X - T_X$ evolution is comparable to the self-similar prediction for $z < 0.3$, but negative at higher-z.

Coming back to our simulations, clearly MUC clusters lack the necessary physical processes to match real clusters. Anyhow we describe the results as in the more accurately reproduced scaling laws. In table 6.1 we find a scaling slope $\beta = 2.026 \pm 0.051$ slightly shallower than for nearby clusters alone (sections 3.4.1 and 6.5), but still compatible with them within the confidence intervals.

Normalization show a very large evolution ($\gamma = 1.261 \pm 0.108$) next to the gravitation-only run of Short et al. (2010), which show mild positive evolution ($\gamma = 0.307 \pm 0.058$). L_X is very sensitive to the additional physics and, as a consequence, the evolution is extremely sensitive to the detailed implementation. For instance, the preheating run of Short et al. (2010) estimates a very negative evolution inconsistent with observations while their simulation with feedback ($\gamma = 0.760 \pm 0.050$) is the model which better reproduce observational data. In opposition, another implementation of feedback (Kay et al. 2007) result into a negative parameter for evolution ($\gamma = -0.61 \pm 0.04$)

According to the enormously varied evolution of $L_X - T_X$, the conclusion is that it is unclear how the physical processes governing the ICM is actually affecting the evolution of galaxy clusters.

6.7.4 $f_{gas} - E_z M_{tot} - z$

It is sometimes assumed that f_{gas} is constant with redshift if clusters are selected appropriately (e.g. Rines et al. (1999), Allen et al. (2004)). Recent observational support this idea when intracluster light is taken into account in the baryon census (Gonzalez et al. 2007), however this work do not consider E_z that conceive the passive self-similar evolution. When passive self-similar evolution is assumed, the quiescent assumption often employed is transformed into a negative evolution as in fig. 6.4 where Giodini et al. (2009) data has lower normalization at high-z.

Simulations disagree on the evolution of the baryon fraction. Some authors claim that there is a negative evolution (e.g. Ettori et al. (2004a), Kay et al. (2007)) while others find no evolution (Crain et al. 2007) at all.

In this work we have found a positive evolution on top of the passive one ($\gamma = 0.012 \pm 0.006$). As a comparison we measure a very weak variation

$f_{\rm gas}/(\Omega_{\rm bar}/\Omega_{\rm m}) = 0.919$ at $z = 0$ and $f_{\rm gas}/(\Omega_{\rm bar}/\Omega_{\rm m}) = 0.928$ at $z = 1$ for a $M_{\rm tot} = 3 \times 10^{14}\, h^{-1} M_{\odot}$, whereas Ettori et al. (2009) report $f_{\rm gas}/(\Omega_{\rm bar}/\Omega_{\rm m}) = 0.874$ at $z = 0$ and $f_{\rm gas}/(\Omega_{\rm bar}/\Omega_{\rm m}) = 0.947$ at $z = 1$ with gravitational heating only.

Recently, Young et al. (2010) have reported results from MGS simulations that agree with our results in the self-similar expectation within r_{500} for adiabatic clusters. They also see a very slight increase in baryon fraction at larger distances, $f_{\rm gas}/(\Omega_{\rm bar}/\Omega_{\rm m}) \simeq 0.894$ at $z = 0$ and $f_{\rm gas}/(\Omega_{\rm bar}/\Omega_{\rm m}) \simeq 0.933$ at $z = 1$.

The main difference between Ettori et al. (2009) and Young et al. (2010) simulations and our work is the enhanced resolution of MUC, that tend to indicate a higher baryon fraction at lower redshifts and a weaker evolution.

Chapter 7

Conclusions

> An ancestor of mine maintained, that if you eliminate the impossible, whatever remains, however improbable, must be the truth.
>
> *Star Trek VI: The Undiscovered Country*, Mr. Spock

In this thesis we have described a study of galaxy clusters by means of the high-resolution adiabatic simulations in the MNCP. This set is formed by five simulations at different resolutions, cosmological parameters and initial random phases. The cosmological frameworks cover the most probable models compatible with the constrains derived from CMB, supernovae and galaxy clusters observations. However, the most important feature is the fact that it contains the MUC simulation, the largest SPH simulations ever carried out.

We use this simulated clusters to explore the distribution of properties in the ICM, including total mass, gas mass, X-ray temperature, SZ proxy, luminosity and baryon fraction; measured within $\Delta = 500c$ and $\Delta = 200$ at several snapshots between $z = 0$ and $z = 1$. We have analyzed the effects of resolution in the X-ray scaling relations ($M_{\rm tot} - T_{\rm X}$, $M_{\rm tot} - Y_{\rm X}$, $L_{\rm X} - T_{\rm X}$ and $f_{\rm gas} - M_{\rm tot}$), the abundances of galaxy clusters for WMAP1 to WMAP5 models and the evolution of scaling relations in the WMAP1 universe. Moreover, thanks to the unprecedent resolution in our largest sample we have been able to measure the scatter in the scaling relations. Our main results are summarized as follows:

- Dynamical state of galaxy clusters has no influence in the determination of the scaling relations as indicated in table 3.4.1. Numerical predictions

of other authors (e.g. Jeltema et al. (2008)) with simulations including radiative processes support this argument.

- From the analysis of scaling relations at $z = 0$ we conclude that our simulations have enough resolution to reproduce the observed $M_{\rm tot} - T_{\rm X}$ and $M_{\rm tot} - Y_{\rm X}$ relations. In the former, the systematics produced by increasing resolution from 512^3 to 1024^3 are comparable to the instrumental uncertainties. The latter shows even a better agreement proving that $M_{\rm tot} - Y_{\rm X}$ is less dependent on resolution and, hence, more suitable for the numerical study of cluster $M_{\rm tot}$.

- Our $L_{\rm X} - T_{\rm X}$ and $f_{\rm gas} - M_{\rm tot}$ relations fail to mimic the latests observations of $L_{\rm X}$ and $f_{\rm gas}$. Since resolution does not play a significant role, these systematic differences must come from lack of the necessary physical processes even in the region $r > 0.15\, r_{500}$. In fact, we can state that low-$M_{\rm tot}$ clusters are more affected by radiative physics.

- Underesolved halos can be easily found when it comes to $f_{\rm gas}$. Smaller halos tend to have lower $M_{\rm gas}$ which makes $f_{\rm gas}$ closer to the observational expectations. However, this is just an spurious result driven by the lack of particles in such halos. We have found the same decline in works from other authors (i.e. Rudd (2007) and Crain et al. (2007)) when dark matter halos has approximately the same number of particles as in our simulations (see fig. 3.7).

- We have fully characterized the residuals of the best-fit scaling relations at $z = 0$ in three cosmological models based on WMAP results. This includes intrinsic scatter, skewness and kurtosis of both X-ray properties. In this work, the sources of the intrinsic scatter are history of formation of clusters and the dynamical state, although merging does not seem to play a role according to Yang et al. (2009). Besides, we model the residuals as a function of a fixed X-ray property.

- By comparing the results from MUC and MUCL we get an estimate of the uncertainties due to numerical resolution. This allow us to state that numerical convergence of scaling relations is reached before the scatter does. In general, higher resolution simulation presents larger scatter whereas lower σ_8 cosmologies tend to decrease it. Numerical uncertainties are of the same order than variations between cosmological models, with the exception of $L_{\rm X} - T_{\rm X}$ which is more dependent of resolution.

- $M_{\rm tot} - Y_{\rm X}$ happens to be not only a low-scatter scaling relation, as proved observationally by Vikhlinin et al. (2009). Besides, it is more robust than

the other relations in terms of numerical study because the scatter seems almost unaffected by resolution. In addition, Nagai (2006) reports that it is also fairly unaffected by radiative cooling, star formation and energy feedback. All together, and thanks to the large quantity of clusters in our samples, makes that our computation of $M_{\rm tot} - Y_{\rm X}$ scatter the most accurate estimate up-to-date.

- The comparison between our numerical XTF and the most recent observations (Ikebe et al. (2002), Henry (2004b)) shows a deficient of abundance of cluster in WMAP3. The needed $M_{\rm tot} - T_{\rm X}$ relation to reconcile mass and X-ray luminosity functions are $\sim 5\sigma$ away from the relation we get from simulations MUW+MU2W.

- Increasing σ_8 value, as in simulation MUWHS, partially alleviates the problem although the cluster abundance still lies below the observational estimates. Very recently, the joint analysis of WMAP5 and *maxBCG* cluster catalog has proved that $\sigma_8 \sim 0.8$ (Rozo et al. 2010).

- Thanks to the high resolution of simulation MUC, the number of cluster at high redshift is large enough to study the evolution of the scaling relations for $z < 1$. $E_z M_{\rm tot} - T_{\rm X} - z$ is bias high at all redshifts when we compare with observations. However, the observational mass estimates are known to be underestimated by 20% when $M_{\rm tot}$ is computed assuming hydrostatic equilibrium (i.e., Rasia et al. (2006), Nagai et al. (2007b), Jeltema et al. (2008)). The mismatch between MUC clusters and the latest observational results is compatible with those $\sim 20\%$ systematics.

- We find a positive evolution in $E_z M_{\rm tot} - T_{\rm X} - z$ that agrees remarkably with similar non-radiative simulations from Rudd (2007) and Short et al. (2010). Simulations including preheating or feedback results into an amount of evolution that depends on the detailed prescription of the radiative processes added.

- The evolution in $E_z M_{\rm tot} - E_z Y_{\rm X} - z$ is significantly more quiescent in this work than in the adiabatic runs of Rudd (2007) and Short et al. (2010). Basing in the discussion of appendix A of Short et al. (2010), we believe their increase of evolution is only apparent and is due to the larger deviation from self-similarity they present. Our sample, on the other hand, show a smaller deviation from the self-similar prediction and does not suffer from this mock evolution. Anyhow, and despite the short of observations to compare with, our model agrees remarkably with most distant observed cluster (Maughan et al. 2008b).

- As expected from the previous chapters, the $E_z^{-1}L_X - T_X - z$ relation fails to reproduce observations at $z > 0$, obtaining only similar results in very massive systems ($M_{tot} \sim 10^{15}h^{-1}M_\odot$). A large range of evolution parameters can be obtained depending on the detailed prescription of physical processes. Anyhow, the $E_z^{-1}L_X - T_X - z$ evolution that we measure is much larger than both, any of them and the observational data.

- Baryon fraction is also unable to reproduce observations, however, we get similar results in evolution of real clusters. We report that $f_{gas} - E_z M_{tot} - z$ has a very weak positive evolution on top of the self-similar one whereas observations tend to indicate no evolution at all.

Resolution, cosmological framework and scaling relations are the foundations of the scatter measurement. Lack of resolution in sampling clusters profiles adds up scatter to the scaling relations. This must be taken into account in theoretical predictions because in some cases it may exceed the underlying meaningful scatter. For instance, we have seen that $L_X - T_X$ intrinsic scatter is very sensitive to resolution changes even for the highly resolved clusters.

In the last years, the efforts of the scientific society have focused in performing highly detailed numerical simulations in order to understand all the physical processes involved in the formation of a galaxy cluster. The drawback is that the number of objects studied is very small.

This thesis is based on the contrary approach, where a large statistical sample of clusters is needed to study large-scale structure. By removing radiative processes from the numerical code, we can simulate high-resolution clusters in large volumes. This work allow to examine clusters that have had different formation histories which causes the intrinsic scatter in the scaling relation. In the next years, forthcoming projects will survey larger volumes and SZ detection will allow to observations at high-z. Theoretical studies of scatter in scaling relations are compulsory to determine the uncertainties in their mass estimates.

7.1 Future prospects

Significant applications can also be found for our databases. In particular, we have restricted our analysis to galaxy clusters whereas the modeling of gas outside collapsed objects is remarkable in our simulations.

For instance, MUC has larger volume and higher resolution than the most of numerical simulations devoted to the study of the baryon budget (e.g. Davé et al. (2001), Cen & Ostriker (2006), Harford et al. (2008), Smith et al. (2010)). These previous works state that the evolution of WHIM is primary determined by shock heating from gravitational perturbations whereas radiative cooling and feedback plays a much lesser role. What is more, box size is a crucial parameter because larger scales that affect in the non-linear evolution of WHIM are considered (Davé et al. 2001). Only galactic superwinds has a significant impact in the baryon budget (see figure 2.4) as it is reported in Cen & Ostriker (2006). However, the generation of galactic superwinds is far from being properly modeled.

Coming back to galaxy clusters,we may be able to check for the existence of a fundamental plane for galaxy clusters using their SZ signal. Verde et al. (2002) and Afshordi (2008) establish semi-analytical models that relates the SZ flux, the angular size and the temperature (SZ flux, observed size and total mass $M_{\rm tot}$ in Afshordi (2008)) of clusters, similar to the Tully-Fisher relation for spiral galaxies. The use of the latter relationship can be seen as a new method to estimate cluster masses from SZ measurements. Needless to say, the fundamental plane can only be accurately modeled through high-resolution cosmological simulations with a sufficiently large number of clusters to perform a three-dimensional fitting, such as the MUC clusters that we have introduced in this thesis.

Finally, the creation of samples with equal number of particles would guarantee the lack of resolution effects. The ideal simulation a larger volume to increase the mass coverage, specially in the high-mass regime. This can be achieved by performing a preliminary simulation in the full volume, where low-resolution clusters are identified. Afterwards, mass-selected clusters would be resimulated keeping each halo with an equal number of particles. In this way, volume-limited samples can be obtained while the ICM structure is equally described for the total mass range.

Such a sample would allow to analyze the shape of the scaling laws. Scaling relations follow simple power-laws according to the self-similar model. Despite the agreement of observations is remarkable, simple theoretical models predict small deviations from linearity. An sample of equally-resolved clusters would be the perfect tool to investigate into non-linear scaling relations.

Conclusiones

> Uno de mis antepasados sostenía, que si se eliminaba lo imposible, lo que quedase, por improbable que fuera, sería la verdad.
>
> *Star Trek VI: Aquel país desconocido*, Sr. Spock

En esta tesis hemos descrito el estudio de los cúmulos de galaxias por medio de las simulaciones adiabáticas de alta resolución de MNCP. El conjunto está formado por cinco simulaciones de distinta resolución y parámetros cosmológicos. Los entornos cosmológicos utilizados cubren los modelos más probables compatibles con las restricciones provenientes de las observaciones de CMB, supernovas y cúmulos de galaxias. Sin embargo, lo más importante es que este conjunto contiene a la simulación MUC, la mayor simulación SPH realizada hasta el momento.

Utilizamos los cúmulos simulados para explorar las propiedades en rayos X del ICM: masa total, masa de gas, temperatura en rayos X, indicador SZ, luminosidad y fracción bariónica; medidas a $\Delta = 500c$ y $\Delta = 200$ en distintos instantes entre $z = 0$ y $z = 1$. Se han analizado los efectos de la resolución en las relaciones de escala de rayos X ($M_{\rm tot} - T_{\rm X}$, $M_{\rm tot} - Y_{\rm X}$, $L_{\rm X} - T_{\rm X}$ y $f_{\rm gas} - M_{\rm tot}$), así como las abundancias de cúmulos de galaxias para modelos WMAP1 y WMAP5 y la evolución de dichas relaciones de escala en el universo WMAP1. Además, gracias a la resolución sin precedentes de nuestra muestra más grande, hemos podido medir la dispersión de las relaciones de escala. Los resultados más importantes se resumen a continuación:

- El estado dinámico de los cúmulos de galaxias no tienen influencia en la determinación de las relaciones de escala tal y como se indica en la tabla 3.4.1. Las predicciones numéricas de otros autores (e.g. Jeltema et al. (2008)) con simulaciones que incluyen procesos radiativos apoyan este argumento.

- A partir del análisis de las relaciones de escala a $z = 0$ concluímos que nuestras simulaciones tienen suficiente resolución para reproducir las relaciones $M_{\rm tot} - T_{\rm X}$ y $M_{\rm tot} - Y_{\rm X}$ observadas. En la primera, los errores sistemáticos producidos por aumentar la resolución de 512^3 a 1024^3 son comparables a las incertidumbres instrumentales. En cuanto a $M_{\rm tot} - Y_{\rm X}$, incluso un mejor acuerdo demostrando que es menos dependiente de la resolución y, por tanto, más apropiada para es estudio numérico de la masa total de los cúmulos.

- Nuestras relaciones $L_{\rm X} - T_{\rm X}$ y $f_{\rm gas} - M_{\rm tot}$ no son capaces de reproducir las observaciones de luminosidad y fracción bariónica. Ya que la resolución no juega un papel importante, estas diferencias sistemáticas deben provenir de la falta de los procesos físicos necesarios incluso en la región $r > 0.15\, r_{500}$. De hecho, los cúmulos de menor masa están más afectados por la física radiativa.

- Viendo la fracción bariónica se pueden encontrar fácilmente los halos no resueltos. Los halos pequeños tienden a tener menor $M_{\rm gas}$ lo que hace que su $f_{\rm gas}$ disminuya y se aproxime a valores observacionales. Sin embargo, este es únicamente un resultado espúreo debido a la falta de partículas en esos halos. Hemos encontrado la misma disminución en trabajos de otros autores (i.e. Rudd (2007) and Crain et al. (2007)) para los halos de materia oscura con aproximadamente el mismo número de partículas que en nuestras simulaciones (ver fig. 3.7).

- Hemos caracterizado completamente los residuos de las relaciones de escala que mejor se ajustan, a $z = 0$ y en tres modelos cosmológicos basados en resultados de WMAP. Esto incluye la dispersión intrínseca, asimetría y curtosis en los dos ejes. En este trabajo, la fuentes de dispersión intrínseco son la historia de formación de los cúmulos y el estado dinámico, aunque la fusión de objetos no parece tener importancia de acuerdo a Yang et al. (2009).

- Comparando los resultados de MUC y MUCL obtenemos una estimación de las incertidumbres debidas exclusivamente a la resolución numérica. Esto nos permite determinar que la convergencia numérica se alcanza antes para las relaciones de escala medias que para la dispersión. En general, la simulación con mayor resolución presenta mayor dispersión mientras que las cosmologías con menor σ_8 tienden a disminuirla. Las incertidumbres numéricas son del mismo orden que las variaciones debidas a los modelos cosmológicos, con la excepción de $L_{\rm X} - T_{\rm X}$ que es más dependiente de la resolución.

- $M_{\rm tot} - Y_{\rm X}$ resulta no ser únicamente una relación de escala con poca dispersión, como demostró observacionalmente Vikhlinin et al. (2009). También es más robusta que las demás relaciones en términos numéricos porque su dispersión no está casi afectado por la resolución. Además, Nagai (2006) informa que es muy poco dependiente del enfriamiento radiativo, la formación estelar y la retroalimentación energética. Todo esto, junto con la gran cantidad de cúmulos de nuestras muestras, hace que nuestro cálculo sobre la dispersión de $M_{\rm tot} - Y_{\rm X}$ sea la estimación más precisa hasta la fecha.

- La comparación de nuestras XTF numéricas con las más recientes observaciones (Ikebe et al. (2002), Henry (2004b)) indica una deficiencia en las abundancias en cúmulos en WMAP3. La relación $M_{\rm tot} - T_{\rm X}$ necesaria para reconciliar las funciones de masa y luminosidad en rayos X están alejadas $\sim 5\sigma$ de las relaciones que obtenemos en las simulaciones WMAP3.

- Aumentando el valor de σ_8, como en la simulación MUWHS, palia parcialmente el problema aunque la abundancia de cúmulos aún se mantiene por debajo de las estimaciones observacionales. Muy recientemente, el análisis conjunto de WMAP5 y el catálogo de cúmulos *maxBCG* ha demostrado que $\sigma_8 \sim 0.8$ (Rozo et al. 2010).

- Gracias a la alta resolución de la simulación MUC, el número de cúmulos a alto redshift es suficientemente grande como para estudiar la evolución de las relaciones de escala en $z < 1$. Al comparar con las observaciones vemos que nuestra $E_z M_{\rm tot} - T_{\rm X} - z$ es sistemáticamente mayor en todos los redshifts. Sin embargo, se sabe que las estimaciones observacionales de la masa están subestimadas un 20% al asumir equilibrio hidrostático para calcular $M_{\rm tot}$(i.e., Rasia et al. (2006), Nagai et al. (2007b), Jeltema et al. (2008)). El desajuste entre los cúmulos MUC y los recientes observaciones es compatible con estos errores sistemáticos del $\sim 20\%$.

- Encontramos una evolución positiva en $E_z M_{\rm tot} - T_{\rm X} - z$ que presenta un acuerdo notable con simulaciones no radiativas de Rudd (2007) y Short et al. (2010) que son similares a las nuestras. En simulaciones que incluyen precalentamiento o retroalimentación energética la evolución depende de la forma concreta en que se implementan esos procesos radiativos adicionales.

- La evolución en $E_z M_{\rm tot} - E_z Y_{\rm X} - z$ es significativamente más próxima a la evolución pasiva auto-similar en este trabajo que en las simulaciones

adiabáticas de Rudd (2007) y Short et al. (2010). Basándonos en la discusión del apéndice A de Short et al. (2010), creemos que su mayor evolución es sólo aparente y se debe a la mayor desviación que presentan respecto al modelo auto-similar. Nuestra muestra, por otro lado, es más próxima a la predicción auto-similar y no sufre tanto la evolución espúrea. De cualquier modo, y a pesar de las pocas observaciones con las que comparar, nuestro modelo coincide perfectamente con el cúmulo observado más distante (Maughan et al. 2008b).

- Tal y como era de esperar por los capítulos anteriores, la relacin $E_z^{-1}L_{\rm X} - T_{\rm X} - z$ no es capaz de reproducir las observaciones a $z > 0$, obteniendo resultados similares únicamente para en los objetos muy masivos ($M_{\rm tot} \sim 10^{15}h^{-1}M_{\odot}$). Dependiendo de cómo se implementen los procesos físicos se puede obtener un amplio rango de resultados para la evolución. De todas formas, la evolución $E_z^{-1}L_{\rm X} - T_{\rm X} - z$ que medimos es mucho mayor que las estimadas anteriormente, ya sean con simulaciones o con cúmulos observados.

- La fracción bariónica tampoco es capaz de reproducir las observaciones, sin embargo, obtenemos resultados similares a la evolución de cúmulos reales. Encontramos que $f_{\rm gas} - E_z M_{\rm tot} - z$ tienen una evolución positiva débil más allá de la auto-similar mientras que las observaciones tienden a indicar que no hay evolución en absoluto.

La resolución, el entorno cosmológico y las relaciones de escala son los cimientos de la medida de la dispersión. La falta de resolución a la hora de muestrear los perfiles de los cúmulos añaden aún más dispersión a las relaciones de escala. Esto se debe tener en cuenta en las predicciones teóricas porque, en algunos casos, puede incluso exceder la dispersión subyacente que sí tiene sentido físico. Por ejemplo, hemos visto que la dispersión intrínseca de $L_{\rm X} - T_{\rm X}$ es muy sensible a los cambios en la resolución incluso para los cúmulos mejor resueltos.

En los últimos años, los esfuerzos de la comunidad científica se han centrado en realizar simulaciones numéricas muy detalladas para entender los procesos físicos involucrados en la formación de un cúmulo de galaxias. La desventaja es que el número de objetos estudiados es muy bajo.

En esta tesis nos hemos basado en el enfoque contrario, en el que empleamos una gran muestra estadística para estudiar la estructura a gran escala. Quitando los procesos radiativos del código numérico, podemos simular cúmulos en alta resolución en grandes volúmenes. Este trabajo permite examinar los

cúmulos que han tenido distintas historias de formación, por lo que las relaciones de escala tienen una dispersión intrínseca. En los próximos años, la nueva generación de proyectos sondearán volúmenes más extensos y detectarán cúmulos por efecto SZ lo que permitirá que haya más observaciones a alto-z. Los estudios teóricos de la dispersión en las relaciones de escala son imprescindibles para determinar las incertidumbres de las masas en observaciones futuras.

Appendix A

Derivation of the Self-Similar Scaling Relations

A.1 Mass vs Temperature Relation

The equation of hydrostatic equilibrium can be written as,

$$\frac{d(\rho_{\rm gas} T)}{dr} \approx \frac{\rho_{\rm gas} G M_{\rm tot}}{r^2} \Rightarrow M_{\rm tot} \propto TR \tag{A.1}$$

and the total mass of a sphere of radius R with density Δ times bigger than the critical density is,

$$M_{\rm tot} \equiv \frac{4}{3}\pi\, \rho_{\rm crit,z}\, \Delta R^3 \tag{A.2}$$

which, according with equations 1.6 and 1.10, can be rewritten as

$$M_{\rm tot} \propto E_z^2 \Delta R^3 \tag{A.3}$$

Combining equations A.1 and A.3 the mass versus temperature relations is got,

$$\boxed{E_z\, M_{\rm tot} \propto T^{3/2}} \tag{A.4}$$

A.2 Baryon Fraction vs Temperature/Mass Relation

Taking the state equation of an ideal gas,

$$P = \frac{\rho_{\rm gas} k_B T}{\mu m_p} = P_0 \rho_{\rm gas}^{\gamma} \tag{A.5}$$

and assuming and isothermal gas ($\gamma = 1$), density becomes independent from temperature

$$\rho_{\rm gas} \propto T^0 \tag{A.6}$$

According to A.1 and the previously derived relation $M_{\rm tot} - T_{\rm X}$, total density may be written as

$$\rho \propto \frac{M_{\rm tot}}{R^3} \propto \frac{T^3}{M_{\rm tot}^2} \propto T^0 \tag{A.7}$$

Hence, the baryon fraction is

$$f_{\rm gas} \equiv \frac{\rho_{\rm gas}}{\rho} = \frac{M_{gas}}{\frac{4}{3}\pi R^3} \frac{\frac{4}{3}\pi R^3}{M_{\rm tot}} = \frac{M_{gas}}{M_{\rm tot}} \propto T^0 \Rightarrow f_{\rm gas} \propto T^0 \tag{A.8}$$

And together with the previously-deduced $M_{\rm tot} - T_{\rm X}$relation

$$\boxed{f_{\rm gas} \propto M_{\rm tot}^0} \tag{A.9}$$

A.3 Luminosity vs Temperature/Mass Relation

In the absence of star formation, the total emissivity of a hot plasma is simply derived from the gas density and a function depending of its temperature

$$\epsilon = n_e n_H \Lambda(T) \propto \rho_{\rm gas}^2 \Lambda(T) \tag{A.10}$$

being $\Lambda(T)$ the bolometric cooling function (see section 3.3.2). Hence, total luminosity can expressed as

$$L_{\rm X} \propto \epsilon R^3 \approx \rho_{\rm gas}^2 T^{1/2} R^3 \propto \frac{f_{\rm gas}^2 T^{1/2} M_{\rm tot}^2}{R^3} \propto f_{\rm gas}^2 T^{1/2} M_{\rm tot} E_z^2 \tag{A.11}$$

Using equations A.4 and A.8 we may approximate the relations as

$$\boxed{E_z^{-1} L_{\rm X} \propto T^2} \tag{A.12}$$

and

$$E_z^{-1} L_{\rm X} \propto (E_z M_{\rm tot})^{4/3} \tag{A.13}$$

A.4 Mass vs $Y_{\rm X}$ Relation

According to Kravtsov et al. (2006), the product of gas mass and temperature is an observational proxy for the total SZ flux created by hot ICM in a cluster.

$$E_z Y_{\rm X} = E_z M_{\rm gas} T \tag{A.14}$$

In eq A.8 we saw that baryon fraction is independent of temperature, and together with eq A.4 we may rewrite $Y_{\rm X}$ as

$$E_z Y_{\rm X} \propto E_z M_{\rm tot} T \propto (E_z M_{\rm tot})^{5/3} \tag{A.15}$$

Resulting in the self-similar prediction for the $M_{\rm tot} - Y_{\rm X}$ relation,

$$\boxed{E_z M_{\rm tot} \propto (E_z Y_{\rm X})^{3/5}} \tag{A.16}$$

Appendix B

Intrinsic Scatter

B.1 $M_{\rm tot} - T_{\rm X}$ relation

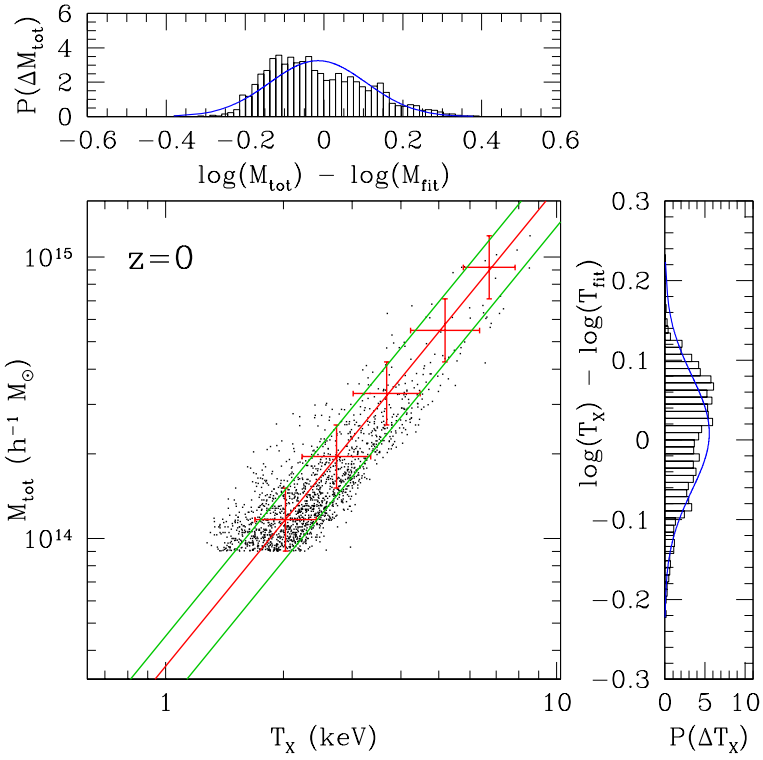

Figure B.1: Same as figure 4.1 for simulation MUCL.

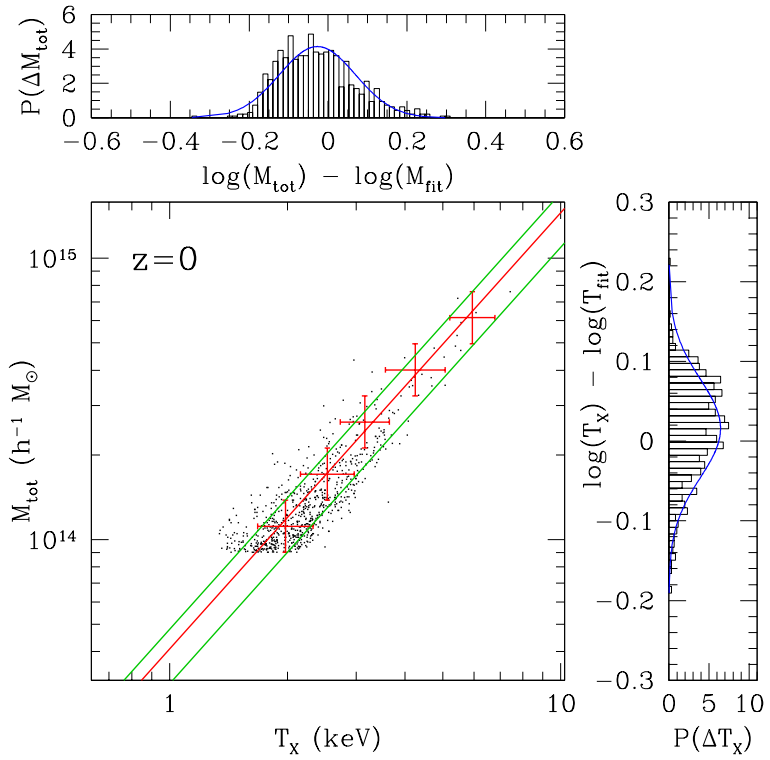

Figure B.2: Same as figure 4.1 for simulation MUW+MU2W.

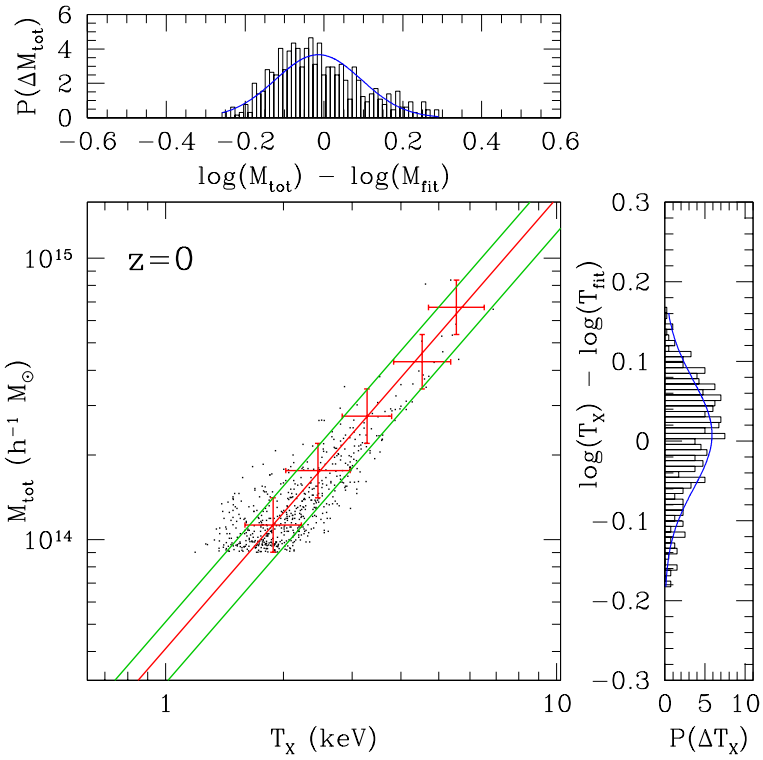

Figure B.3: Same as figure 4.1 for simulation MUWHS.

B.2 $M_{\rm tot} - Y_{\rm X}$ relation

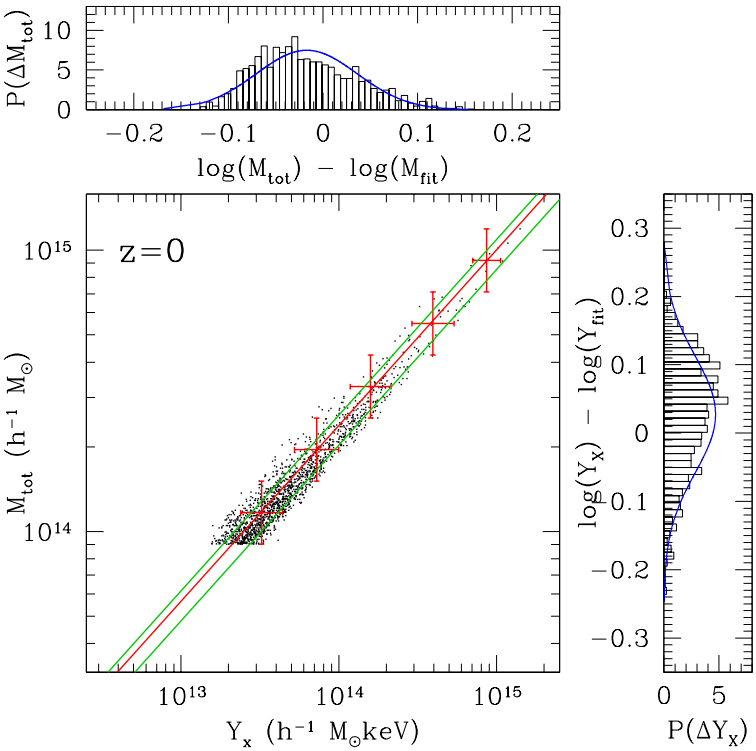

Figure B.4: Same as figure 4.3 for simulation MUCL.

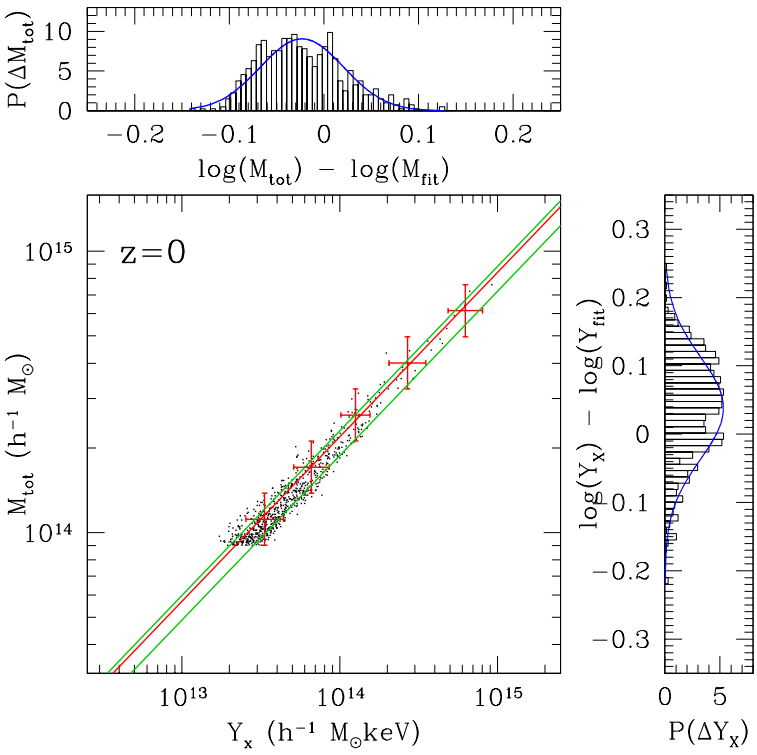

Figure B.5: Same as figure 4.3 for simulation MUW+MU2W.

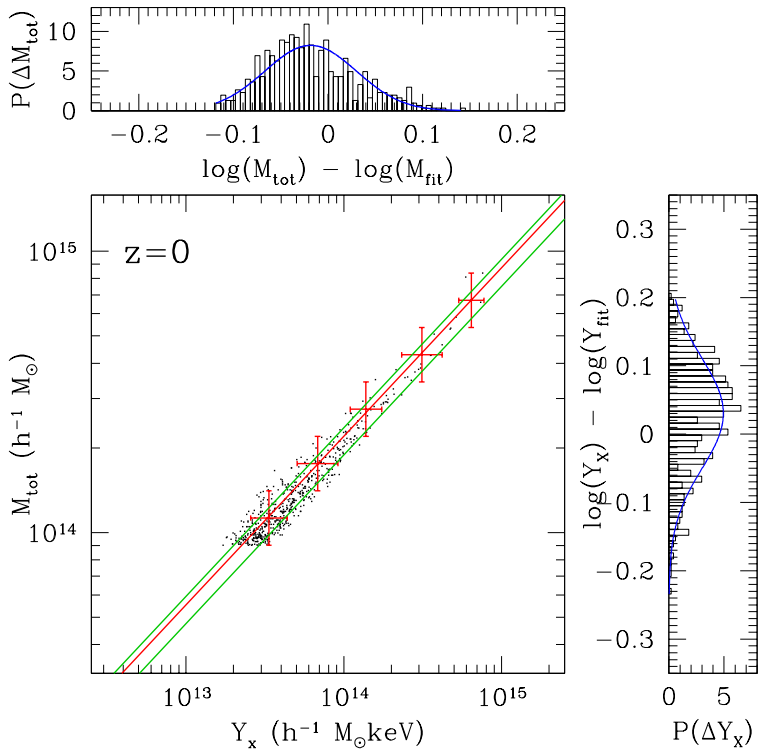

Figure B.6: Same as figure 4.3 for simulation MUWHS.

B.3 $L_{\rm X} - T_{\rm X}$ relation

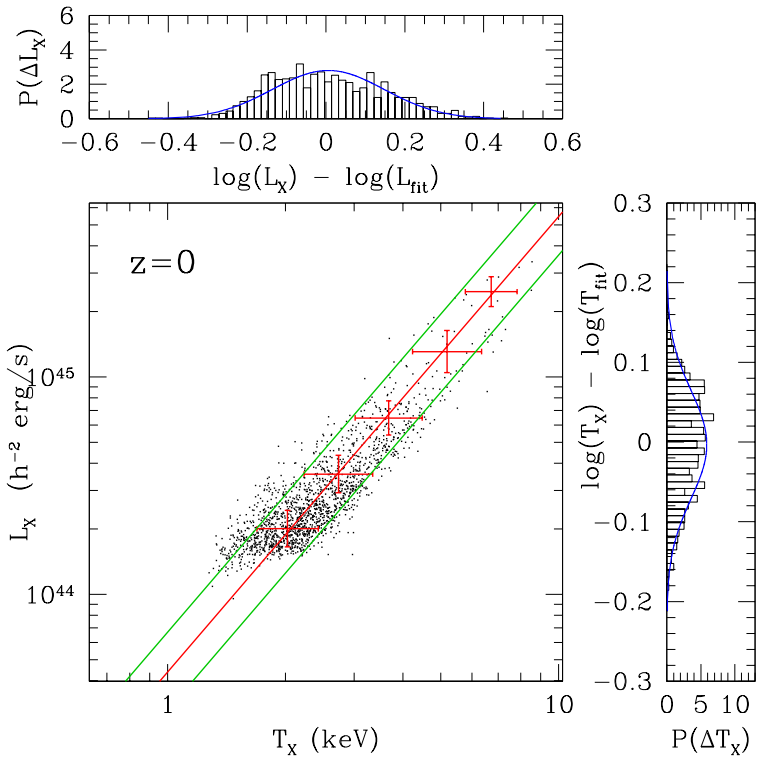

Figure B.7: Same as figure 4.5 for simulation MUCL.

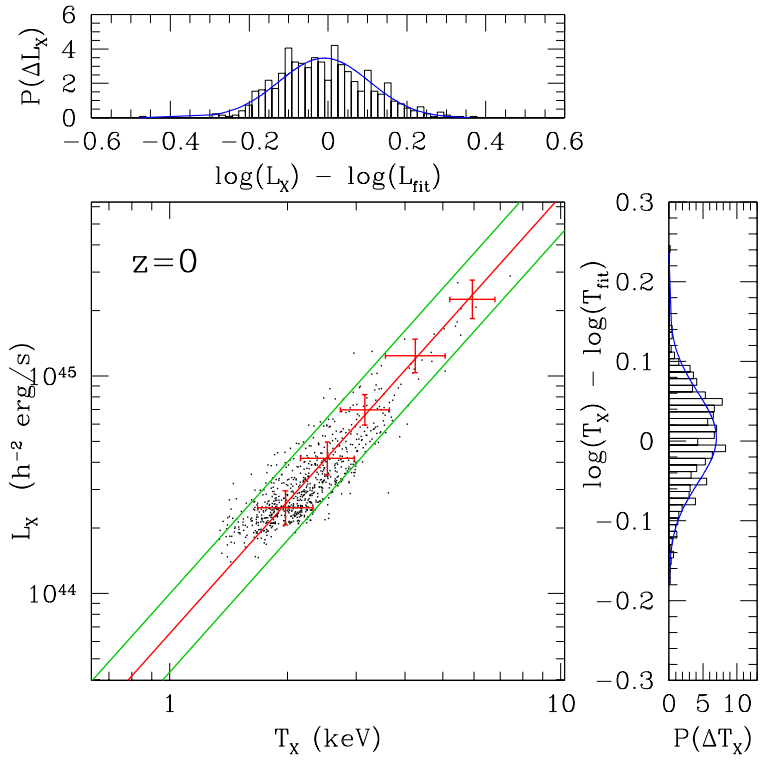

Figure B.8: Same as figure 4.1 for simulation MUW+MU2W.

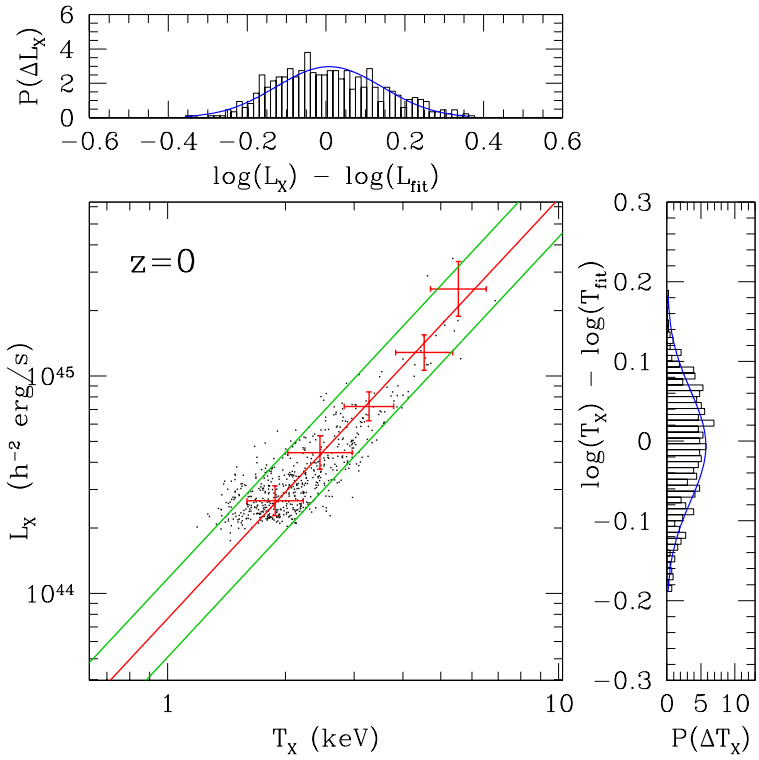

Figure B.9: Same as figure 4.5 for simulation MUWHS.

B.4 $f_{\rm gas} - M_{\rm tot}$ relation

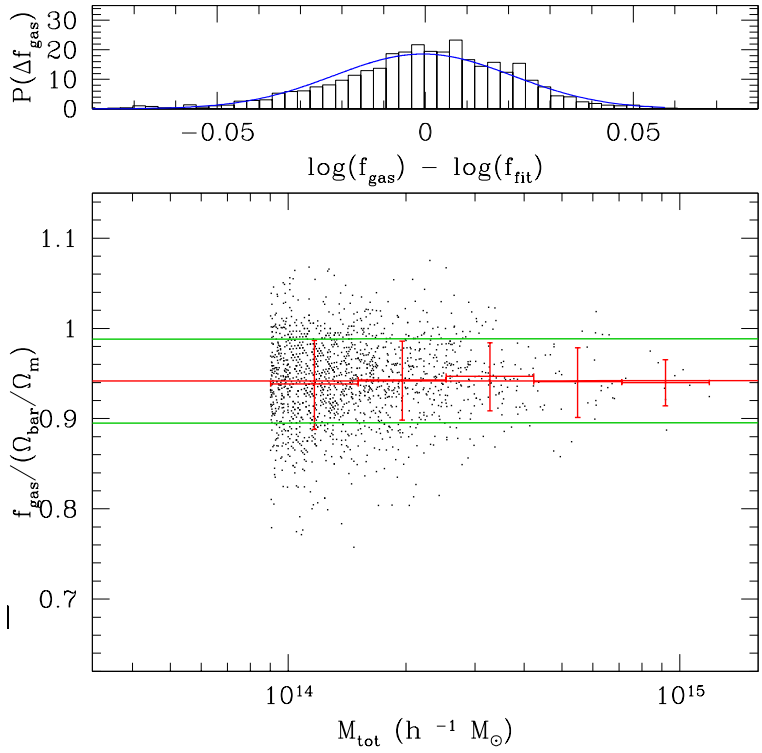

Figure B.10: Same as figure 4.7 for simulation MUCL.

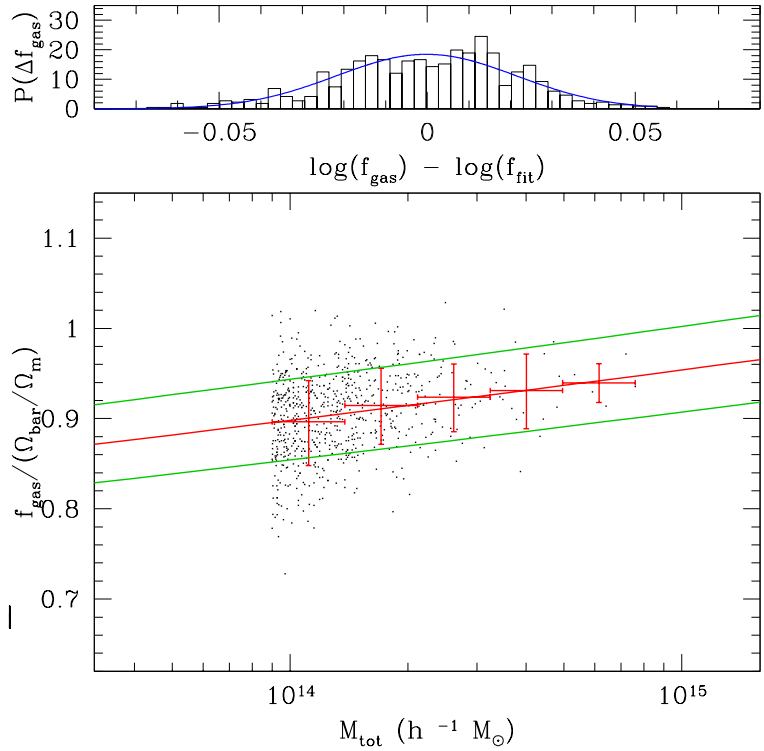

Figure B.11: Same as figure 4.7 for simulation MUW+MU2W.

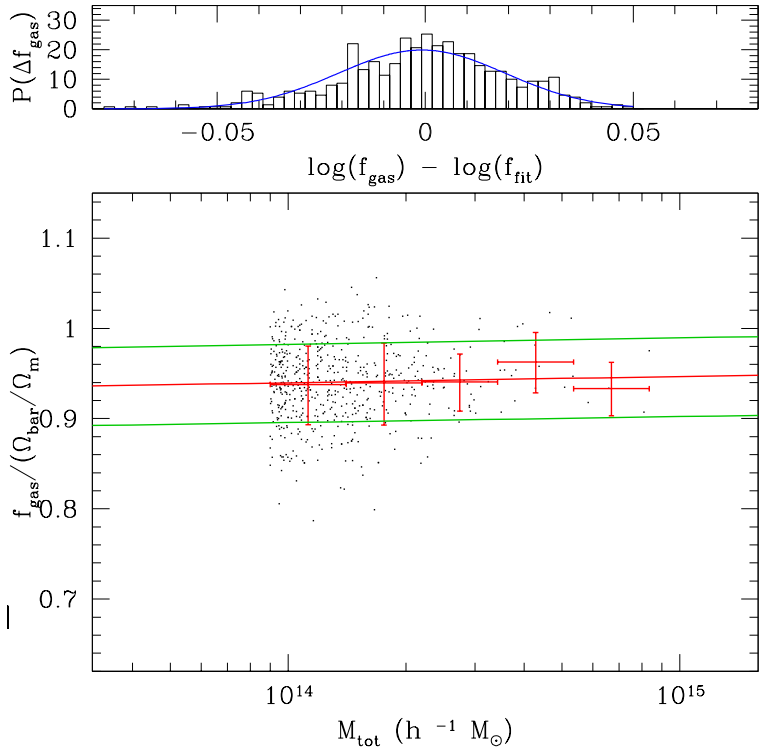

Figure B.12: Same as figure 4.7 for simulation MUWHS.

Appendix C

Scatter residuals

C.1 $M_{\rm tot} - T_{\rm X}$ relation

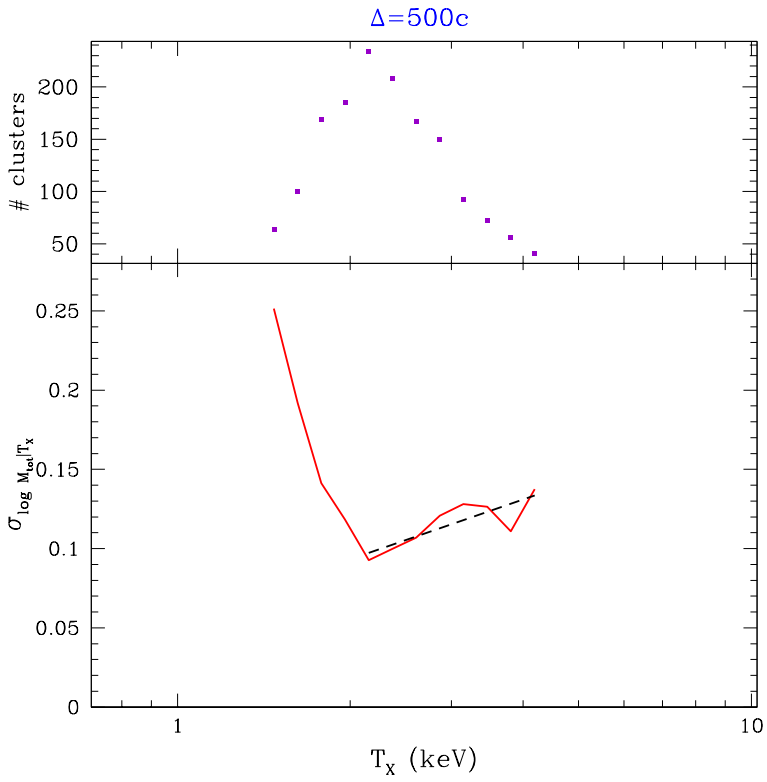

Figure C.1: Same as figure 4.2 for simulation MUCL.

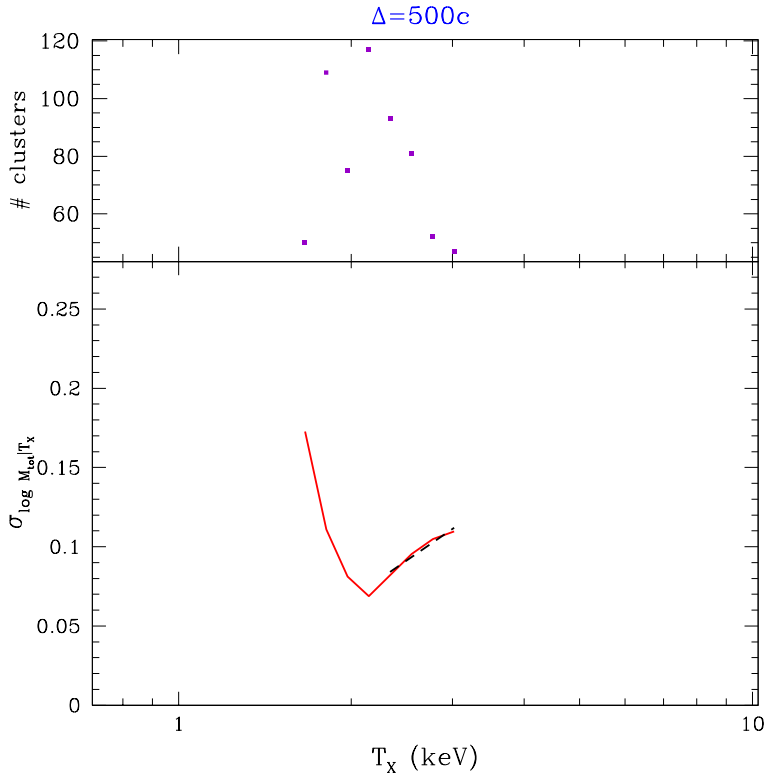

Figure C.2: Same as figure 4.2 for simulation MUW+MU2W.

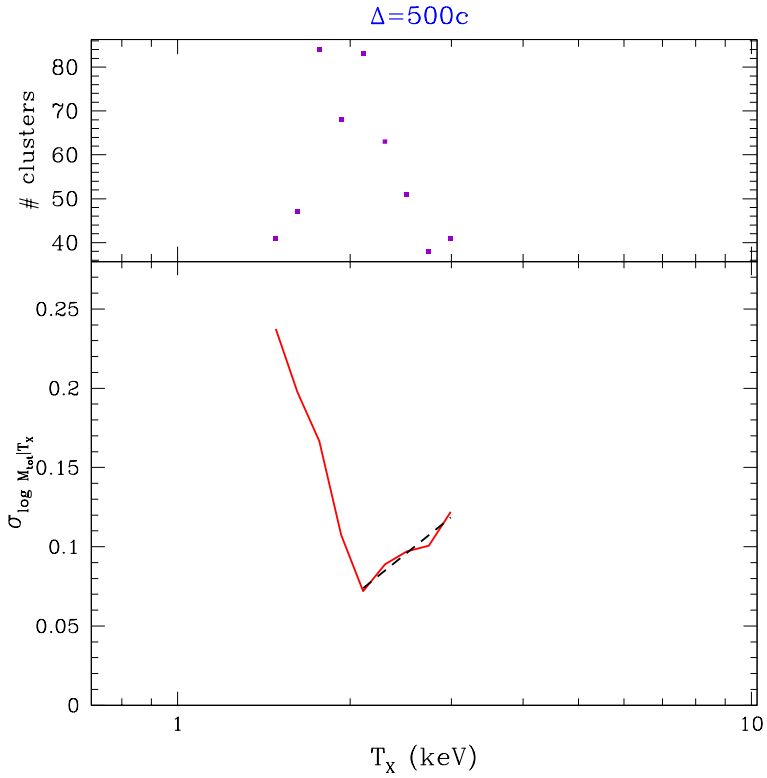

Figure C.3: Same as figure 4.2 for simulation MUWHS.

C.2 $M_{\rm tot} - Y_{\rm X}$ relation

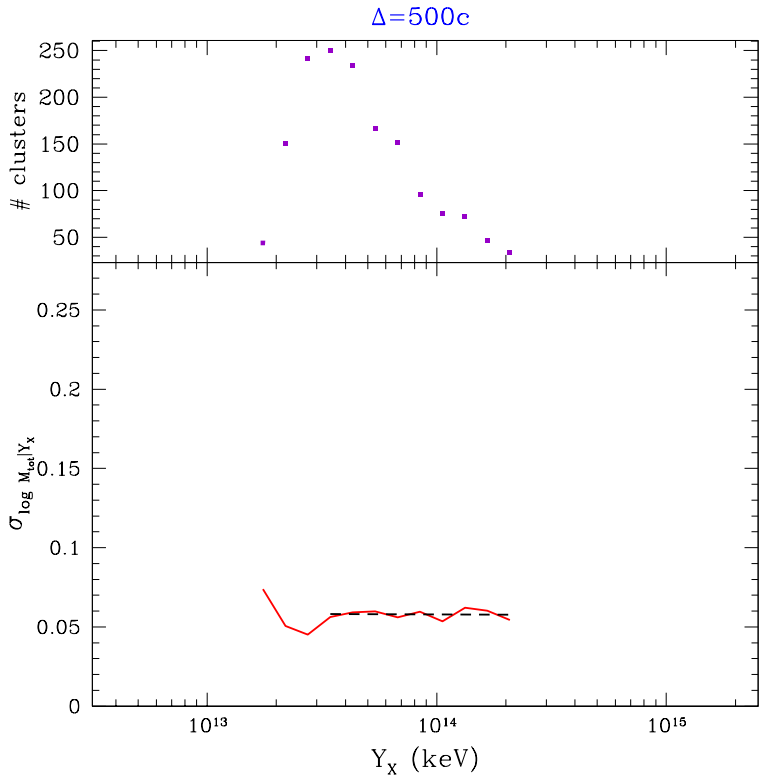

Figure C.4: Same as figure 4.4 for simulation MUCL.

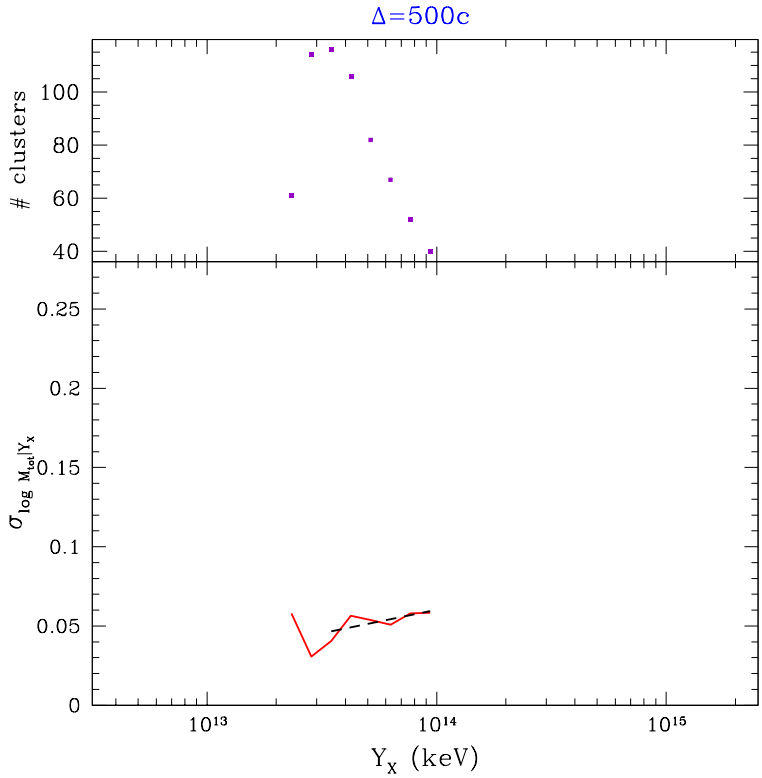

Figure C.5: Same as figure 4.4 for simulation MUW+MU2W.

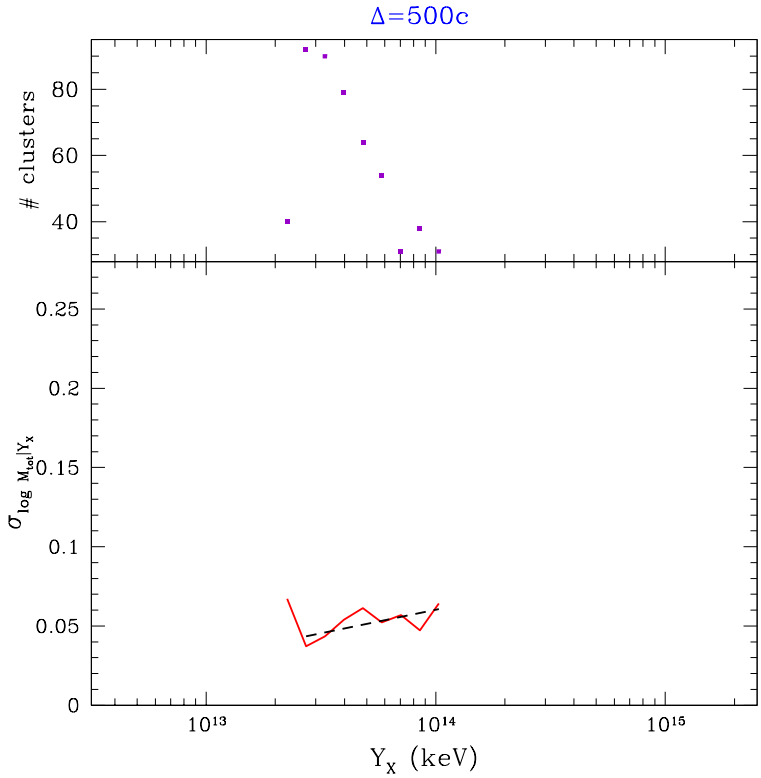

Figure C.6: Same as figure 4.4 for simulation MUWHS.

C.3 $L_{\rm X} - T_{\rm X}$ relation

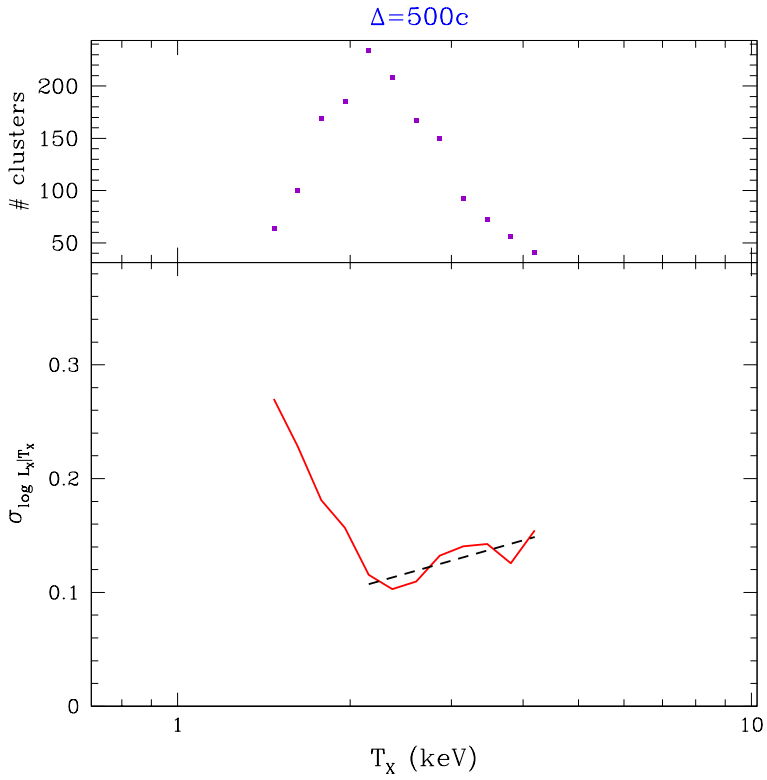

Figure C.7: Same as figure 4.6 for simulation MUCL.

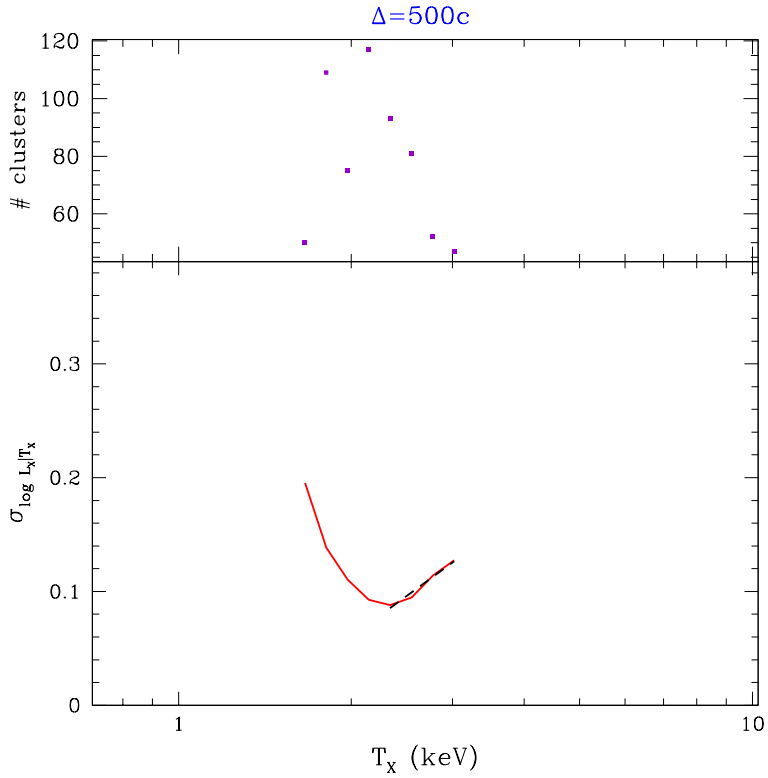

Figure C.8: Same as figure 4.6 for simulation MUW+MU2W.

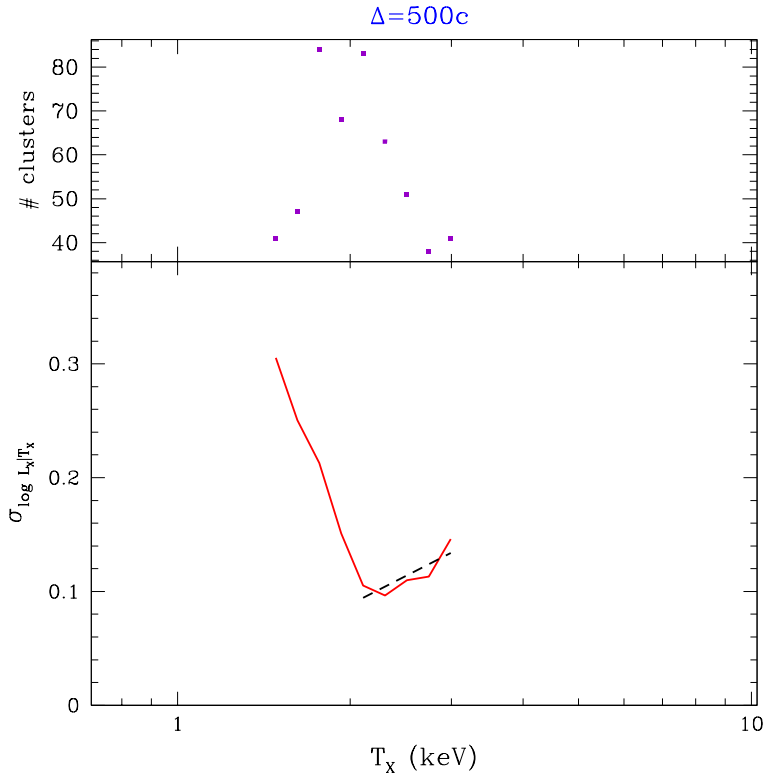

Figure C.9: Same as figure 4.6 for simulation MUWHS.

C.4 $f_{\rm gas} - M_{\rm tot}$ relation

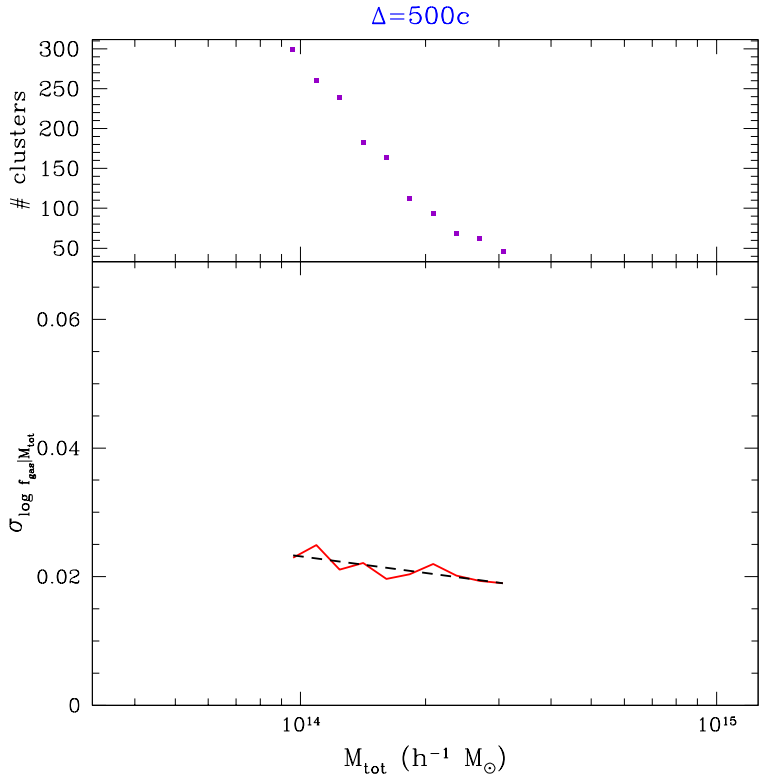

Figure C.10: Same as figure 4.8 for simulation MUCL.

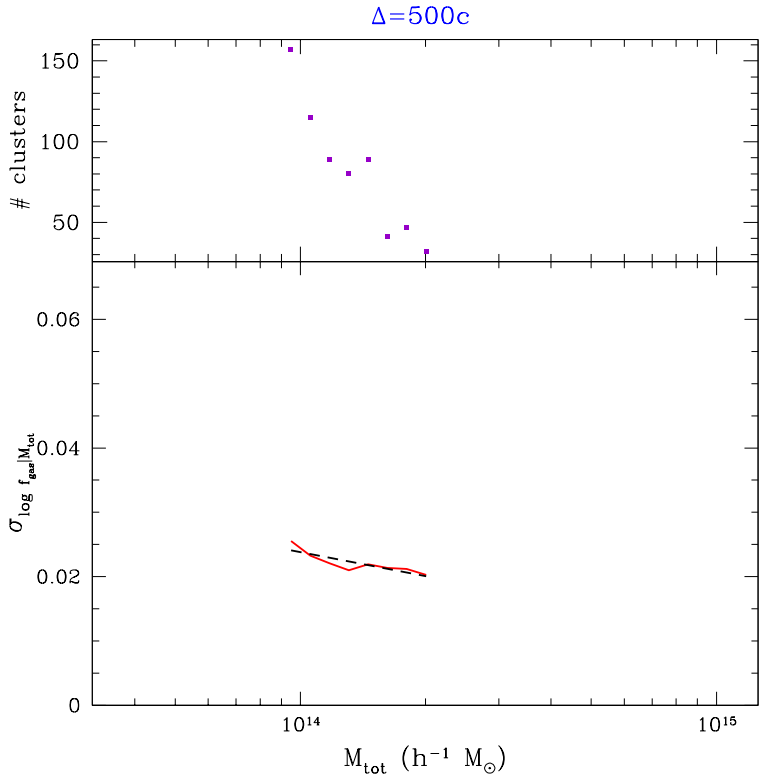

Figure C.11: Same as figure 4.8 for simulation MUW+MU2W.

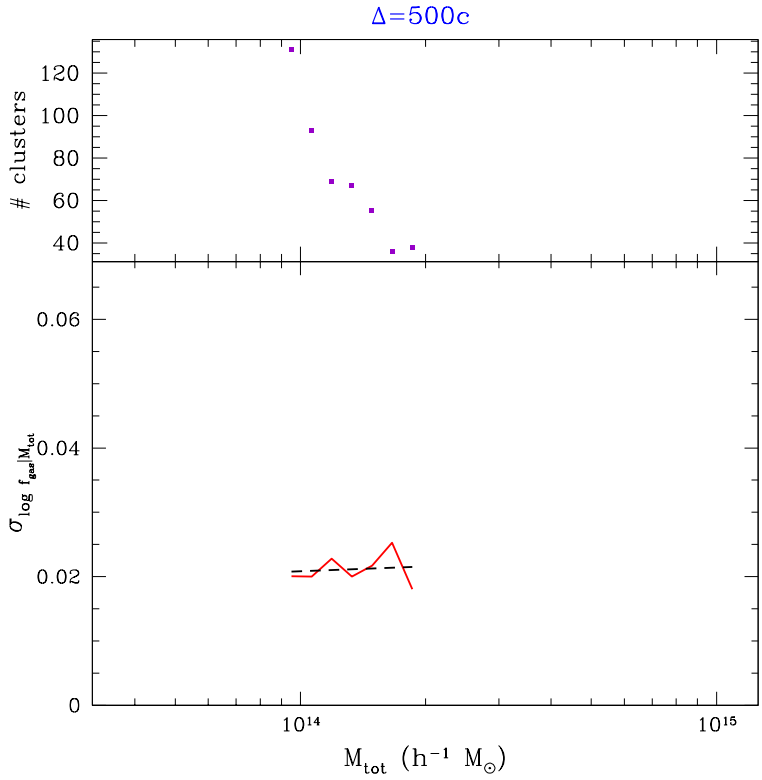

Figure C.12: Same as figure 4.8 for simulation MUWHS.

Appendix D

Evolution

D.1 $M_{\rm tot} - T_{\rm X}$ relation

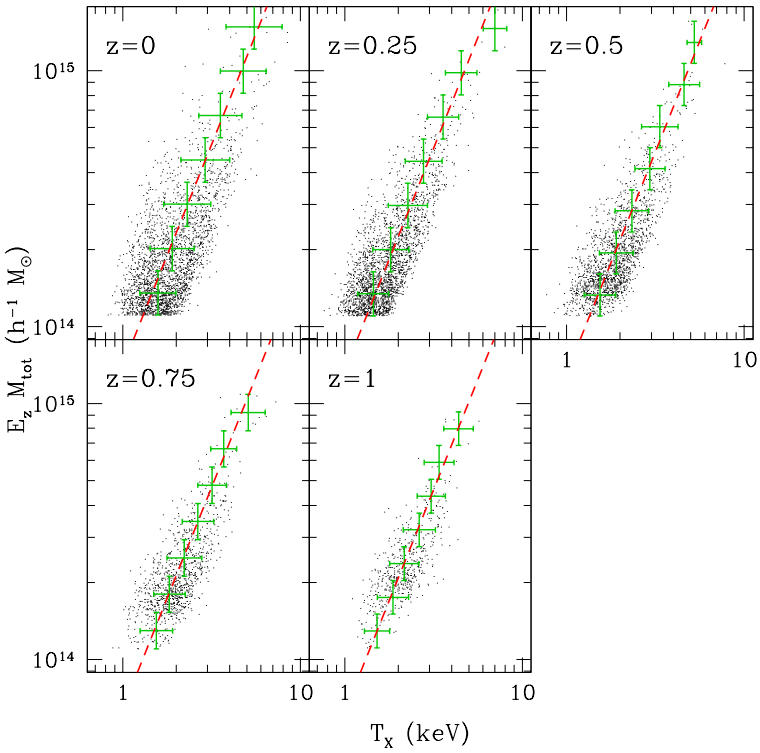

Figure D.1: Redshift dependence on the $M_{\rm tot} - T_{\rm X}$ relation and best fit as seen on table 6.1 for $\Delta = 200$.

D.2 $M_{\rm tot} - Y_{\rm X}$ relation

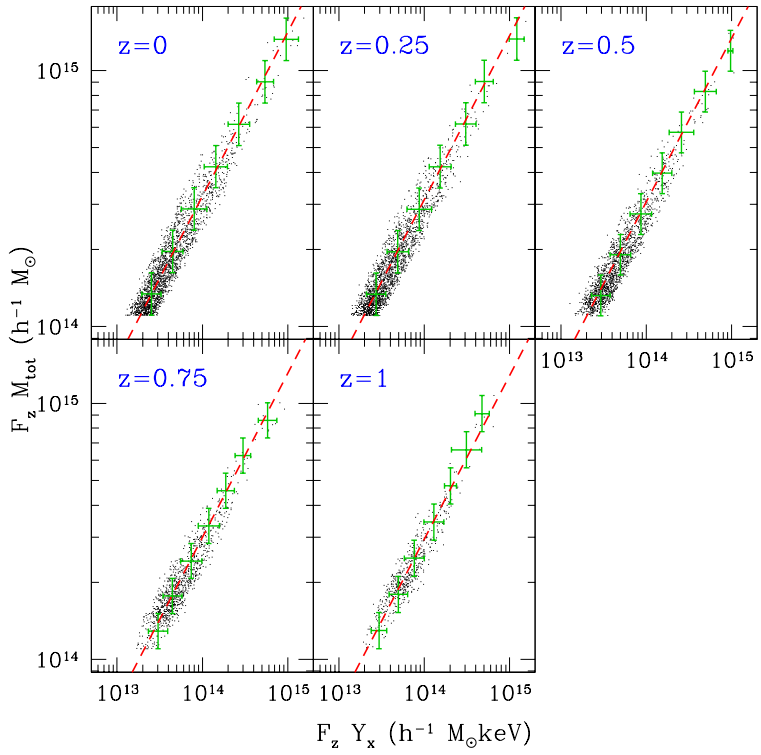

Figure D.2: Redshift dependence on the $M_{\rm tot} - Y_{\rm X}$ relation and best fit as seen on table 6.1 for $\Delta = 200$.

D.3 $L_{\rm X} - T_{\rm X}$ relation

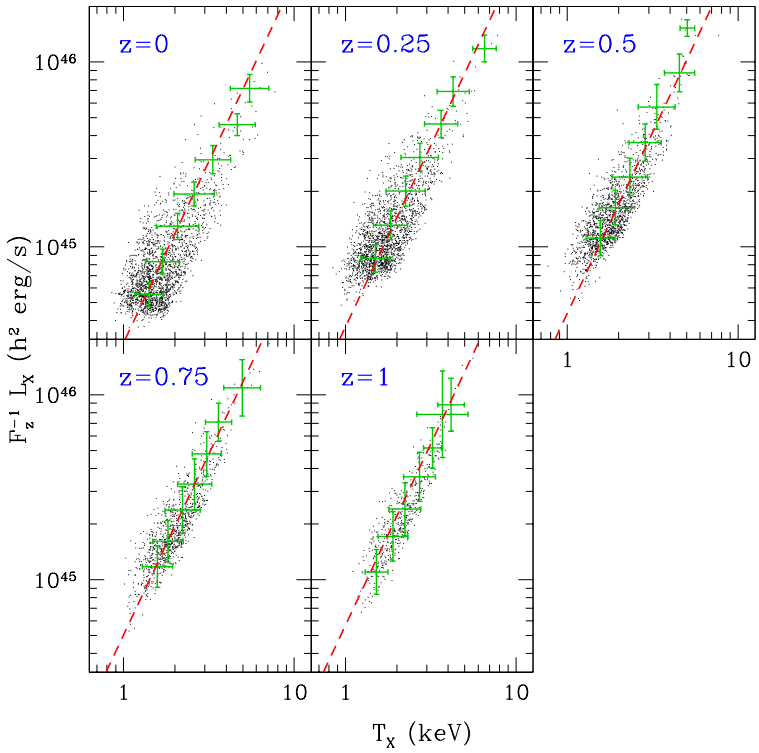

Figure D.3: Redshift dependence on the $L_{\rm X} - T_{\rm X}$ relation and best fit as seen on table 6.1 for $\Delta = 200$.

D.4 $f_{\rm gas} - M_{\rm tot}$ relation

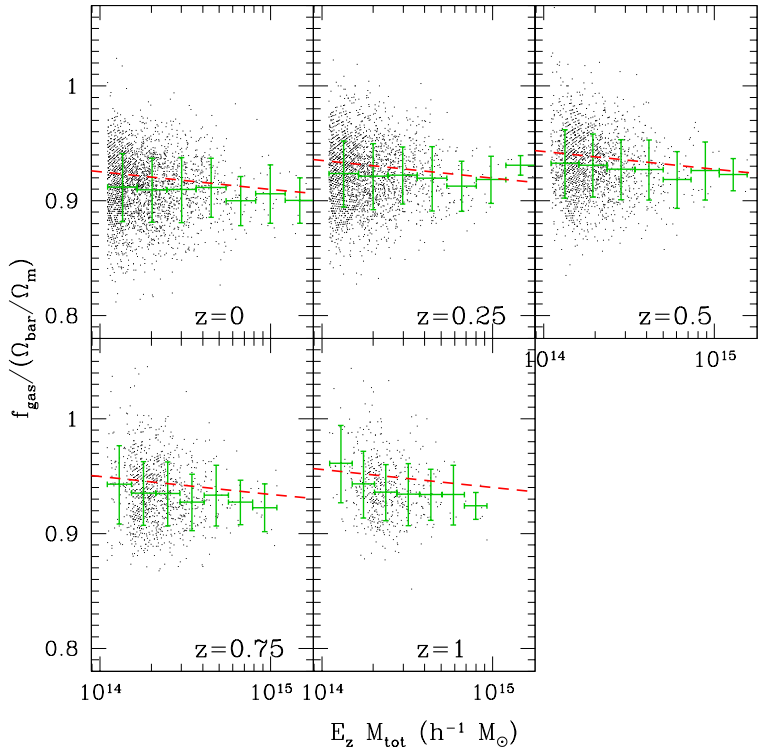

Figure D.4: Redshift dependence on the $f_{\rm gas} - M_{\rm tot}$ relation and best fit as seen on table 6.1 for $\Delta = 200$.

Index

Bibliography

Afshordi, N. 2008, ApJ, 686, 201 pages 129

Allen, S. W. & Fabian, A. C. 1998, MNRAS, 297, L57 pages 78

Allen, S. W., Rapetti, D. A., Schmidt, R. W., et al. 2008, MNRAS, 383, 879 pages 118

Allen, S. W., Schmidt, R. W., Ebeling, H., Fabian, A. C., & van Speybroeck, L. 2004, MNRAS, 353, 457 pages 123

Allen, S. W., Schmidt, R. W., & Fabian, A. C. 2001, MNRAS, 328, L37 pages 79

Allen, S. W., Schmidt, R. W., & Fabian, A. C. 2002, MNRAS, 334, L11 pages 4, 5

Allen, S. W., Schmidt, R. W., Fabian, A. C., & Ebeling, H. 2003, MNRAS, 342, 287 pages 20

Anders, E. & Grevesse, N. 1989, GeCoA, 53, 197 pages 42, 43, 45

Araya-Melo, P. A. 2008, *Tesis Doctoral*, University of Groningen pages 20

Arnaud, M. & Evrard, A. E. 1999, MNRAS, 305, 631 pages 78

Arnaud, M., Pointecouteau, E., & Pratt, G. W. 2007, A&A, 474, L37 pages 119

Ascasibar, Y. & Gottlöber, S. 2008, MNRAS, 386, 2022 pages 20

Ascasibar, Y., Sevilla, R., Yepes, G., Müller, V., & Gottlöber, S. 2006, MNRAS, 371, 193 pages xix, 50, 53, 56, 57

Ascasibar, Y., Yepes, G., Müller, V., & Gottlöber, S. 2003, MNRAS, 346, 731 pages 18, 57

Balogh, M. L., Babul, A., Voit, G. M., et al. 2006, MNRAS, 366, 624 pages 50, 80

Benitez, N., Broadhurst, T. J., Ford, H., et al. 2002, in Bulletin of the American Astronomical Society, Vol. 34, Bulletin of the American Astronomical Society, 1236–+ pages 16

Bialek, J. J., Evrard, A. E., & Mohr, J. J. 2001, ApJ, 555, 597 pages 84

Binney, J. 2004, MNRAS, 350, 939 pages 48

Bonamente, M., Joy, M., LaRoque, S. J., et al. 2008, ApJ, 675, 106 pages 47

Borgani, S. & Kravtsov, A. 2009, ArXiv e-prints pages 117

Borgani, S., Murante, G., Springel, V., et al. 2004, MNRAS, 348, 1078 pages 95, 99

Branchesi, M., Gioia, I. M., Fanti, C., & Fanti, R. 2007, A&A, 472, 739 pages 106, 123

Brickhouse, N. S., Raymond, J. C., & Smith, B. W. 1995, ApJS, 97, 551 pages 17

Bryan, G. L. 2000, ApJL, 544, L1 pages 117

Carlstrom, J. E., Holder, G. P., & Reese, E. D. 2002, ARAA, 40, 643 pages 45, 46

Cen, R. & Ostriker, J. P. 1999, ApJ, 514, 1 pages 37

Cen, R. & Ostriker, J. P. 2006, ApJ, 650, 560 pages 37, 38, 85, 129

Crain, R. A., Eke, V. R., Frenk, C. S., et al. 2007, MNRAS, 377, 41 pages 54, 55, 85, 88, 123, 126, 132

Davé, R., Cen, R., Ostriker, J. P., et al. 2001, ApJ, 552, 473 pages 37, 129

David, L. P., Slyz, A., Jones, C., et al. 1993, ApJ, 412, 479 pages 117

Dunkley, J., Komatsu, E., Nolta, M. R., et al. 2009, ApJS, 180, 306 pages v, viii, 13, 30

Edge, A. C. & Stewart, G. C. 1991, MNRAS, 252, 414 pages 18, 78, 117

Edge, A. C., Stewart, G. C., & Fabian, A. C. 1992, MNRAS, 258, 177 pages 78

Eisenstein, D. J. & Hu, W. 1999, ApJ, 511, 5 pages 8

Eisenstein, D. J., Zehavi, I., Hogg, D. W., et al. 2005, ApJ, 633, 560 pages 11

Eke, V. R., Navarro, J. F., & Frenk, C. S. 1998, ApJ, 503, 569 pages 84

Ettori, S. 2003, MNRAS, 344, L13 pages 84

Ettori, S., Borgani, S., Moscardini, L., et al. 2004a, MNRAS, 354, 111 pages 18, 23, 120, 123

Ettori, S., Dolag, K., Borgani, S., & Murante, G. 2006, MNRAS, 365, 1021 pages 84

Ettori, S., Morandi, A., Tozzi, P., et al. 2009, A&A, 501, 61 pages 59, 124

Ettori, S., Tozzi, P., Borgani, S., & Rosati, P. 2004b, A&A, 417, 13 pages 105, 120, 122

Evrard, A. E., Bialek, J., Busha, M., et al. 2008, ApJ, 672, 122 pages 29, 33

Fabian, A. C., Crawford, C. S., Edge, A. C., & Mushotzky, R. F. 1994, MNRAS, 267, 779 pages iii, vii, 18, 78

Frenk, C. S., White, S. D. M., Bode, P., et al. 1999, ApJ, 525, 554 pages 28, 56, 84, 87

Giodini, S., Pierini, D., Finoguenov, A., et al. 2009, ApJ, 703, 982 pages 118, 123

Gonzalez, A. H., Zaritsky, D., & Zabludoff, A. I. 2007, ApJ, 666, 147 pages 123

Gottlöber, S. & Yepes, G. 2007, ApJ, 664, 117 pages 31, 34, 56, 85

Greene, J. 1959, ApJ, 130, 693 pages 52

Hallman, E. J., O'Shea, B. W., Burns, J. O., et al. 2007, ApJ, 671, 27 pages 47

Harford, A. G., Hamilton, A. J. S., & Gnedin, N. Y. 2008, MNRAS, 389, 880 pages 129

Harrison, E. R. 1970, PhRvD, 1, 2726 pages 8

Hashimoto, Y., Henry, J. P., Boehringer, H., & Hasinger, G. 2007, A&A, 468, 25 pages 112

He, P., Feng, L., & Fang, L. 2005, ApJ, 623, 601 pages 85

Henry, J. P. 2004a, ApJ, 609, 603 pages 20

Henry, J. P. 2004b, ApJ, 609, 603 pages 93, 97, 98, 127, 133

Henry, J. P., Evrard, A. E., Hoekstra, H., Babul, A., & Mahdavi, A. 2009, ApJ, 691, 1307 pages 20

Herschel, W. 1785, Philosophical Transactions Series I, 75, 213 pages 14

Hilton, M., Collins, C. A., Stanford, S. A., et al. 2007, ApJ, 670, 1000 pages 122

Hinshaw, G., Weiland, J. L., Hill, R. S., et al. 2009, ApJS, 180, 225 pages 11, 30

Hu, W. 2003, PhRvD, 67, 081304 pages 105

Hubble, E. 1929, Proceedings of the National Academy of Science, 15, 168 pages 6

Ikebe, Y., Reiprich, T. H., Böhringer, H., Tanaka, Y., & Kitayama, T. 2002, A&A, 383, 773 pages 23, 93, 97, 98, 127, 133

Itoh, N. & Nozawa, S. 2004, A&A, 417, 827 pages 47

Jeltema, T. E., Canizares, C. R., Bautz, M. W., & Buote, D. A. 2005, ApJ, 624, 606 pages 35, 112

Jeltema, T. E., Hallman, E. J., Burns, J. O., & Motl, P. M. 2008, ApJ, 681, 167 pages 50, 112, 126, 127, 131, 133

Kaastra, J. S., Paerels, F. B. S., Durret, F., Schindler, S., & Richter, P. 2008, Space Science Reviews, 134, 155 pages 17

Kaiser, N. 1986, MNRAS, 222, 323 pages iii, vii, 106

Kay, S. T., da Silva, A. C., Aghanim, N., et al. 2007, MNRAS, 377, 317 pages 109, 111, 115, 117, 120, 121, 123

Kay, S. T., Thomas, P. A., Jenkins, A., & Pearce, F. R. 2004, MNRAS, 355, 1091 pages 87, 88

Kay, S. T., Thomas, P. A., & Theuns, T. 2003, MNRAS, 343, 608 pages 84

Klypin, A., Gottlöber, S., Kravtsov, A. V., & Khokhlov, A. M. 1999, ApJ, 516, 530 pages 33

Klypin, A., Kravtsov, A. V., Bullock, J. S., & Primack, J. R. 2001, ApJ, 554, 903 pages 32

Knollmann, S. R. & Knebe, A. 2009, ApJS, 182, 608 pages 35

Knop, R. A., Aldering, G., Amanullah, R., et al. 2003, ApJ, 598, 102 pages 4, 5

Kotov, O. & Vikhlinin, A. 2005, ApJ, 633, 781 pages 105, 106, 110, 115, 120, 122

Kotov, O. & Vikhlinin, A. 2006, ApJ, 641, 752 pages 110, 116, 122

Kowalski, M., Rubin, D., Aldering, G., et al. 2008, ApJ, 686, 749 pages 11, 12

Kravtsov, A., Gonzalez, A., Vikhlinin, A., et al. 2009, in Astronomy, Vol. 2010, astro2010: The Astronomy and Astrophysics Decadal Survey, 164–+ pages 118

Kravtsov, A. V., Nagai, D., & Vikhlinin, A. A. 2005, ApJ, 625, 588 pages 54, 56, 84

Kravtsov, A. V., Vikhlinin, A., & Nagai, D. 2006, ApJ, 650, 128 pages 40, 47, 51, 72, 74, 139

LaRoque, S., Bonamente, M., Carlstrom, J., et al. 2005, in Bulletin of the American Astronomical Society, Vol. 37, Bulletin of the American Astronomical Society, 1226–+ pages 113

Lesgourgues, J., Viel, M., Haehnelt, M. G., & Massey, R. 2007, Journal of Cosmology and Astro-Particle Physics, 11, 8 pages 29

Li, G. L., Mao, S., Jing, Y. P., et al. 2006, MNRAS, 372, L73 pages 33

Liedahl, D. A., Osterheld, A. L., & Goldstein, W. H. 1995, ApJL, 438, L115 pages xvii, 43

Lima, M. & Hu, W. 2005, PhRvD, 72, 043006 pages 62

Lin, Y., Mohr, J. J., & Stanford, S. A. 2003, ApJ, 591, 749 pages 85

Lodders, K. 2003, ApJ, 591, 1220 pages 42

Mantz, A., Allen, S. W., Ebeling, H., Rapetti, D., & Drlica-Wagner, A. 2009, ArXiv e-prints pages iii, vii, 51, 60, 110, 113, 114, 116, 120

Markevitch, M. 1998, ApJ, 504, 27 pages iii, vii, 78

Mathiesen, B. F. & Evrard, A. E. 2001, ApJ, 546, 100 pages 40

Maughan, B. J. 2007, ApJ, 668, 772 pages 47, 106, 112, 113, 121

Maughan, B. J., Jones, C., Forman, W., & Van Speybroeck, L. 2008a, ApJS, 174, 117 pages 35, 115

Maughan, B. J., Jones, L. R., Ebeling, H., & Scharf, C. 2006, MNRAS, 365, 509 pages 105, 120, 121, 122, 123

Maughan, B. J., Jones, L. R., Pierre, M., et al. 2008b, MNRAS, 387, 998 pages 110, 113, 114, 115, 121, 127, 134

Mazzotta, P., Rasia, E., Moscardini, L., & Tormen, G. 2004, MNRAS, 320 pages 41

McCarthy, I. G., Babul, A., Bower, R. G., & Balogh, M. L. 2008, MNRAS, 386, 1309 pages 85

McCarthy, I. G., Bower, R. G., & Balogh, M. L. 2007, MNRAS, 377, 1457 pages 33, 84

Mewe, R., Gronenschild, E. H. B. M., & van den Oord, G. H. J. 1985, A&AS, 62, 197 pages xvii, 43

Miralda-Escudé, J., Cen, R., Ostriker, J. P., & Rauch, M. 1996, ApJ, 471, 582 pages 36

Monaghan, J. J. 1992, ARAA, 30, 543 pages xvii, 28

Morandi, A., Ettori, S., & Moscardini, L. 2007, MNRAS, 379, 518 pages 61, 105, 122

Muanwong, O., Kay, S. T., & Thomas, P. A. 2006, ApJ, 649, 640 pages 106

Muanwong, O., Thomas, P. A., Kay, S. T., & Pearce, F. R. 2002, MNRAS, 336, 527 pages 84

Nagai, D. 2006, ApJ, 650, 538 pages 47, 52, 72, 127, 133

Nagai, D., Kravtsov, A. V., & Vikhlinin, A. 2007a, ApJ, 668, 1 pages 66, 74, 112

Nagai, D., Vikhlinin, A., & Kravtsov, A. V. 2007b, ApJ, 655, 98 pages 51, 52, 64, 95, 99, 127, 133

Nicastro, F., Mathur, S., & Elvis, M. 2008, Science, 319, 55 pages 36

Novicki, M. C., Sornig, M., & Henry, J. P. 2002, AJ, 124, 2413 pages 116

O'Hara, T. B., Mohr, J. J., Bialek, J. J., & Evrard, A. E. 2006, ApJ, 639, 64 pages 59

O'Hara, T. B., Mohr, J. J., & Sanderson, A. J. R. 2007, ArXiv e-prints pages 105, 113

Pedersen, K. & Dahle, H. 2007, ApJ, 667, 26 pages 29

Peebles, P. J. E. 1993, Principles of physical cosmology (Princeton Series in Physics, Princeton, NJ: Princeton University Press, —c1993) pages 9

Pierpaoli, E., Scott, D., & White, M. 2001, MNRAS, 325, 77 pages 94

Ponman, T. J., Cannon, D. B., & Navarro, J. F. 1999, Natur, 397, 135 pages iv, vii

Power, C., Navarro, J. F., Jenkins, A., et al. 2003, MNRAS, 338, 14 pages 48

Prada, F., Klypin, A. A., Simonneau, E., et al. 2006, ApJ, 645, 1001 pages 20

Pratt, G. W., Arnaud, M., Piffaretti, R., et al. 2010, A&A, 511, A85+ pages iii, vii, 113, 115

Rapetti, D., Allen, S. W., & Weller, J. 2005, MNRAS, 360, 555 pages 118

Rasia, E., Ettori, S., Moscardini, L., et al. 2006, MNRAS, 369, 2013 pages 112, 127, 133

Reiprich, T. H. & Böhringer, H. 2002, ApJ, 567, 716 pages 20

Rines, K., Diaferio, A., & Natarajan, P. 2007, ApJ, 657, 183 pages 100

Rines, K., Diaferio, A., & Natarajan, P. 2008, ApJL, 679, L1 pages 99

Rines, K., Forman, W., Pen, U., Jones, C., & Burg, R. 1999, ApJ, 517, 70 pages 123

Rosati, P., Borgani, S., & Norman, C. 2002, ARAA, 40, 539 pages iii, vii, xix, 19, 53, 91, 117

Roussel, H., Sadat, R., & Blanchard, A. 2000, A&A, 361, 429 pages 85

Rozo, E., Wechsler, R. H., Koester, B. P., et al. 2007, ArXiv Astrophysics e-prints pages 29, 33, 100

Rozo, E., Wechsler, R. H., Rykoff, E. S., et al. 2010, ApJ, 708, 645 pages 20, 29, 100, 127, 133

Rudd, D. H. 2007, *Tesis Doctoral*, The University of Chicago pages 54, 56, 107, 120, 121, 122, 126, 127, 132, 133, 134

Rykoff, E. S., McKay, T. A., Becker, M. R., et al. 2008, ApJ, 675, 1106 pages 61, 62

Sadat, R., Blanchard, A., Vauclair, S. C., et al. 2005, A&A, 437, 31 pages 85

Schuecker, P., Böhringer, H., Reiprich, T. H., & Feretti, L. 2001, A&A, 378, 408 pages 59

Short, C. J., Thomas, P. A., Young, O. E., et al. 2010, ArXiv e-prints pages 120, 121, 122, 123, 127, 133, 134

Smith, B. D., Hallman, E. J., Shull, J. M., & O'Shea, B. W. 2010, ArXiv e-prints pages 37, 129

Spergel, D. N., Bean, R., Doré, O., et al. 2007, ApJS, 170, 377 pages v, viii

Spergel, D. N., Verde, L., Peiris, H. V., et al. 2003, ApJS, 148, 175 pages v, viii, 5

Springel, V. 2005, MNRAS, 364, 1105 pages xvii, 26, 27

Springel, V. & Hernquist, L. 2002, MNRAS, 333, 649 pages 26

Stanek, R., Evrard, A. E., Böhringer, H., Schuecker, P., & Nord, B. 2006, ApJ, 648, 956 pages 23, 61

Stanek, R., Rasia, E., Evrard, A. E., Pearce, F., & Gazzola, L. 2010, ApJ, 715, 1508 pages 67, 75, 88

Sun, M., Voit, G. M., Donahue, M., et al. 2009, ApJ, 693, 1142 pages 110, 113, 119

Sunyaev, R. A. & Zel'dovich, Y. B. 1972, Comments on Astrophysics and Space Physics, 4, 173 pages xvii, 45

Sutherland, R. S. & Dopita, M. A. 1993, ApJS, 88, 253 pages 43

Tozzi, P., Rosati, P., Ettori, S., et al. 2003, ApJ, 593, 705 pages 44

Ventimiglia, D. A., Voit, G. M., Donahue, M., & Ameglio, S. 2008, ApJ, 685, 118 pages 61, 63

Verde, L., Haiman, Z., & Spergel, D. N. 2002, ApJ, 581, 5 pages 129

Vikhlinin, A. 2006, ApJ, 640, 710 pages 21, 41, 110

Vikhlinin, A., Burenin, R. A., Ebeling, H., et al. 2009, ApJ, 692, 1033 pages iv, viii, 50, 51, 61, 64, 109, 110, 112, 113, 116, 121, 126, 133

Vikhlinin, A., Kravtsov, A., Forman, W., et al. 2006, ApJ, 640, 691 pages iii, vii, 51, 57, 110, 113, 116, 119, 120

Vikhlinin, A., van Speybroeck, L., Markevitch, M., Forman, W. R., & Grego, L. 2002, ApJL, 578, L107 pages 105

Voit, G. M. 2005a, Advances in Space Research, 36, 701 pages iii, vii, 18

Voit, G. M. 2005b, Reviews of Modern Physics, 77, 207 pages 18, 59, 122

Voit, G. M. & Bryan, G. L. 2001, Natur, 414, 425 pages 117

Yang, H., Ricker, P. M., & Sutter, P. M. 2009, ApJ, 699, 315 pages 50, 126, 132

Yepes, G., Sevilla, R., Gottlöber, S., & Silk, J. 2007, ApJL, 666, L61 pages 30

Young, O. E., Thomas, P. A., Short, C. J., & Pearce, F. 2010, ArXiv e-prints pages 88, 118, 124